

https://dspace.org/

The study of quaternary semiconducting chalcogenide nanomaterials for application as counter electrodes

Ngubeni, Grace Nomthandazo

2021

University of the Witwatersrand, Johannesburg

https://hdl.handle.net/10539/46127

Ngubeni, Grace Nomthandazo. (2021). The study of quaternary semiconducting chalcogenide nanomaterials for application as counter electrodes [PhD thesis, University of the Witwatersrand, Johannesburg]. WIReDSpace. https://hdl.handle.net/10539/46127

Downloaded from a DSpace repository. https://dspace.org/

The study of quaternary semiconducting chalcogenide nanomaterials for application as counter electrodes

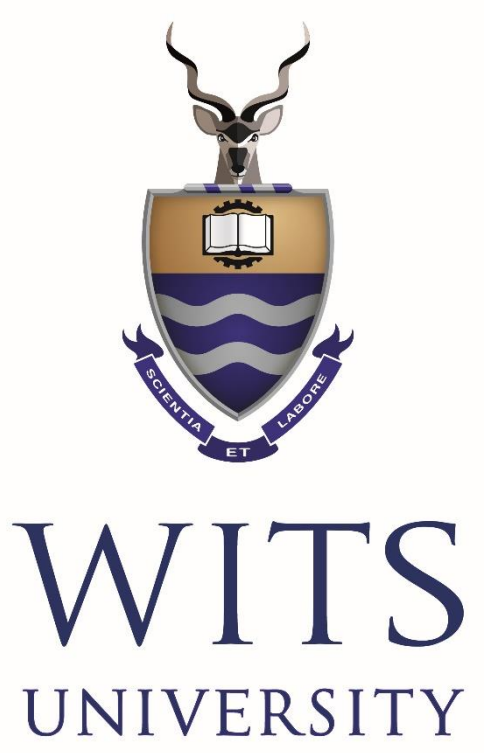

A thesis submitted to the Faculty of Science, University of the Witwatersrand,
in partial fulfilment for the degree
Doctor of Philosophy

By

Grace Nomthandazo Ngubeni
307412

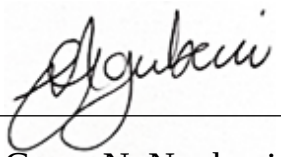

Grace N. Ngubeni

August 2021

Date



Advisor

Prof Nosipho Moloto

August 2021

Date

DECLARATION

I declare that the work reported herein is my own independent work, submitted at the School of Chemistry, University of the Witwatersrand, Johannesburg. This work has not been submitted for any degree or examination in any other institution of higher learning.

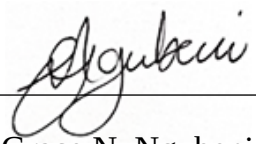

Grace N. Ngubeni

August 2021

Date

ABSTRACT

Herein, the colloidal synthesis of Cu_2ZnSnS_4 (CZTS), $Cu_2ZnSnSe_4$ (CZTSe) and the first time colloidal synthesis of Li_2ZnSnS_4 (LZTS) and Na_2ZnSnS_4 (NZTS) nanoparticles respectively were investigated. All the nanoparticles were applied as counter electrodes in dye-sensitized solar cells (DSSCs). For the CZTS and CZTSe nanoparticles in particular, the effect of three substrates, namely, vitreous carbon (VC), indium tin oxide (ITO) and fluorine doped tin oxide (FTO) on the electrocatalytic properties including the overall performance of the solar cells were investigated. The CZTS and CZTSe were successfully synthesized and characterized with X-ray diffraction (XRD), Raman spectroscopy, X-ray photoelectron spectroscopy (XPS), Fourier-transform infrared (FT-IR), nuclear magnetic resonance (NMR), and ultra-violet visible (UV-vis) spectroscopy and transmission electron microscope (TEM) for the morphologies. CZTSe on glassy carbon (VC) had better electrocatalytic activity as compared to CZTS, however, the DSSCs from VC were poor due to the reduced transmittance of the substrate. On ITO and FTO, CZTS performed the best. Electrochemically, CZTS had the lowest series resistance and charge transfer resistance however had the largest exchange current density and limiting diffusion current thereby making it the best electrocatalyst. The DSSC using CZTS–ITO gave the best performance with the power conversion efficiency (PCE) of 3.62%.

Conversely, for the LZTS and NZTS nanoparticles the effect of the lithium and sodium precursors and the ratio of the constituents e.g. Li:Zn:Sn:S and Na:Zn:Sn:S on the properties of the LZTS and NZTS nanoparticles, respectively were investigated. In addition, the effect of the substrates, that is, ITO vs FTO on the electrocatalytic properties as well as overall performance of the DSSCs were studied. Using the Li_2S precursor, the XPS, ^{7}Li MAS NMR and Raman spectroscopy confirmed the presence of lithium and the formation of LZTS. Since the Li_2S source and the 2:1:0.25:2 ratio, resulted in the purest particles, these were therefore used as CEs in DSSCs for the first time. LZTS nanoparticles on ITO gave the best performance with 2.26% PCE.

Similarly, the study of NZTS indicated that the NaCl regardless of the ratios used resulted in the formation of impurities as observed from XRD patterns. The presence of sodium and the complete formation of NZTS nanoparticles through ^{23}Na MAS NMR, XPS and Raman

spectroscopy were investigated. The results indicated that the Na_2S-based nanoparticles in the 2:1:0.5:4 ratio, yielded the purest NZTS nanoparticles. As such, these results indicated a PCE of 3.93%.

The study illustrates that alkali metals (Li^+ and Na^+) can be used as the monovalent cation in quaternary nanoparticles, instead of the commonly used Cu^+ transition metal with promising results as counter electrode materials in DSSCs. Notably, the NZTS nanoparticles illustrated a higher PCE to CZTS while LZTS had the lowest PCE. It must be however noted, that these results require further optimization to explore the full potential of these alkali metal-based quaternary nanoparticles.

Keywords: Cu_2ZnSnS_4; $Cu_2ZnSnSe_4$; Li_2ZnSnS_4; Na_2ZnSnS_4; substrates; counter electrodes; dye-sensitized solar cells

DEDICATION TO

My Parents

Mr Vusumuzi Philemon Ngubeni

&

Mrs Goodness Thokozile Ngubeni

My Siblings

Mr Ngoako & Mrs Busisiwe Huma

(My nieces: Zoe, Zion & Shiloh)

Mr Nkosinathi Peter & Mrs Charlotte Motlalepula Ngubeni

(My nephew Thando & niece Musa)

Mr Thokozani & Mrs Lerato Yolanda Ngubeni

Ms. Joy Ngubeni

maNkomo amahle

ACKNOWLEDGEMENTS

- I would like to thank God, my Abba Father for guiding, providing and sustaining me. “Ngiyabonga moya oyingcwele, Ngikuzwile ke uhamba name, Ngimangaliswa nguwe kule ndlela, Ung’phethe kahle standwa sam” ~ Hlengiwe Mhlaba

- I would like to express my heartfelt gratitude to Prof Nosipho Moloto for her guidance, support and mentoring. I am inspired by the commitment and passion you have for acquiring knowledge and imparting it to the next generation of scientists.

- I would like to thank my research funders i.e. NRF, MERG and Wits Bursary. Your financial contribution made the journey worthwhile. A special thanks to the School of Chemistry, the MMU facility and NMISA.

- To my fellow colleagues in the NANO-WEBS group (Lab330B) and the CATMAT group – thank you for your assistance throughout the research project. Your insights were invaluable. A special shout out goes to Lineo Mxakaza, Olusola Akinbami, Esmie Mposa, Siyabonga Nkabinde, Zakhele Ndala, Ndivhuwo Shumbula, Muhammed Ballim, Dr Lerato Machogo, Dr Mildred Airo, Michelle Thiebaut and Mathias Kiefer for all the chats and advice through this journey.

- Thank you to Dr Francis Otieno, Dr Adewale Ipadeola and Dr Rudolph Erasmus for assisting me with analysing some of my samples at different stages of my research.

- To my family at large and friends thank you for your constant support and believing in me. Your constant encouragement has not gone unnoticed. A special mention to JP aka T.R.M., Jabulile Ndaba and Bandile Khwela.

- To the Chemistry staff, you welcomed me with such warmth and have been very encouraging. Thank you! A special thank you Mam Khwezi Ndawonde, Mary-Ann and Mrs. Gaby Meirim your assistance during my transition and guidance has been invaluable.

PRESENTATIONS

- Oral presentation at the 70th Annual Meeting of International Society of Electrochemistry conference held in International Convention Centre, Durban from 04 – 09 August 2019.

- Poster presentation at the Nanosmat – Africa 2018 International Conference held in the Western Cape by iThemba Labs/UNISA from 19 – 23 November 2018.

- Poster presentation and School Visit: Ettore Majorana Foundation and Centre for Scientific Culture, Erice (Italy), 7th -12th July 2018 – focus "Materials for Energy and Sustainability".

- Poster presentation at the 9th International Conference of the African Materials Research Society held at the Gaborone International Conference Centre from 09 – 14 December 2017.

- Poster presentation at the 7th Annual Gauteng South African Nanotechnology Initiative – Nanosciences Young Researcher's Symposium (SANi – NYRS) held at Tshwane University of Technology, on the 20th October 2017.

- Numerous departmental seminars at the School of Chemistry, University of the Witwatersrand, 2017-2020.

LIST OF PUBLICATIONS

- Nosipho Moloto, **Grace N. Ngubeni**, Kalenga P. Mubiayi, Alkali metal quaternary nanomaterials, South African Provisional Patent Application no. 2020/01521. *{Contribution: I did all the synthetic work and did most of the characterization}.*

- **Grace N. Ngubeni**, Olusola Akinbami, Lineo Mxakaza, Siyabonga Nkabinde, Tshwarela Kolokoto, Francis Otieno, Makwena J. Moloto, Kalenga P. Mubiayi, Nosipho Moloto, Evaluating the effect of the substrate on the electrocatalytic performance of Cu_2ZnSnS_4 and $Cu_2ZnSnSe_4$ counter electrodes in dye-sensitized solar cells, *Thin Solid Films*, (2021) [Under review, TSF-D-21-00280]. {*Contribution: I did all the synthetic work, did most of the characterization and all of the analysis, that includes XRD, TEM, UV-vis, NMR and Raman spectroscopy and wrote and corrected the manuscript. XPS was ran external to the university at NMISA. Mr Akinbami, Ms Mxakaza, Mr Nkabinde and Ms Kolokoto helped with the electrochemistry characterization and brainstorming of ideas. Dr Otieno helped with the solar cell characterization and Dr Mubiayi and Profs Moloto conceptualized the project, supervised the work and edited the manuscript*}.

- Olusola Akinbami, **Grace Ngubeni**, Francis Otieno, Rudo Kadzutu-Sithole, Cebisa Linganiso, Zikhona Tetana, Siziwe Gqoba, Kalenga Mubiayi, Nosipho Moloto, *Journal of Materials Chemistry C*, (2021), DOI: 10.1039/d1tc00264c. *{Contribution: I contributed with the discussion and characterization on FTIR and NMR spectroscopies}.*

- Olusola Akinbami, Refilwe Moepya, **Grace Ngubeni**, Makwena Justice Moloto, Nosipho Kalenga Mubiayi, Lead-free Rudorffite-type $Cs_3Bi_2Br_9$ nanoparticles for photocatalytic degradation of Rhodamine B and methylene blue, *Journal of Photochemistry & Photobiology, A: Chemistry*, 2021 [Under review, JPHOTOCHEM-D-21-00168]. *{Contribution: I contributed with the discussion and characterization on FTIR and NMR spectroscopies}.*

- Rudo K. Sithole, Tshwarela Kolokoto, Lerato F.E. Machogo, **Grace N. Ngubeni**, Makwena J. Moloto, Juanita van Wyk, Nosipho Moloto, Simultaneous capping and substitution of nitrogen ions of Cu_3N nanocrystals with sulfur ions using DDT as a co-surfactant to form chalcocite and digenite nanocrystals, *Materials Chemistry and Physics*, 251 (2020) 123074. *{Contribution: I contributed with the discussion and characterization on FTIR and NMR spectroscopies}.*

- Siyabonga S. Nkabinde, Zakhele B. Ndala, Ndivhuwo P. Shumbula, Tshwarela Kolokoto, Obakeng Nchoe, **Grace N. Ngubeni**, Kalenga P. Mubiayi, Nosipho Moloto, Delineating the role of crystallinity in the electrocatalytic activity of colloidally synthesized MoP nanocrystals, *New Journal of Chemistry*, 44 (2020) 14041-14049. *{Contribution: I contributed with the discussion XPS spectroscopy}.*

- Lerato F.E. Machogo, Musa Mthimunye, Rudo K. Sithole, Phumlani Tetyana, Neo Phao, **Grace N. Ngubeni**, Mbuso Mlambo, Phumlane S. Mdluli, Poslet M. Shumbula, Nosipho Moloto, Elucidating the structural properties of gold selenide nanostructures, *New Journal of Chemistry*, 43 (2019) 5773-5782. *{Contribution: I contributed with the discussion XPS spectroscopy}.*

TABLE OF CONTENTS

1. Declaration iii

2. Abstract iv

3. Dedication to vi

4. Acknowledgements vii

5. Presentations viii

6. List of Publications ix

7. Table of contents xi

8. List of Figures xv

9. List of Tables xx

10. List of Symbols and Abbreviations xxii

11. Synopsis xxv

Chapter 1 26

General Background 26

1.1. Introduction 26

1.2. Problem Statement 30

1.3. Rationale and motivation 30

1.4. Aim and objectives 30

References 32

Chapter 2 33

Literature Review 33

2.1. Semiconducting nanoparticles 33

2.2 Brief introduction about quaternary nanocrystals 35

2.2.1 Copper Chalcogenides 39

2.2.2 Mixed Chalcogenides 40

2.2.3 Doping/Alloying 41

2.2.4 Monovalent cation replacement of Cu to Li and Na 43

2.2.5 Electronic Band structure of KS, ST and PMCA 43

2.3 Synthetic methods for quaternary nanocrystals 46

2.3.1 Solid-state synthetic methods 46

2.3.2 Solution-based synthetic methods....47
2.3.3 Colloidal synthesis....48
2.3.3.1 Nucleation....48
2.3.3.2 Growth....49
2.3.3.3 Effect of time....50
2.3.3.4 Effect of temperature....51
2.3.3.5 Effect of precursors....52
2.3.3.6 The effects of precursor addition and molar ratios....53
2.3.3.7 Effect of capping agents....54
2.4 Application of quaternary nanocrystals....56
2.4.1 Device: Dye-Sensitized Solar cell....56
2.4.1.1 Architecture of a DSSC....56
2.4.1.2 Mechanism....57
2.4.1.3 Photoanode....58
2.4.1.4 Electrolyte....58
2.4.1.5 Counter electrode....58
2.5 Electrochemical Analysis....60
2.6 Dye-sensitized solar cell performance....62
References....65
Chapter 3....71
Evaluating the effect of the substrate on the electrocatalytic performance of Cu_2ZnSnS_4 and $Cu_2ZnSnSe_4$ counter electrodes in dye-sensitized solar cells....71
3.1. Introduction....71
3.2. Experimental section....72
3.2.1. Materials....72
3.2.2. Synthesis of the CZTS and CZTSe nanoparticles....73
3.2.3. Fabrication of the dye-sensitized solar cells....73
3.2.4. Characterization....74
3.3. Results and discussions....75
3.3.1. Nanoparticle powder analysis....75
3.3.2: Raman analysis of CZTS and CZTSe nanoparticles....76
3.3.3: XPS analysis of CZTS and CZTSe....77

3.3.4: Surface characterisation of CZTS and CZTSe using FTIR and NMR 80
3.3.5: Morphological characterisation of CZTS and CZTSe 84
3.3.6: Absorption analysis of CZTS and CZTSe nanoparticles 85
3.3.7. Electrochemical analysis of CZTS and CZTSe 86
3.3.8. Device fabrication: dye-sensitized solar cells of CZTS and CZTSe 90
3.4. Conclusions 91
References 93
Chapter 4 95
Novel colloidal synthesis of Li_2ZnSnS_4 nanoparticles and its application as counter electrodes in dye-sensitized solar cells 95
4.1. Introduction 95
4.2. Experimental section 96
4.2.1. Materials 96
4.2.2. Colloidal synthesis of LZTS nanoparticles 96
4.2.3. The process of the fabrication of dye-sensitized solar cells 97
4.2.4. Characterization 97
4.3. Results and Discussions 98
4.3.1. Structural characterization of LZTS nanoparticles 98
4.3.2. Morphological characteristics of LZTS nanoparticles 100
4.3.3. XPS analysis of LZTS nanoparticles 101
4.3.4. NMR analysis of LZTS nanoparticles 104
4.3.5. Absorption analysis of LZTS nanoparticles 105
4.3.5. Raman analysis of LZTS nanoparticles 106
4.3.6. Application of LZTS as a counter electrode in dye-sensitized solar cells 107
4.3.7. Device fabrication: dye-sensitized solar cells 111
4.4. Conclusions 112
References 113
Chapter 5 115
The effect of Na-based precursors in the novel colloidal synthesis of Na_2ZnSnS_4 quaternary semiconducting nanocrystals and its application in dye-sensitized solar cells 115
5.1. Introduction 115
5.2. Experimental section 116

5.2.1 Materials 116
5.2.2 Colloidal synthesis of Na_2ZnSnS_4 nanoparticles 116
5.2.3 Device fabrication of the dye-sensitized solar cells 117
5.2.4 Characterization 117
5.3. Results and Discussion 117
5.3.1. Structural characterization of NZTS nanoparticles 117
5.3.2. Solid-state NMR characterization of NZTS nanoparticles 120
5.3.3. XPS characterization of NZTS nanoparticles 121
5.3.4. Morphological characterization of NZTS nanoparticles 125
5.3.5. Optical analysis of NZTS nanoparticles 126
5.3.6. Raman characterization of NZTS nanoparticles 127
5.3.7. FT-IR and liquid-state NMR of NZTS nanoparticles 128
5.3.8 Electrochemical characterization of Na_2S_NZTS nanoparticles 129
5.3.9 Device fabrication: dye-sensitized solar cells 133
5.4. Conclusions 134
References 136
Chapter 6 138
Overall conclusions and recommendations 138
6.1. Conclusions 138
6.2. Recommendations 139
Appendix 141
Supporting Information 141

LIST OF FIGURES

Fig. 1.1: The seventeen sustainable development goals. [Access: 16 Feb. 2021] 26

Fig. 1.2: The projected energy mix strategic development plan [4]. 27

Fig. 1.3: Annual solar radiation map of South Africa [5]. 28

Fig. 1.4: Efficiency chart depicting the most prominent first, second and third generation solar cells [12]. 29

Fig. 2.1: Schematic illustrating the effect of quantum confinement [1]. 33

Fig. 2.2: Direct and indirect bandgap illustrations of semiconductors. 35

Fig. 2.3: The relationship II-VI, I-III-VI and I-II-IV-VI chemical composition of semiconducting material [6]. 36

Fig. 2.4: The progression of the crystal structures from binary to quaternary semiconducting nanocrystals [30]. 39

Fig. 2.5: The crystal structures of CZTS in the kesterite (a), half-disordered kesterite (b) and fully disordered kesterite (c) [32]. 40

Fig. 2.6: The illustration of the kesterite, defective kesterite and stannite structure of CZTS (a-c); Na-doped kesterite (d-f) and Ca-doped kesterite (g) crystal structures at varying concentrations of the dopant [45]. 42

Fig. 2.7: The electronic band structure of the KS, ST and PMCA Ag_2CdSnS_4 using PBE-GGA (a) and mBJ-GGA (b) approximations [49]. 44

Fig. 2.8: The kesterite, stannite, and PMCA crystal structures of quaternary nanoparticles... 44

Fig. 2.9: The top-down (a) and bottom-up (b) synthetic reaction illustrations. 46

Fig. 2.10: Schematic diagram illustrating parameters used to control the synthesis of quaternary semiconducting nanoparticles [60]. 48

Fig. 2.1: The LaMer nucleation and growth diagram [61]. 49

Fig. 2.12: The UV-vis spectra of $CuInS_2$ nanocrystals at different reaction times [66]. 50

Fig. 2.13: The TEM images depicting the effect of time on quaternary nanoparticles [67].... 51

Fig. 2.14: UV-vis and photoluminescence spectra of Cu-Zn-In-S nanocrystals at different reaction temperatures [68]. 52

Fig. 2.15: Schematic of the components of a dye-sensitized solar cell [83]. 57

Fig. 2.16: Spin-coating, dip-coating and drop-casting techniques for depositing nano-inks onto conductive substrates [92-94]. 59

Fig. 2.17: The cyclic voltammograms of Pt, CZTS and CZTSe over a -0.6 – 1.2 potential difference [96].....60

Fig. 2.18: The Nyquist (a) and Tafel polarization plots (b) of Pt, CZTS, CCTS and CNTS respectively [72].....61

Fig. 2.19: Schematic illustrating the I/V curve for evaluating solar cell performance. 62

Fig. 2.20: The energy level diagram (a) and J-V curve plots (b) of CZTS and CZTSe [98]...63

Fig. 3.1: X-ray diffraction patterns of CZTS, CZTSe and their standard reference patterns. .76

Fig. 3.2: Raman spectra of CZTS and CZTSe using a 532 nm laser. 77

Fig. 3.3: XPS survey spectrum, Cu 2p, Zn 2p, Sn, 3d and S 2p high-resolution spectra of CZTS. 78

Fig. 3.4: XPS survey spectrum, Cu 2p, Zn 2p, Sn, 3d and Se 3d high-resolution spectra of CZTSe. 79

Fig. 3.5: C 1s, N 1s and O 1s high-resolution spectra for CZTS nanoparticles. 80

Fig. 3.6: FT-IR spectra of OLA, CZTS and CZTSe. 81

Fig. 3.7: ^{1}H NMR and ^{13}C NMR spectra of oleylamine, CZTS and CZTSe nanoparticles. 82

Fig. 3.9: UV-vis absorption spectra (a) and Tauc plot (b) of CZTS and CZTSe nanoparticles. 85

Fig. 3.10: Cyclic voltammetry of Pt, CZTS and CZTSe at a scan rate of 50 mV.s^{-1}, Nyquist plots of EIS for the symmetric cells with CZTS and CZTSe on GC and the electrochemical equivalent circuit. 86

Fig. 3.11: Nyquist plots of EIS for the symmetric cells with Pt, CZTS and CZTSe on ITO and FTO substrates, Tafel plots Pt, CZTS and CZTSe electrodes on ITO and FTO substrates. 88

Fig. 3.12: DSSC set-up, band diagram and J-V curves of DSSCs of CZTS and CZTSe on VC, ITO and FTO substrates. 90

Fig. 4.1: X-ray diffraction patterns of LZTS nanoparticles synthesized using different lithium sources (LiCl, Li(acac), Li_2S) at different precursor ratios (1:1:1:1 and 2:1:0.25:2). 98

Fig. 4.2: the kesterite, stannite, and PMCA structural representations for LZTS. 99

Fig. 4.4: XPS survey spectra of LZTS nanoparticles synthesized using different lithium sources (LiCl, Li(acac), Li2S) at different precursor ratios (1:1:1:1 and 2:1:0.25:2). 102

Fig. 4.5: Li 1s high-resolution spectra of LZTS nanoparticles synthesized using different lithium sources (LiCl, Li(acac), Li_2S) at different precursor ratios (1:1:1:1 and 2:1:0.25:2). 103

Fig. 4.6: Zn 2p, Sn 3d, S 2p high-resolution spectra of LZTS nanoparticles synthesized using different Li_2S at different precursor ratios 2:1:0.25:2. 104

Fig. 4.7: ^{7}Li MAS NMR spectra of the LiCl, Li(acac) and Li_2S and the corresponding LZTS spectra. 105

Fig. 4.8: Tauc plots derived from UV-vis absorption spectra of LZTS nanoparticles synthesized using different lithium sources (LiCl, Li(acac), Li_2S) at different precursor ratios (1:1:1:1 and 2:1:0.25:2). 106

Fig. 4.9: Raman spectrum of LZTS nanoparticles synthesized using Li_2S and 2:1:0.25:2 ratio. 107

Fig. 4.10: Cyclic voltammetry of Pt and LZTS at a scan rate of 50 $mV.s^{-1}$, Nyquist plot of the EIS for the symmetric cell with LZTS on GC and the electrochemical equivalent circuit. ..108

Fig. 4.11: Nyquist plots of EIS for the symmetric cells with Pt and LZTS on ITO and FTO substrates, Tafel plots of Pt and LZTS electrodes on ITO and FTO substrates.....109

Fig. 4.12: DSSC set-up, band diagram and J-V curves of DSSCs of LZTS on ITO and FTO substrates.....111

Fig. 5.1: X-ray diffractograms of the Na_2ZnSnS_4 nanoparticles synthesized with different sodium precursors (NaCl and Na_2S), precursor ratios (1:1:1:1 and 2:1:0.5:4) and the standard reference pattern.....119

Fig. 5.2: ^{23}Na MAS NMR spectra illustrating the ratio study of NZTS using NaCl and Na_2S as different sodium precursors, including the NaCl starting material. 121

Fig. 5.3: survey spectra of the three Na precursor sources for 1:1:1:1 and 2:1:0.25:2 ratios.122

Fig. 5.4: Na 1s high-resolution spectra of NZTS nanoparticles synthesized from different sodium sources (i.e. NaCl and Na_2S) at different precursor ratios. 123

Fig. 5.5: The high-resolution spectra of Zn 2p NZTS. 124

Fig. 5.6: The high-resolution spectra of Sn 3d NZTS.....124

Fig. 5.7: The high-resolution spectra of S 2p of NZTS. 125

Fig. 5.8: TEM micrographs of NZTS nanoparticles synthesized from different sodium precursors (NaCl and Na_2S) at different ratios (1:1:1:1 and 2:1:0.5:4). 126

Fig. 5.9: Tauc plots of NZTS nanoparticles using NaCl and Na_2S precursors with varying mole ratios (1:1:1:1 and 2:1:0.5:4).....127

Fig. 5.10: Raman spectrum of Na_2S_NZTS 2:1:0.5:4 ratio nanoparticles using the 785 nm laser. 128

Fig. 5.11: Cyclic voltammograms of Pt and Na_2S_NZTS (2:1:0.5:4) counter electrodes analysed at a scan rate of 50 mV/s (a), EIS plot of NZTS counter electrode on a glassy carbon substrate (b) and the equivalent electrochemical circuit model (c). 130

Fig. 5.12: (a) The equivalent circuit model of Na_2S_NZTS (2:1:0.5:4) with the EIS measurements on (b) ITO (left) and (c) FTO.....131

Fig. 5.13: Tafel polarization curves of Pt and Na_2S_NZTS (2:1:0.5:4) using dummy symmetrical electrodes on ITO and FTO substrates. 133

Fig. 5.14: J-V curves of DSSCs of Pt and Na_2S_NZTS 2:1:0.5:4 on ITO and FTO substrates. 133

Fig. 3.1S: C 1s, N 1s and O 1s high-resolution spectra for CZTSe nanoparticles. 141

Fig. 3.3S: ^{1}H NMR and ^{13}C NMR spectra of oleylamine, CZTS and CZTSe nanoparticles. 142

Fig. 4.1S: LiCl_LZTS (1:1:1:1) ratio nanocrystals depicting the high-resolution spectra of the C 1s, N 1s and O 1s. 143

Fig. 4.2S: LiCl_LZTS (2:1:0.25:2) ratio nanocrystals depicting the high-resolution spectra of the C 1s, N 1s and O 1s. 143

Fig. 4.3S: Li_2S_LZTS (1:1:1:1) ratio nanocrystals depicting the high-resolution spectra of the C 1s, N 1s and O 1s. 143

Fig. 4.4S: Li_2S_LZTS (2:1:0.25:2) ratio nanocrystals depicting the high-resolution spectra of the C 1s, N 1s and O 1s. 144

Fig. 4.5S: Li(acac)_LZTS (1:1:1:1) ratio nanocrystals depicting the high-resolution spectra of the C 1s, N 1s and O 1s. 144

Fig. 4.6S: Li(acac)_LZTS (2:1:0.25:2) ratio nanocrystals depicting the high-resolution spectra of the C 1s, N 1s and O 1s. 144

Fig. 4.7S: OLA and LZTS FT-IR spectra 145

Fig. 4.8S: the ^{1}H NMR spectra of OLA. 145

Fig. 4.9S: the ^{1}H NMR spectra of Li_2S_LZTS nanoparticles. 146

Fig. 4.10S: the ^{13}C NMR spectra of OLA. 146

Fig. 4.11S: the ^{13}C NMR spectra of Li_2S_LZTS. 147

Fig. 4.12S: Raman spectra of LiCl and Li(acac) LZTS material analysed using the 785 nm laser. 147

Fig. 5.1S: C 1S, N 1s and O 1s high-resolution spectra for NaCl_NZTS (1:1:1:1) ratio nanoparticles. 148

Fig. 5.2S: C 1S, N 1s and O 1s high-resolution spectra for NaCl_NZTS (2:1:0.5:4) ratio nanoparticles. 148

Fig. 5.3S: C 1S, N 1s and O 1s high-resolution spectra for Na_2S_NZTS (1:1:1:1) ratio nanoparticles. 148

Fig. 5.4S: C 1S, N 1s and O 1s high-resolution spectra for Na_2S_NZTS (2:1:0.5:4) ratio nanoparticles. 149

Fig. 5.5S: FT-IR spectra of OLA & NZTS respectively. 149

Fig. 5.6S: ^{1}H NMR spectra of (a) OLA and (b) NZTS nanoparticles. 154
Fig. 5.7S: ^{13}C NMR spectra of (a) OLA and (b) NZTS nanoparticles. 155
Fig. 5.8S: Raman spectrum of NaCl_NZTS. 156

LIST OF TABLES

Table 2.1: Summary of quaternary nanoparticles and their application/s 37

Table 2.3: Lattice parameters of tetragonal CZTS structures [27]. 45

Table 2.2: Summary of three mechanisms to form ideal NPs. 53

Table 3.1: NMR assignments of OLA, CZTS and CZTSe nanoparticles. 83

Table 3.2: CV and EIS parameters from counter electrodes drop-casted on glassy-carbon electrode 87

Table 3.3: Electrochemical performance parameters obtained from EIS & Tafel polarization plots based on CZTS and CZTSe nanoparticles on ITO and FTO substrates 89

Table 3.4: J-V parameters of DSSCs of Pt, CZTS and CZTSe on VC, ITO and FTO substrates 91

Table 4.1: Synthetic procedure of LZTS. 97

Table 4.2: Lattice parameters of tetragonal LZTS structures. 100

Table 4.3: CV and EIS parameters from the LZTS counter electrodes drop-casted on glassy-carbon electrode 108

Table 4.4: Electrochemical performance parameters obtained from EIS & Tafel polarization plots based on LZTS nanoparticles on ITO and FTO substrates 110

Table 4.5: J-V parameters of DSSCs of Pt and LZTS on ITO and FTO substrates 112

Table 5.1: Synthetic procedure of NZTS 117

Table 5.2: Lattice parameters of tetragonal NZTS structures. 120

Table 5.3: NMR assignments for OLA and Na_2S_NZTS (2:1:0.5:4) nanoparticles. 129

Table 5.3: CV and EIS parameters for NZTS on glassy carbon substrate. 130

Table 5.4: Electrochemical performance parameters obtained from EIS and Tafel polarization plots based on Na_2S_NZTS (2:1:0.5:4) nanoparticles on ITO and FTO. 132

Table 5.5: J-V parameters of DSSCs of Pt and NZTS on ITO and FTO substrates. 134

Table 5.1S: Summary of the atomic composition stoichiometric assignments obtained from the fitting of the XPS spectra. 150

Table 5.2S: Summary of the atomic composition stoichiometric assignments obtained from the fitting of the XPS spectra. 151

Table 5.3S: Summary of the atomic composition stoichiometric assignments obtained from the fitting of the XPS spectra. 152

Table 5.4S: Summary of the atomic composition stoichiometric assignments obtained from the fitting of the XPS spectra. 153

LIST OF SYMBOLS AND ABBREVIATIONS

1-DDT – 1-Dodecanethiol

C 1s – Carbon 1s spectrum

CB – Conduction band

C_{dl} – Double layer capacitance

CE – Counter electrode

CNT – Classical nucleation theory

CuCl – Copper Chloride

CV – Cyclic voltammetry

CZTS – copper zinc tin sulfide (Cu_2ZnSnS_4)

CZTSe – copper zinc tin selenide ($Cu_2ZnSnSe_4$)

CZTSSe – copper zinc tin sulfide selenide ($Cu_2ZnSnSSe_4$)

D – Diffusion coefficient

DSSC – Dye-sensitized solar cell

E_g – Band gap

EIS – Electrochemical impedance spectroscopy

Epp – Peak-to-peak separation

FCC – Face-centered cubic

FF – Fill factor

FT-IR – Fourier-transform infrared spectroscopy

FTO – Fluorine-doped tin oxide

HDA – Hexadecylamine

HOMO – Highest occupied molecular orbital

ITO – Indium-doped tin oxide

J_0 – Exchange current density

J_{lim} – Limiting diffusion current density

J_{sc} – Short-circuit current density

J-V – Photocurrent voltage

KS – Kesterite

Li(acac) – lithium acetylacetonate

LUMO – Lowest unoccupied molecular orbital

LZTS – Lithium zinc tin sulfide (Li_2ZnSnS_4)

mA – Milliampere

MAS NMR – Magic angle spinning nuclear magnetic resonance

NaCl – Sodium chloride

$Na_2S{\cdot}9H_2O$ – Sodium sulfide nonahydrate

NP – Nanoparticle

NMR – Nuclear magnetic resonance

NZTS – sodium zinc tin sulfide (Na_2ZnSnS_4)

OA – Oleic acid

OLA – Oleylamine

PCE – Power conversion efficiency (η)

P_{max} – Maximum power output

PMCA – Primitive mixed Cu-Au

Pt - Platinum

PV – Photovoltaic

QD – Quantum dot

R_{ct} – Charge transfer resistance

R_s – Series/Solution resistance

R_{sh} – Shunt resistance

S – Sulfur

Se – Selenium

SILAR – Successive ionic layer adsorption and reaction

SnCl – Tin chloride

ST – Stannite

TCO – Transparent conductive oxide

TEM – Transmission electron microscopy

UV-Vis – Ultra-violet visible spectrometry

VB – Valence band

VC – Vitreous carbon

V_{cu} – Copper vacancy

V_{oc} – Open-circuit voltage

XPS – X-ray photoelectron spectroscopy

XRD – X-ray diffraction

ZnCl – Zinc chloride

Z_w – Nernst diffusion

Z’ – Real

Z’’ – Imaginary

SYNOPSIS

Quaternary semiconducting nanomaterial are part of the *third generation* of photovoltaic cells, which have received much attention because of their use of earth-abundant elements. This study was motivated by the promising electrocatalytic results observed from the popular CZTS and CZTSSe nanoparticles and their use in dye-sensitized solar cells. The alkali metal doping/alloying of the Cu-based chalcogenides have also shown promising results however, the replacement of Cu with alkali metals has been unexplored for solution-based synthesis methods. This thesis reports on the synthesis of CZTS, CZTSe and novel synthesis of LZTS and NZTS nanoparticles using the colloidal method. The electrocatalytic properties of the quaternary semiconducting nanoparticles were explored using cyclic voltammetry, electrochemical impedance spectroscopy and through the fabrication of dye-sensitized solar cells with the aims of replacing platinum as the counter electrode. The order of this thesis is detailed below:

Chapter 1: The general background, motivation, rational, aims and objectives of the research project.

Chapter 2: The backbone of this study will be detailed in the literature review as such; it will cover the introduction of Cu-based quaternary nanoparticles and its properties, doping/alloying of Cu-chalcogens and the replacement of the monovalent Cu with alkali metals.

Chapter 3: Will report the findings of the fabricated CZTS and CZTSe counter electrodes on different substrates.

Chapter 4: Will report on the novel synthesis of LZTS using varying precursors; vary the precursor additions and ratios. This part of the study aims to determine the best parameters for the synthesis and electrocatalytic performance of the new LZTS nanoparticles.

Chapter 5: Similarly, this chapter will report on the novel synthesis of NZTS using varying precursors, vary the precursor additions and ratios. This part of the study aims to determine the best parameters for the synthesis and electrocatalytic performance of the new NZTS nanoparticles.

Chapter 6: Conclusions and recommendations (future work)

***Appendix*:** Will have all the additional figures and tables from Chapter 3 to 5.

CHAPTER 1
General Background

1.1. Introduction

The global increase in population has a direct impact on the supply and demand of energy. The seventeen global sustainable development goals shown in Fig. 1.1 have been developed as a guideline to help transform our world towards sustainable living [1]. High on the list of the sustainable development goals is the need for affordable and clean energy. There is a continuous battle for Africa to meet its ever-increasing energy demands. The increase in population puts more strain on the continent and alternative methods have become imperative. The continued use of traditional sources of energy (i.e. oil, coal and natural gas) and the increased demand builds the argument towards moving from depleting traditional energy sources to more abundant non-traditional renewable energy sources [2,3].



Fig. 1.1: The seventeen sustainable development goals. [Access: 16 Feb. 2021]

South Africa has projected energy mix that can help the country meet its energy demand. This can be achieved using wind, water and solar power. Among the various energy solutions possible, solar energy is the front-runner for providing alternative energy. Moreover, as

observed in Fig. 1.2, solar energy has the potential to contribute about 60% towards the projected energy mix by the year 2050 [4].

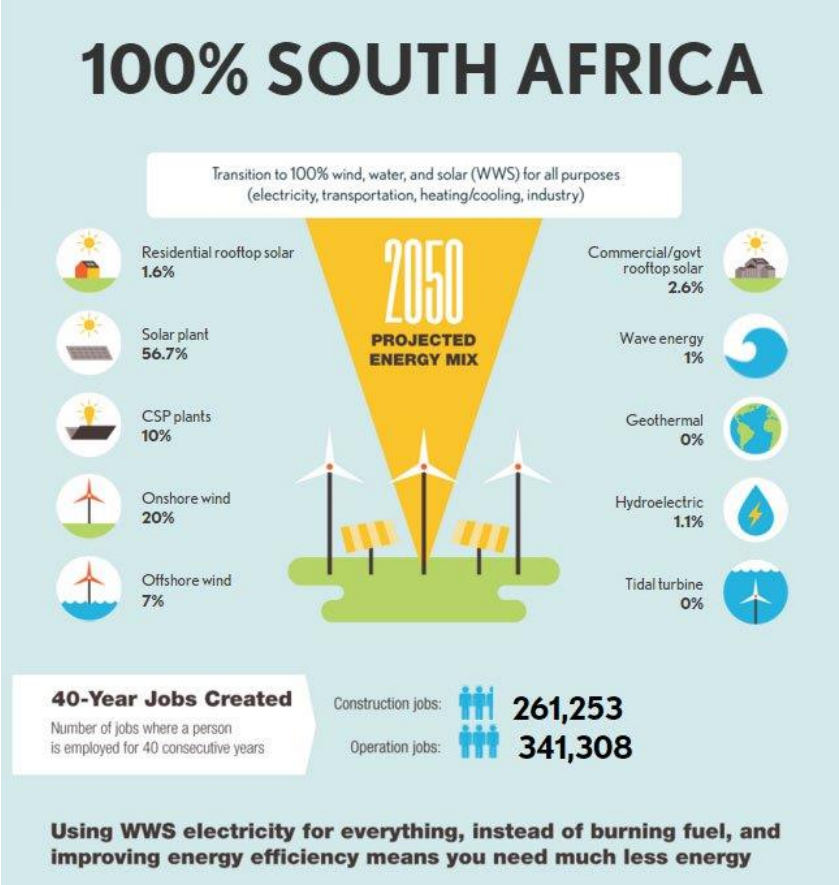

Fig. 1.2: The projected energy mix strategic development plan [4].

The use of candles and kerosene lamps for lighting and solid biomass (i.e. fuel wood, charcoal or dung) for cooking purposes, are still common practices within the country, more specifically in informal settlements, rural and remote areas. As an alternative to these common practices, many South African households survive on the illegal connection of electricity from the grid, which causes an overload to the electrical supply. The overload causes damage to the infrastructure. In the attempt to solve these energy demands, the state owned power supplier i.e. Eskom has introduced load shedding [5]. The strategy behind load shedding is to reduce the excessive load on the grid. This is a temporary solution and not very sustainable as it leaves large parts of the country without electricity for hours. The unexpected load shedding, forces communities to resort to the traditional methods for lighting, warmth and cooking for their households, thus creating a vicious cycle. Therefore, the more sustainable way to combat this

crisis is to integrate two types of technologies i.e. off-grid generated and grid-connected photovoltaic (PV) systems [6, 7]. However, one of the major drawbacks with off-grid PVs is the need to have efficient storage systems in place. The storage systems are costly unless alternative technologies such as emerging supercapacitors, fuel cells and batteries are incorporated [6]. On the other hand, grid-connected PVs have attracted much interest because they are have a dual function of storage and supply of excess energy, thus, eliminating the need for storage devices.

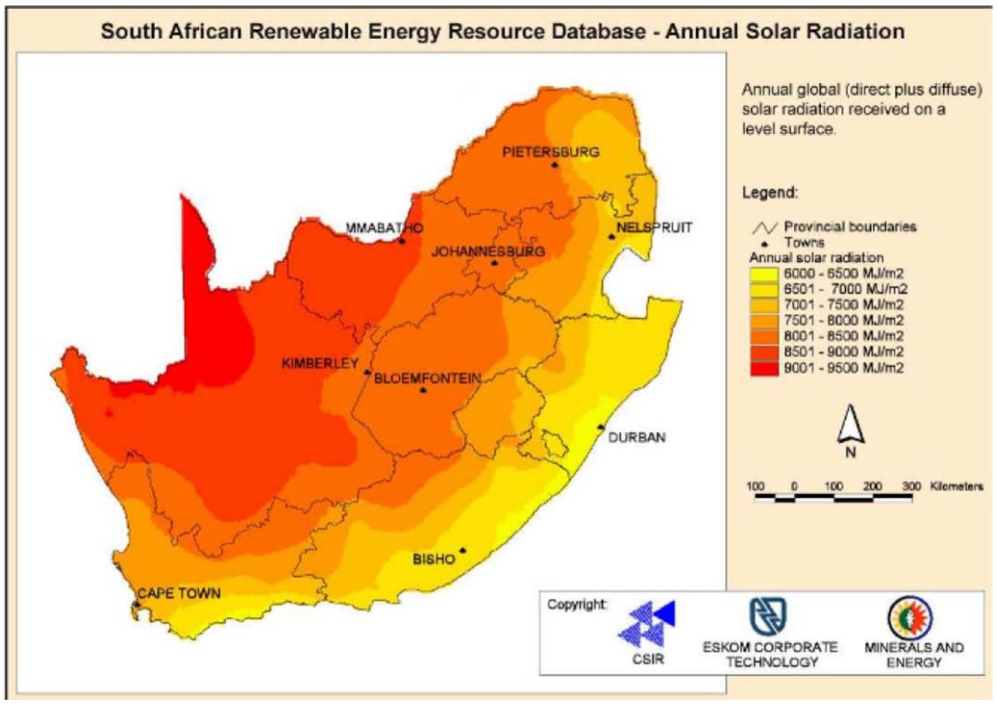

Fig. 1.3: Annual solar radiation map of South Africa [5].

From the annual solar radiation map, depicted in Fig. 1.3, there is an obvious benefit towards harnessing solar energy. In South Africa, high solar radiation regions cover an area of about 194000 km^2, and this can potentially generate about 1300 MJ/m^2/year of energy [6]. This further cements the need to explore and develop solar energy technology for South Africa. Over the years, there has been gradual progress with PV technologies. From the *first-generation* PV cells which are made of monocrystalline silicon. These are the most efficient single-layer PVs and have been the most adopted commercially. However, they suffer from high cost due to the manufacturing processes, thus limiting their wide adoption. To circumvent this, *second-generation* PV cells (amorphous-Silicon, CdTe and CIGS) have been developed.

These largely encompasses sold state thin film fabrication methods. While the fabrication costs are slightly cheaper than that of monocrystalline silicon, the overall combined costs are still rather large due to the reduced efficiency. This has led to the current development of *third-generation* PV cells. They have been geared to reduce manufacturing costs by making use of earth abundant elements and synthetic methods that can be easily scaled-up at lower costs as well as using solution-based thin film fabrication methods. The *third-generation* PV cells include technologies such as organic solar cells, quantum dot solar cells, dye-sensitized solar cells and most recently perovskite solar cells [8-11]. These new and emerging PV technologies have seen a gradual increase in efficiency as shown in Fig. 1.4. However, to truly capture the market and potentially replace technologies based on traditional energy sources, the efficiencies and cost of these technologies need to improve drastically.

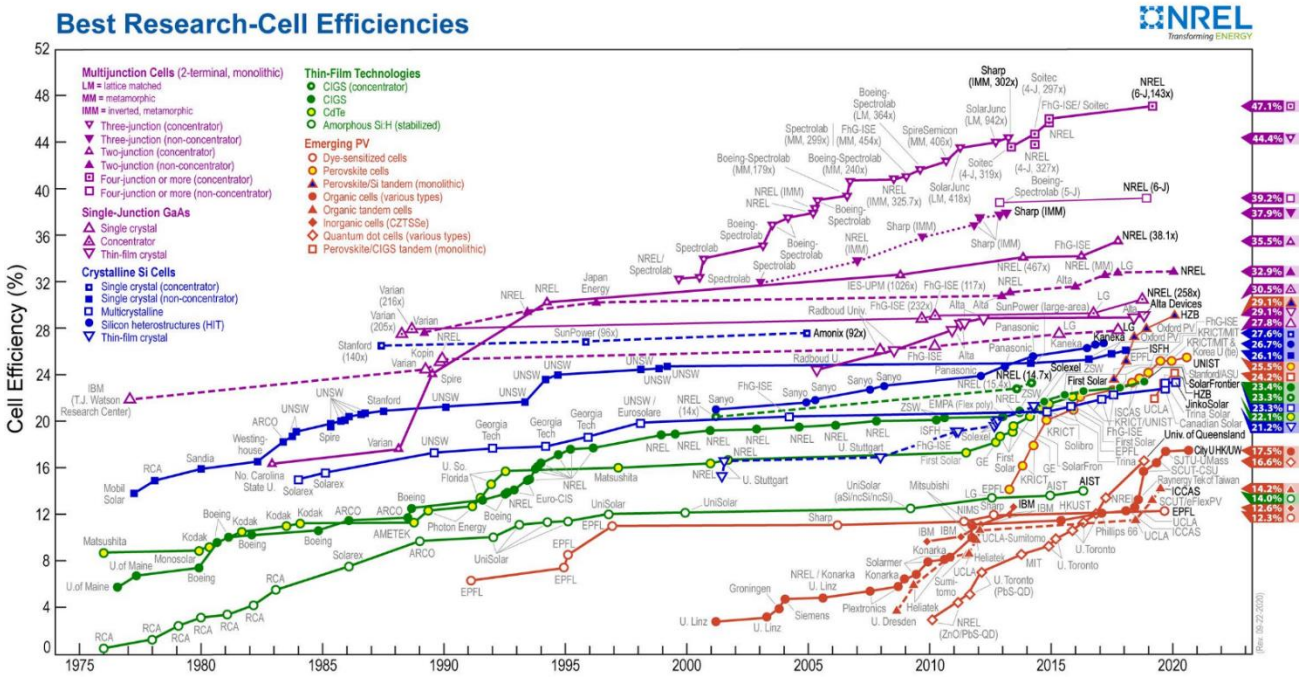

Fig. 1.4: Efficiency chart depicting the most prominent first, second and third generation solar cells [12].

Dye-sensitized solar cells among the emerging technologies are probably the easiest to produce. However, they suffer from a number of disadvantages that reduces their overall efficiencies. These include photo-bleaching of the dye, leakage of the liquid electrolyte and corrosion of the platinum counter electrode in the liquid electrolyte [13, 14]. Therefore, finding new strategies that can overcome these disadvantages is of paramount importance. Herein, of interest, is to find alternative materials that can have similar properties as platinum, however,

be more chemically stable. Lastly, the suggested alternative materials must be easily synthesized and have relative earth abundant elements that are much cheaper than platinum.

1.2. Problem Statement

Platinum is the counter electrode employed in dye-sensitized solar cells. It has high conductivity and high electrocatalytic activity; however, as a noble metal, it is expensive and is prone to corrosion when subjected to the iodide/triiodide electrolyte solution. These limitations speak to the need for the development of affordable counter electrode materials that can withstand the corrosive effect of the electrolyte solution and provide long-term stability to the device. In addition, the efficiency of the currently available material has not surpassed the efficiency of platinum. Therefore, there is a need to develop affordable and efficient material which can be used in all environments.

1.3. Rationale and motivation

Quaternary copper chalcogenide nanoparticles have long been used as components in solar cells particularly as active layers [13]. Most recently, they have been employed as counter electrodes in dye-sensitized solar cells [15]. While cheaper and more stable than platinum in the electrolyte, the electrocatalytic activities are however slightly poor. As such, herein, the use of lithium and sodium-based quaternary nanoparticles (which have not been synthesized using the colloidal method) is proposed for improved electrocatalytic activities. Lithium and sodium-based materials have been shown to have excellent electrocatalytic activities once electrically charged in an application such as batteries due to cation mobility [16]. In addition, unlike platinum, the colloid synthesis of quaternary nanoparticles offers the possibility of tunable properties through the manipulation of size and shape, scalability and the fabrication of the electrodes using solution-based methods such as drop-casting.

1.4. Aim and objectives

The aim of this project was to synthesize quaternary nanoparticles namely Cu_2ZnSnS_4 (CZTS), $Cu_2ZnSnSe_4$ (CZTSe), Li_2ZnSnS_4 (LZTS) and Na_2ZnSnS_4 (NZTS) and use them as counter electrodes in dye-sensitized solar cells.

In order to fulfil the above mentioned aim, the following objectives were set in place:

- To use the hot injection colloidal method to synthesize CZTS, CZTSe, LZTS, NZTS nanoparticles

- To study the effect of the Li/Na precursor, mole ratio, order of addition and the reaction time on the structural, optical and electrochemical properties of LZTS and NZTS nanoparticles
- To use the nanoparticles as counter electrodes in dye-sensitized solar cells

References

[1] https://www.un.org/development/desa/dspd/2030agenda-sdgs.html [Accessed 16 February 2021].

[2] S. Myong, *Recent Patents on Nanotechnology*, 1 (2007) 67-73.

[3] M. Kumar, "Social, Economic, and Environmental Impacts of Renewable Energy Resources," in Wind Solar Hybrid Renewable Energy System, (2020) 1-12.

[4] https://businesstech.co.za/news/energy/105015/how-much-100-renewable-energy-in-africa-would-cost/. [Accessed 13 March 2020].

[5] https://loadshedding.eskom.co.za/loadshedding/description [Accessed 24 February 2021].

[6] A. Aliyu, B. Modu and C. Tan, *Renewable and Sustainable Energy Reviews*, 81 (2018) 2502-2518.

[7] H. Tazvinga, O. Dzobo and M. Mapako, *Journal of Energy in Southern Africa*, 31 (2020) 59-72.

[8] G. Conibeer, *Materials Today*, 10 (2007) 42-50.

[9] G. Gong, S. Darling and F. You, *Energy & Environmental Science*, 8 (2015) 1953-1968.

[10] J. Jean, A. Wang and A. Bulovic, *Organic Electronics*, 31 (2016) 120-126.

[11] D. Aldakov, A. Lefrancois and P. Reiss, *Journal of Materials Chemistry C*, 1 (2013) 3756-3776.

[12] https://www.nrel.gov/pv/assets/pdfs/best-research-cell-efficiencies.20200104.pdf [Accessed: 17 July 2021]

[13] S. Lu, H. Yang, F. Yi, Y. Wang, S. Chen, G. Yang, Y. Liu and X. Zhang, *Scientific Reports*, 8 (2018) 1-7.

[14] D. Cao, X. Li, X. Yu, N. Cheng, P. Yang, B. Mi and Z. Gao, *Physica Status Solidi*, 217, (2019) 1-7.

[15] S. Chen, A. Xu, J. Tao, H. Tao, Y. Shen, L. Zhu, J. Jiang, T. Wang and L. Pan, *ACS Sustainable Chemistry & Engineering*, 3 (2015) 2652-2659.

[16] R. Ruffo, C. Wessells, R.A. Huggins, Y. Cui, *Electrochemistry Communications*, 11 (2009) 247-249.

CHAPTER 2
Literature Review

2.1. Semiconducting nanoparticles

Semiconducting nanoparticles (NPs) have been observed to exhibit unique optical and electronic properties, making them useful in a wide variety of applications when compared to their bulk counterparts. NPs are defined as crystalline material composed of a number of electrons that occupy well-defined and discrete quantum states. Their electronic properties display an intermediate between bulk and discrete fundamental particle [1]. The structural arrangement of the NPs mimics atoms of their bulk (3D) counterparts with diameters in the range of one to one hundred nanometers. The small size increases the number of atoms present on the surface. The energy associated with NPs is reliant on the inversely proportional relationship between the size of the NP and the exciton Bohr radius. It is well documented that the energy difference between the valence band (VB) and conduction band (CB) increases with the decrease in size of the NPs (Fig. 2.1).

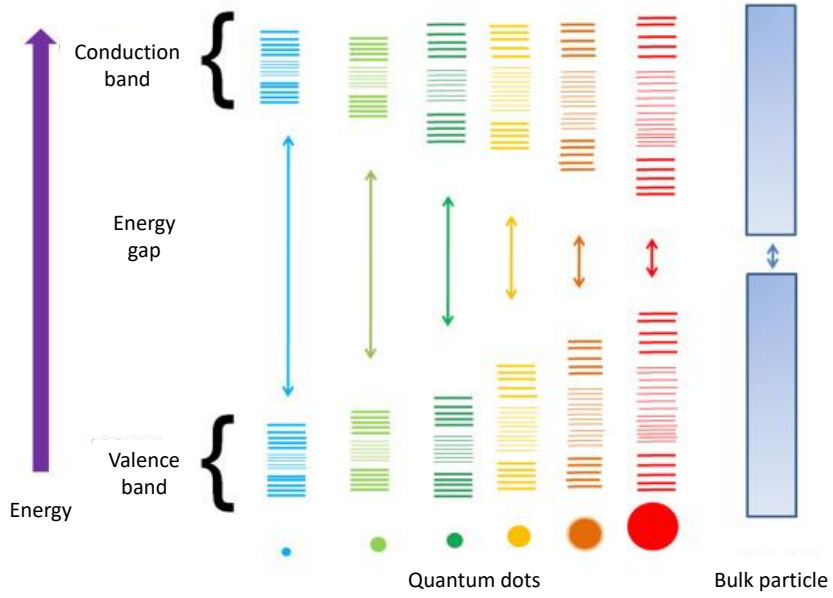

Fig. 2.1: Schematic illustrating the effect of quantum confinement [1].

The colloidal synthesis method plays a crucial role in tuning the size of the NPs ranging from 2D (i.e. quantum wells), 1D (quantum wires) and 0D (quantum dots). This phenomenon can

be explained by quantum confinement, which occurs when the size of the particle is infinitesimal to be comparable to the wavelength of the electron. Another consequence of quantum confinement is the formation of quasiparticles that occur because of the dot boundary. The transition between the electron (in the VB) and quantum-size levels (in the CB) of small semiconducting NPs occurs because of linear and nonlinear optical measurements. Quantum confinement in quantum dots (QDs) can be explained through the parabolic approximation equation 2.1. The energy of the electron and the vacant quantum-size levels can be characterized by angular momentum quantum number *l*, where $m_{e,h}$ represents the electron and hole effective mass respectively, a represents the crystal radius, $\Phi_{l,n}$ represents the *n*th root of the spherical Bessel function [2-4].

$$E_{l,n}^{e,h} = \frac{\hbar^2 \phi_{l,n}^2}{2m_{e,h}a^2} \qquad (2.1)$$

The parabolic approximation equation explains that the total energy of the optical band edge transition will increase with a size decrease in the NP [5]. This is as a result of the quantized size levels of the electron and the hole. Additionally, the modification in size enables the absorption/emission of light across the visible spectrum. This means that the band gaps of the semiconducting material can range from 1.0 eV to 3.0 eV.

The excitation of an electron from the VB to the CB leaves a vacancy in the VB that is positively charged. The energy difference between the VB and CB is the band gap (E_g) that determines the amount of energy required by an electron to reach the CB. The E_g of nanocrystalline material can either be direct (e.g. $CuInGaSe_2$) or indirect (e.g. silicon) (Fig. 2.2), it is possible to have allowed and forbidden direct and indirect transitions. When the conservation of the electronic wave function is observed, it can be attributed to a direct band. Conversely, when the absorption coefficients are small and the transition between the VB and CB is forbidden, it results in an indirect band gap [6]. Unlike binary NPs which have relied on toxic elements, the recent synthesis of ternary and quaternary NPs have the ability to use non-toxic elements to achieve the ideal band gap for their use in electronic applications. Therefore, due to the flexibility in tuning the band gap of ternary and quaternary NPs, there has been an increased interest in synthesizing these materials because they do not rely on toxic elements [6].

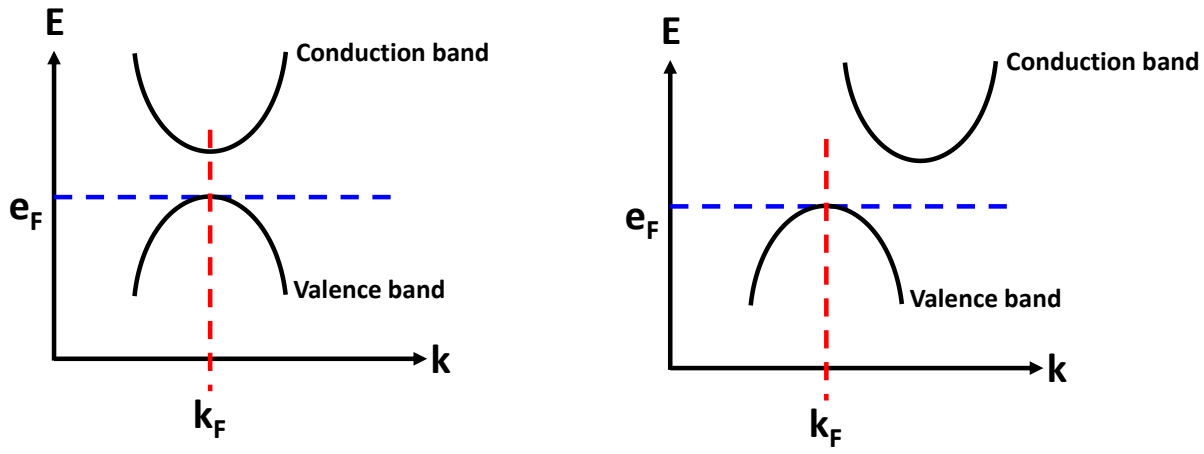

Fig. 2.2: Direct and indirect bandgap illustrations of semiconductors.

2.2 Brief introduction about quaternary nanocrystals

The interest around quaternary nanocrystals has increased over the past decades. Quaternary nanocrystals stem from binary and ternary semiconducting materials that involve the use of toxic heavy metals ranging from cadmium (Cd), lead (Pb) and mercury (Hg) [6]. The development of CdS, CdTe, $CuInSe_2$ (CIS) and $CuInGaSe_2$ (CIGS) became sought after because of the electrical properties displayed. These materials were investigated as p-type semiconducting material with the ability to harvest light in thin film solar cells [7]. The use of CIS and CIGS achieved efficiencies greater than 20% [8]. However, the continued synthesis of CIGS was seen as a potential threat due to the use of scarce elements In and Ga respectively. The introduction of Cu-chalcogenide quaternary compounds was revolutionary, as the reliance on toxic elements gradually ended (Fig. 2.3). This led to the replacement of In and Ga with Zn and Sn as non-toxic and abundant earth elements. The quaternary single crystal structure of Cu_2ZnSnS_4 (CZTS) was first reported by Nitsche in the early 1960s. The CZTS structure was discovered through the growth of crystals using the vapor phase by chemical transport with the iodine method [9, 10].

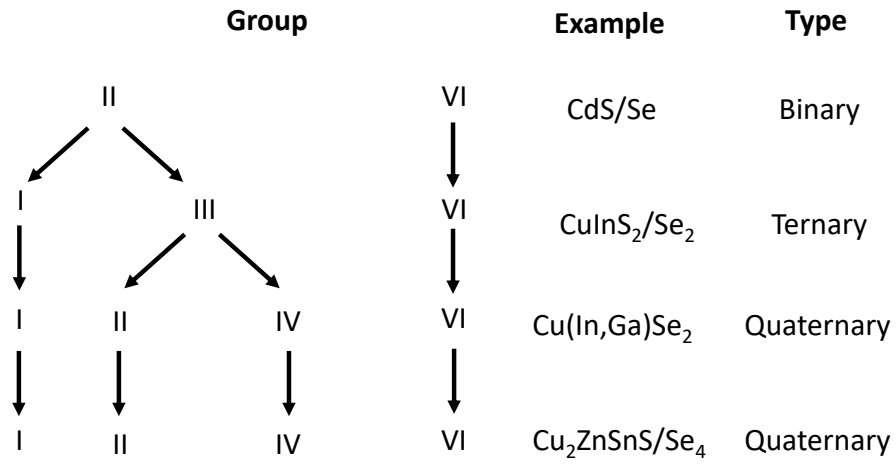

Fig. 2.3: The relationship II-VI, I-III-VI and I-II-IV-VI chemical composition of semiconducting material [6].

The I_2-II-IV-VI_4 chemical composition has been known to represent the following elements: I = Cu, II = Zn, IV = Sn, and VI = S or Se [9]. As observed, various substitutions have been studied for the II, IV cations and VI anion respectively (Table 2.1). In the last decade, the solid-state substitution of copper with silver, lithium and sodium respectively, has been successfully reported [11-16].

Table 2.1: Summary of quaternary nanoparticles and their application/s

Quaternary NP	Ref.	Band gap/PCE	Synthetic Method	Application
The substitution of **I** cation				
Cu$_2$ZnSnS$_4$	[9]	1.5 eV	Solid-state – vapor phase	
Ag$_2$ZnSnS$_4$	[11, 12]	1.5 eV 1.48 eV	Sputtering Colloidal synthesis	Solar cell
Li$_2$ZnSnS$_4$	[13, 14]	1.5-1.9 eV 2.87 eV	Solid-state – grinding Solid-state – ceramic route	Photodiode/Solar cell
Na$_2$ZnSnS$_4$	[15, 16]	3.10 eV 3.32 eV	Solid-state – flux method Solid-state	Nonlinear Optical studies/Solar cell

Quaternary NP	Ref.	Band gap/PCE	Synthetic Method	Application
The substitution of **II** cation				
Cu$_2$**Cd**SnS$_4$	[17]	1.52 eV	Solvothermal	Photovoltaics
Cu$_2$**Fe**SnS$_4$	[18, 19]	1.19 eV 1.5eV	SILAR Solvothermal	PN junction solar cell
Cu$_2$**Mn**SnS$_4$	[19]	1.28 eV	Solvothermal	Photovoltaic cells
Cu$_2$**Co**SnS$_4$	[19]	1.25 eV	Solvothermal	
Cu$_2$**Ni**SnS$_4$	[19]	1.49 eV	Solvothermal	

Quaternary NP	Ref.	Band gap/PCE	Synthetic Method	Application
The substitution of **IV** cation				
Cu$_2$Zn**Si**S$_4$	[20]	2.71 eV	Co-sputtering	Photoelectrochemistry
Cu$_2$Zn**Ge**Se$_4$	[21]	PCE = 5.5%	Solid-state – thin films	Optoelectronics
Cu$_2$Zn**In**S$_3$	[22]	1.20-1.72 eV	Colloidal	Light emitting diodes

Quaternary NP	Ref.	Band gap/PCE	Synthetic Method	Application
The substitution of **VI** anion				
Cu$_2$ZnSn**Se**$_4$	[23]	1.42 eV	Solution – Facile	Solar cells
Cu$_2$ZnSn**Te**$_4$	[24]	0.84-0.88 eV	Solid-state – ball-milling	Photovoltaic cells

The desired quaternary compound has been reported to form impurities therefore, finding the appropriate precursors and optimal reaction conditions is essential. Fig. 2.4 shows the progression towards the formation of quaternary nanocrystals, which are likely to crystalize in the kesterite, stannite and/or primitive mixed CuAu (PMCA) crystal phase. The kesterite and stannite phase are the most dominant phases because they are thermally stable. This group of semiconductors have tetrahedral coordination, which stem from a zinc-blende crystal structure. More specifically, the kesterite crystals are derived from the chalcopyrite orientation while the stannite and PMCA crystals are derived from the CuAu-like orientation [25-27]. The energy difference between kesterite and stannite is approximately 3–5meV/atom [27, 28]. Due to this subtle energy difference, the crystal structures can be distinguished through the space groups. The kesterite phase has I-4 space group, while stannite has I-42m and PMCA has a P-42m space group. The PMCA phase has a 90° rotation in one of the II-IV layers, which distinguishes it from the other two structures [25, 27, 29]. However, this distinction is not easy to identify.

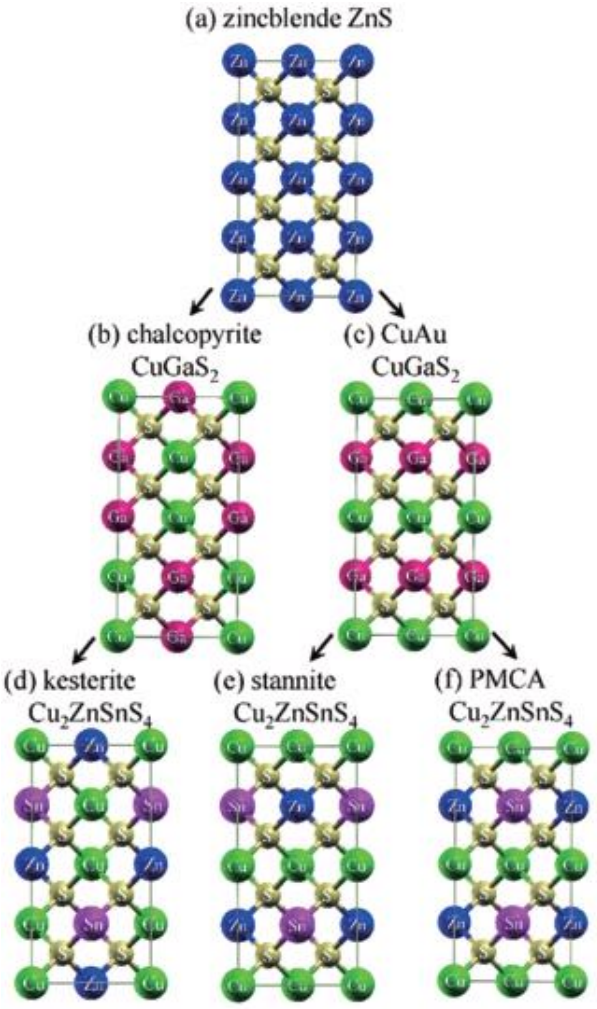

Fig. 2.4: The progression of the crystal structures from binary to quaternary semiconducting nanocrystals [30].

2.2.1 Copper Chalcogenides

The development of bulk material (i.e. CZTS) has resulted in low conductivity and photo-response in photovoltaic (PV) application. Therefore, the synthesis of nanocrystals has shown to improve the performance of optoelectronic devices. Cu_2ZnSnS_4 (CZTS) and $Cu_2ZnSnSe_4$ (CZTSe) as quaternary semiconducting nanocrystal chalcogenides were developed as alternative absorber material for PV applications. Kattan *et al.* has reported that, the crystal defects have a direct impact on the carrier transport and the lifetime in the absorber layer [29]. In addition, the optimal band gap 1.0 – 1.5 eV, high absorption coefficient and ease of synthesis make these materials favourable for application in PV cells [24, 31, 32].

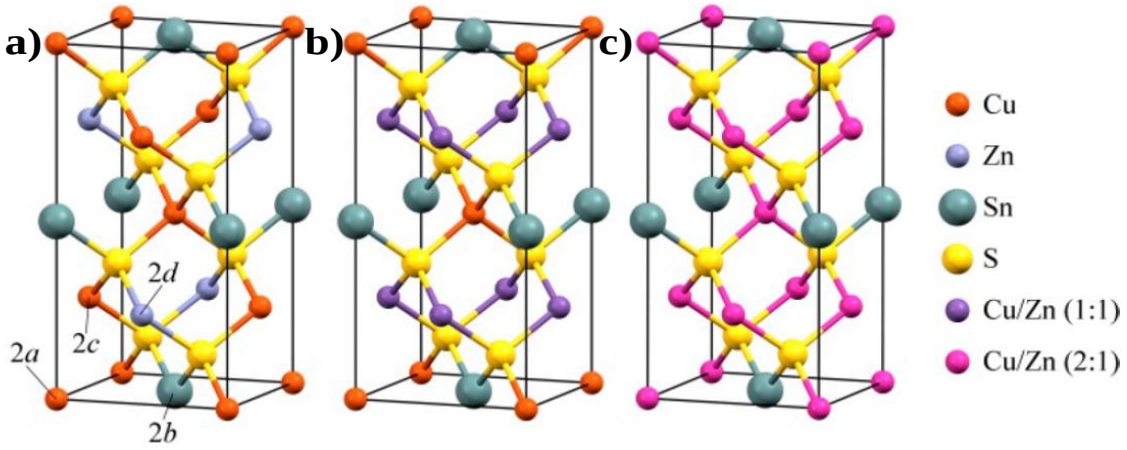

Fig. 2.5: The crystal structures of CZTS in the kesterite (a), half-disordered kesterite (b) and fully disordered kesterite (c) [32].

CZTS and CZTSe nanocrystals experience a few similarities in structural, optical and electrochemical properties. The crystal structure has been reported in the traditional kesterite phase, where the Wyckoff positions (i.e. 2a, 2b, 2c and 2d) are reported as shown in Fig. 2.5a. The Wyckoff positions help keep track of crystal defects in the crystal structure. In Fig. 2.5b, a 1:1 ratio Cu/Zn disorder is observed and results in a half-disordered kesterite crystal structure. While Fig. 2.5c exhibits a 2:1 Cu/Zn ratio which is indicated as a fully disordered kesterite structure. The Cu_{Zn} crystal defect in the structural arrangement of CZTS results in the inevitable p-type nature of the Cu-chalcogenides. Therefore, the replacement of Cu_{Zn} defect with the copper vacancy (V_{Cu}) results in the increased presence of zinc, which has been reported to result in the best solar cell device performance [32].

2.2.2 Mixed Chalcogenides

$Cu_2ZnSn(S,Se)_4$ (CZTSSe) is an alloy/derivative of CZTS and CZTSe nanoparticles first reported around 2009 [33, 34]. The crystal structure is observed to be similar to the CZTS/Se nanoparticles with alternating sulphur and selenium atoms respectively. Beyond the structural properties, CZTSSe has been observed to exhibit improved optical and electrochemical properties. The CZTSSe have been synthesized using the two different methods namely, non-vacuum based and vacuum-based [33, 35]. The highest recorded power conversion efficiency (PCE) for CZTSSe is 12.6% using non-vacuum based synthetic methods and while vacuum-based methods have reported a 12.3% PCE [33, 35]. One of the non-vacuum methods include the fabrication of CZTSSe thin-films using the sulfo-selenization process with approximately 200 mg selenium solid and H_2S gas with a reported efficiency of 12.62% [36]. One of the

vacuum-based methods include the fabrication of CZTSSe deposited via sputtering and nealed with Se and SeS_2 [35]. However, the lack of increase in PCE of the CZTSSe nanoparticles has been reported to be due to the presence of secondary phases, defects and band grading [31, 37].

Beyond the improved optical and electrochemical properties exhibited by CZTSSe, the inherent Cu_{Zn} defect still exists and reveals disordering issues observed in the CZTS nanoparticles. Attempts have been made to resolve this defect through longer annealing times however, not much progress has been made. In light of this, substitution of the cations has been explored. Gershon *et al.* has reported on the partial substitution of the monovalent cation with Ag^+ [38]. However, the inversion in the semiconductor type is observed for the $Ag_2ZnSnSSe_4$ as n-type as opposed to the conventional p-type observed in the Cu-based semiconductors. Other reported mixed chalcogens are the partial substitution of zinc (Zn) with cadmium (Cd), manganese (Mn), iron (Fe), cobalt (Co) and barium (Ba) respectively [38, 39]. The partial/complete substitution was employed to create a mismatch in the monovalent and divalent elements. The substitution helps reduce the antisite defects, the associated band tailing and improves PCE of the mixed chalcogenides.

2.2.3 Doping/Alloying

The mechanism of doping/alloying has shown to have advantages in improving device performance by altering the electric conductivity of semiconducting material and reducing defects such Cu_{Zn} and Zn_{Cu} antisites in CZTS material. The incorporation of alkali metals into quaternary materials and their derivatives was first discovered over 20 years ago through sheer serendipity when soda-lime glass was used as a substrate for a solar cell device [40]. The incorporation of sodium through doping resulted in the increase in grain size and charge-carrier properties [41, 42]. Similarly, the incorporation of lithium through either doping or alloying has been reported to increase grain size, similar to sodium doping and in addition an increase in the band gap [43]. Lithium doping has also been reported to minimize charge recombination at the interface of the solar device [44].

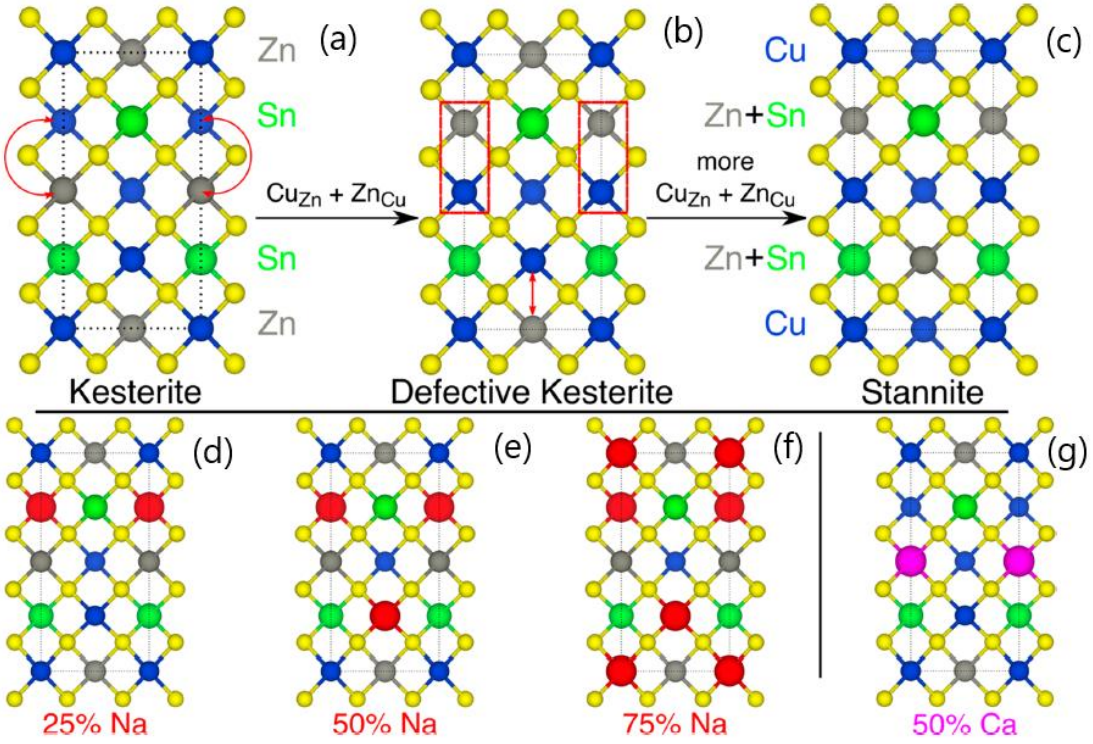

Fig. 2.6: The illustration of the kesterite, defective kesterite and stannite structure of CZTS (a-c); Na-doped kesterite (d-f) and Ca-doped kesterite (g) crystal structures at varying concentrations of the dopant [45].

Berman *et al.* predicted the modification of the local structure (Fig. 2.6) with isovalent dopants (i.e. Na and Ca) of the kesterite crystal phase using DFT calculations, at varying concentrations [45]. The doped kesterite (KS) material were shown to partially replace Cu^{+} with Na^{+} and Zn^{2+} with Ca^{2+} respectively. Furthermore, the DFT calculations predicted that 50% was the threshold-limit of the amount of dopants that could be introduced. Therefore, it was imperative to control the concentration of the dopant. This method can pose a few unknowns during the experimental method process. It has been suggested that over-doping with Na, can induce unwanted phase separation such that Na_2ZnSnS_4 co-exists with Cu_2ZnSnS_4. In addition, undesired secondary and ternary phases (i.e. Cu_2SnS_3/CaS) could form upon large introductions of Ca. Similar to Na doping,Ca doping can cause marginal changes on the band gap of the KS structure [45]. Regardless of the doping limitations, the doping/alloying of the quaternary materials, has influenced the replacement of the monovalent cation in the I_2-II-IV-VI_4 crystal structure.

2.2.4 Monovalent cation replacement of Cu to Li and Na

Among doping, lithium and sodium have been used in the production of rechargeable batteries. The use of alkali metals has shown good electrical and conductive properties, making them excellent candidates for application in energy storage and photovoltaic devices. The Cu_{Zn} antisite has been one of the limiting parameters in the CZTS nanocrystals. Therefore, the observed change in the monovalent cation from Cu^+ to Ag^+ has shown improved properties in the quaternary nanocrystals. The replacement has been observed to drastically reduce the antisite disordering in AZTSe in comparison to CZTSe [46]. This is due to the increase in ionic radii from 0.77 Å for Cu^+ to 1.15 Å for Ag^+. The ionic radii of lithium (Li^+) and sodium (Na^+) are 0.90 Å and 1.16 Å respectively. The increase in the ionic radii of Li^+ and Na^+ make lithium and sodium good potential replacements for the monovalent cation. The bulk LZTS and NZTS material have been synthesized through solid-state methods [13 – 16]. The material have shown to exhibit semiconducting behaviour through their structural, optical and electrical properties results. Herein, the colloidal synthesis of L/NZTS akin to CZTS/Se nanocrystals is reported for the first time.

2.2.5 Electronic Band structure of KS, ST and PMCA

Upon changes on the crystal structure, it is important to study the band structure of the new nanocrystals. The band structure (Fig. 2.7) reveals the parameters and band energies shown along the symmetry lines in the Brillouin zones [47]. In addition, the band structure explains the physical properties of solids and forms the foundation of all solid-state devices [47, 48]. Conversely, the Brillouin zone is the minimum unit cell of a periodic structure. To further understand the electronic band structure of crystalline material, the three phases of Ag_2CdSnS_4 were investigated. In Fig. 2.7, Saidi *et al*. have reported the electronic band structures of Ag_2CdSnS_4 calculated from PBE-GGA (Fig 2.7a) and mBJ-GGA (Fig 2.7 b) computer modelling approximations for the three different phases [49]. At first glance, the material appear to have the same band structures. However, a closer look at the symmetry lines, subtle differences are observed which distinguish the three phases from each other. From the band structure, the Γ point which relates to k = 0, the conduction band (CB) minimum and valence band (VB) maximum are observed. It is at the Γ point where the direct band gap is observed for each phase. Saidi *et al.* reported that the mBJ-GGA band gap approximations, were in good agreement with previously reported research. Furthermore, the band gap energies shown indicate that the material can be applied as a future absorber layer material.

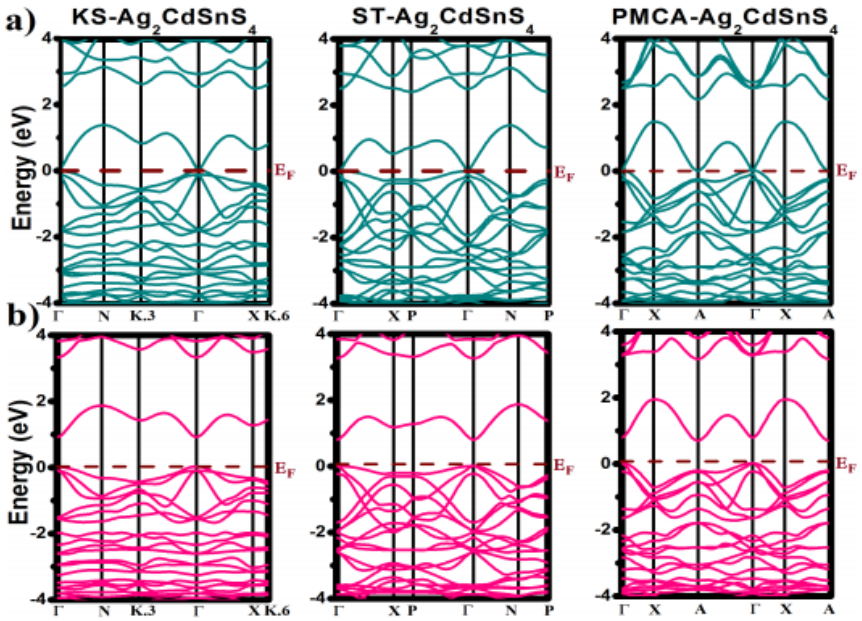

Fig. 2.7: The electronic band structure of the KS, ST and PMCA Ag_2CdSnS_4 using PBE-GGA (a) and mBJ-GGA (b) approximations [49].

The I_2-II-IV-VI_4 crystallizes in the kesterite (KS; space group I4), stannite (ST; space group I42m), or primitive mixed Cu-Au (PMCA; space group P42m) crystal structures and these are shown in Fig. 2.8.

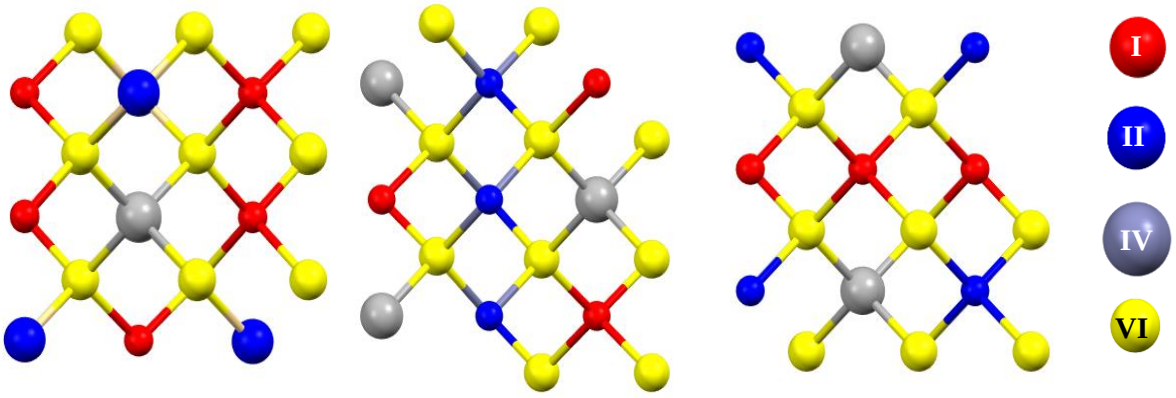

Fig. 2.8: The kesterite, stannite, and PMCA crystal structures of quaternary nanoparticles.

Kesterite (KS) and stannite (ST) are body-centered tetragonal crystal structures with c ≈ 2a and may be understood as two VI elements face-centered cubic (FCC) lattices stacked on top of each other with I, II, and IV elements occupying half the tetrahedral voids within this FCC lattice. The PMCA structure is primitive tetragonal with c ≈ a as shown in Fig. 2.8 [27]. The tetrahedral voids are prone to produce three different structures which arise from the varied arrangement and stacking of the metal cations. The KS structure consists of two interchanging cation layers each containing I and II or I and IV elements respectively, whereas in the ST and PMCA structures, the layers consist of I elements which alternate with a layer of II and IV elements respectively. In the ST structure, the II and IV atoms situated on the same layer switch their positions every second layer that proceeds. Notably, the interchanging between II and IV, on every other layer, is not present in PMCA, cementing its primitive tetragonal lattice and differentiates it from the ST structure [27]. The X-ray diffraction of these structures are very similar with only small distinguishing features. The kesterite phase is usually 0.2° shifted from stannite and PMCA due to the larger distortion of the latter. The stannite and the PMCA are largely undistinguishable; however, the stannite is a more stable phase [50]. The XRD experimental data is used to calculate the lattice constants a, b and c by using equation (2.2) and matched to the reference constants, thus distinguishing the two phases. The lattice constants for CZTS are shown in Table 2.3.

$$\frac{1}{d^2} = \frac{h^2 + k^2}{a^2} + \frac{l^2}{c^2} \qquad (2.2)$$

Table 2.3: Lattice parameters of tetragonal CZTS structures [27].

Structure	a = b (Å)	c (Å)	c/a	Type
Kesterite	5.443	10.786	1.982	Simulation
Stannite	5.403	10.932	2.023	
PMCA	5.400	10.942	2.026	
Kesterite	5.432	10.840	1.996	Experimental
Stannite	5.426	10.810	1.992	

2.3 Synthetic methods for quaternary nanocrystals

Among the *third generation* materials, there are wide ranges of quaternary semiconducting nanocrystals, which are promising candidates for photovoltaic applications [19, 50]. Quaternary semiconducting materials have been synthesized using top-down and bottom-up (Fig. 2.9) methods. The top-down methods involve the fragmentation of bulk precursors into smaller parts to form NPs [52-54]. The methods include ball-milling, laser printing and/or ablation, lithography and roll-to-roll nano imprint lithography [24, 52-56]. Conversely, the bottom-up NP synthesis approach involves both physical and chemical processes, where the reaction occurs from their molecular/ionic/atomic precursors. The bottom-up approach encompasses both solid-state and solution-based methods such as chemical vapour deposition, sol-gel, laser pyrolysis, thermal decomposition and the colloidal synthesis method [57]. The bottom-up methods are the most sought-after because they allow better control of the size (i.e. 2 – 10 nm), morphology, defects and chemical composition of the desired NPs.

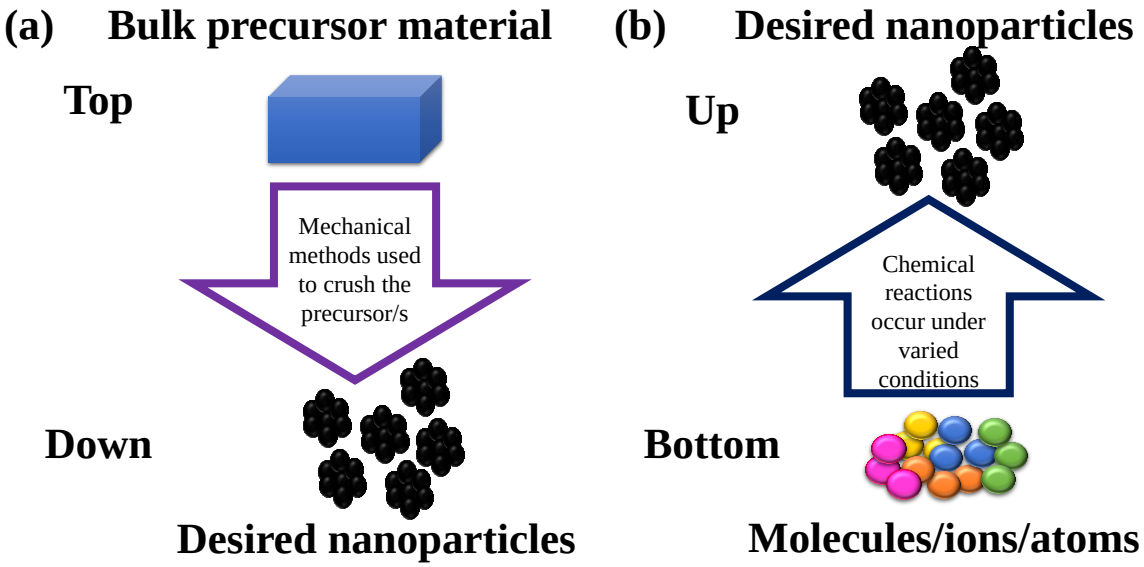

Fig. 2.9: The top-down (a) and bottom-up (b) synthetic reaction illustrations.

2.3.1 Solid-state synthetic methods

For decades, solid-state synthetic methods have been used for the synthesis of bulk crystalline material. There are various solid-state methods that have been used. The first is a chemical vapour transport that involved growing crystals by reacting the desired precursors in a sealed quartz tube above 1000°C in the presence of 5 mg iodine/cm^3. In addition, various iodide gases were used to transport the crystals at a 750 – 800°C gradient [9]. Thermal decomposition of

reactive precursors which occurs at extremely high temperatures [58]. The second is the dry grinding method which involves the grinding of solid hydrazine/cellulose with metal oxides and metal acetates at ambient temperature [58]. The third is the dry milling process which involves the use of tungsten carbide balls, milling pot and precursor material which are combined with the corresponding reactants under inert gas i.e. Argon/Nitrogen. The ball-to-powder mass ratio various along with the milling speed and time [59]. Solid-state methods require the use of either high temperatures over extended periods of time which could decompose the desired compound and they can sometimes make use of highly toxic compounds like hydrazine.

2.3.2 Solution-based synthetic methods

On the other hand, solution-based synthetic methods for synthesizing quaternary semiconducting nanocrystals have received much attention. They are among the most attractive synthetic techniques because of the ability to control the size, composition, shape and crystallite phase (Fig. 2.10). In addition, the solution-based methods are low-cost and reproducible in large-scale. Size control can be determined by the reaction time. Precursor ratio and reactivity determine the composition of the nanomaterials. Surfactants and reaction conditions control the shape. In addition, the surfactant and precursor reactivity help, determine the crystallite phase of the nanocrystals. Recently, solution based methods have been used to synthesize materials that can be used as counter electrodes in DSSCs.

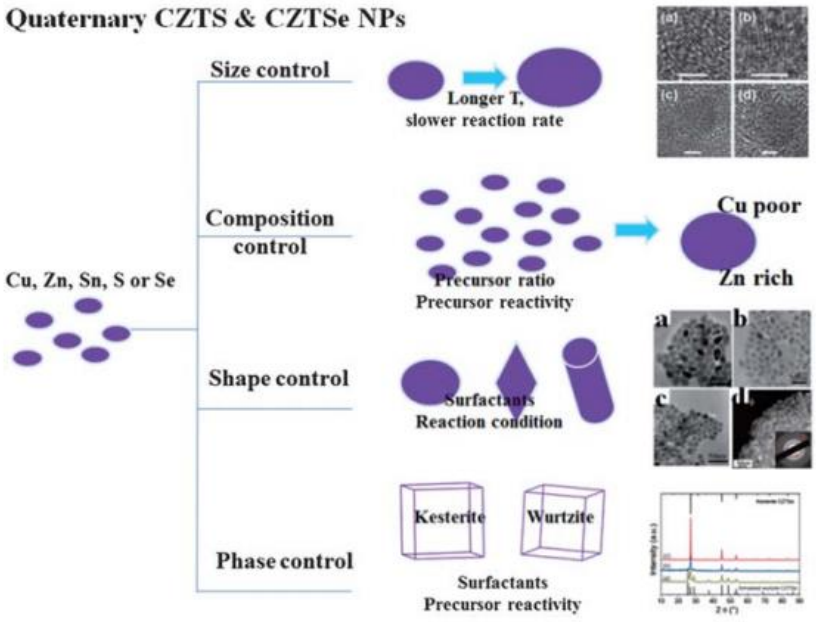

Fig. 2.10: Schematic diagram illustrating parameters used to control the synthesis of quaternary semiconducting nanoparticles [60].

2.3.3 Colloidal synthesis

The solution-based colloidal synthesis method has evolved from the use of hydrazine (toxic and explosive) to hydrazine-free routes (i.e. organic surfactants) towards the desired quaternary semiconducting NPs. The colloidal method is flexible and makes use of various metal salt precursors, high boiling point organic solvents, temperature and time. The flexibility of this method extends to the use of a variety of techniques ranging from hot-injection/hot-adddition, heat-up or microwave assisted solvothermal method to achieve the preferred NPs based on the desired application [36]. Optimizing the parameters of the reaction helps control the nucleation and growth process involved. The ability to control nucleation and growth can lead to uniformed NPs for the intended application.

2.3.3.1 Nucleation

The nucleation phenomenon is best described as the first phase of a thermodynamic model. It describes the formation of the metastable primary phase of the nucleus [61]. The nucleation process is best described by the classical nucleation theory (CNT) which was reported over 70 years ago by Becker and Döring [62]. During the chemical reaction, the CNT maximizes the available entropy in the system. The CNT makes use of the surface energy of the NPs where two processes can be observed [61, 63]. The first process is the homogenous nucleation, which

occurs randomly and spontaneously ($\Delta G<0$) in the presence of a supersaturated state. The second process is the heterogeneous nucleation, which occurs on the nucleation sites on the solid surface of the particles and while the particles are in contact with the solution at either liquid or gaseous state.

The LaMer model of particle formation is an extension of the classical nucleation theory. It was first reported by LaMer and Dinegar, in the 1950s for the syntheses of nanoparticles [64]. The process prides itself on the separate nucleation and growth process, to control the size of the NPs. The LaMer diagram illustrated the three steps involved in nucleation and growth of NPs. The precursors are dispersed/dissolved in a high boiling solvent which reacts to form monomers (Fig. 2.11). At the critical supersaturation level (C_S), the monomers increase and the reaction progresses towards critical nucleation level (C_{min}). Just above this point, critical limiting supersaturation (C_{max}) is reached and nucleation is suppressed causing the curve to drop. The sudden drop is as a result of the consumption of the precursors for the growth of generated nuclei [61, 65].

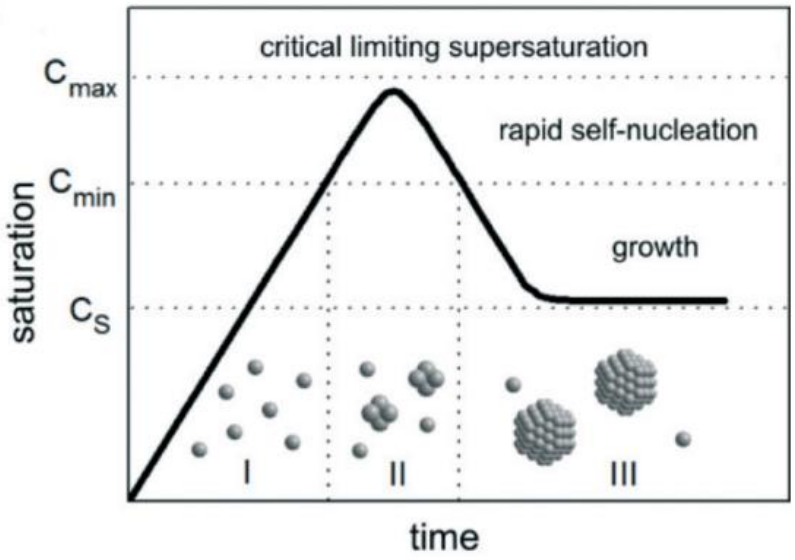

Fig. 2.11: The LaMer nucleation and growth diagram [61].

2.3.3.2 Growth

Once the growth phase is reached, the nuclei of the particles continue to grow with no additional nucleation. The growth mechanisms can occur through diffusion limited growth, aggregation and/or Ostwald ripening. Among these mechanisms, aggregation and Ostwald

ripening are the most reported. Diffusion limited growth occurs as a result of Brownian motion, which forms aggregates. Aggregation cannot be easily disrupted because of the strong covalent/metallic bonds formed between nanoparticles. Ostwald ripening occurs when small particles/droplets disappear by the process of dissolution and deposition on larger particles/droplets. Alternatively, nucleation and growth can occur simultaneously as described by Watzky and Finke [63]. The backbone of the proposed mechanism by Watzky-Finke, is the CNT. The two-step process occurs without any diffusion control. They propose a gradual nucleation process (equation 2.3) subsequent to autocatalytic growth (equation 2.4) on the surface of the NPs.

$$A \rightarrow B \qquad (2.3)$$

$$A + B \rightarrow 2B \qquad (2.4)$$

2.3.3.3 Effect of time

The growth process of any reaction occurs over time. Therefore, the effect of time during colloidal synthesis can have a direct impact on the size of the NP. Prolonged reaction times have the ability to increase the NP size. Qi *et al.* studied the effect of time on $CuInS_2$ NPs and this resulted in the red-shift (towards the NIR region) absorption spectra as shown in Fig. 2.12 [66]. They reported that the diameter of the NPs was controlled by the reaction time.

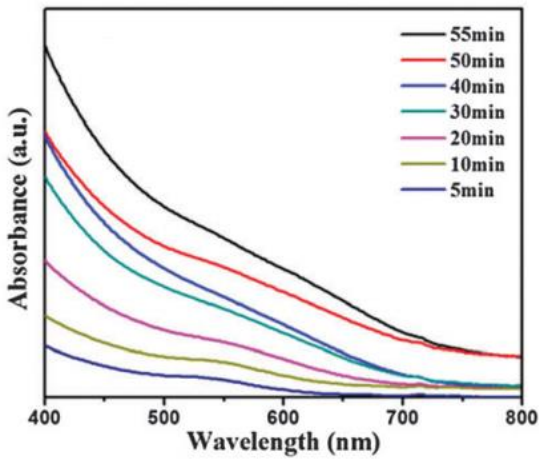

Fig. 2.12: The UV-vis spectra of $CuInS_2$ nanocrystals at different reaction times [66].

Apart from size, the effect of time can also have an impact on the full formation of the desired NPs including its shape. Ibanez *et al.* studied the effect of time on the synthesis of $Cu_2CdSnSe_4$

NCs [67]. When their reaction had reached the desired temperature of 200 °C, aliquots were taken and studied. Their results indicated that after ten seconds, spherical $Cu_{2-x}Se$ nanoparticles (Fig. 2.13 A) had formed, subsequently aliquots at one (Fig. 2.13 B), two (Fig. 2.13 C) and five (Fig. 2.13 D) minutes were taken resulting in a change in morphology to tetrahedral $Cu_{2-x}CdSnSe_4$ nanoparticles. They also reported the change in crystal phase from cubic to stannite. Time does not only influence the shape of the NPs however, when multicomponent elements are involved, the shape and crystal phase of the NPs need to be taken into consideration prior to terminating the reaction.

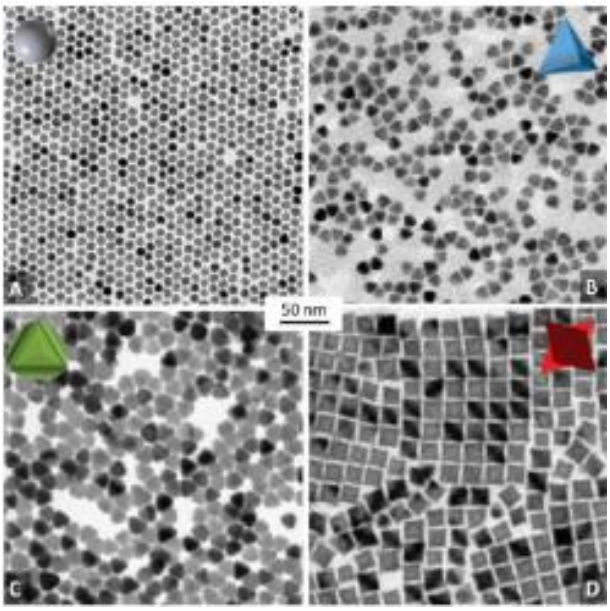

Fig. 2.13: The TEM images depicting the effect of time on quaternary nanoparticles [67].

2.3.3.4 Effect of temperature

Zhang *et al*. 2011 used the hot injection method to illustrate the effect of temperature while synthesizing Cu-Zn-In-S nanoparticles [68]. The NPs ranged from 2 nm to 7 nm when the temperature was changed from 150 to 240 ˚C in 30 °C intervals. Similarly to time, the increase in temperature influences the increase in NP diameter. The change in diameter can be traced through optical analysis, where a gradual red-shift is observed (Fig. 2.14). The red-shift will appear regardless of the presence of a prominent excitonic peak [68, 69]. One of the most common outcomes observed from change in reaction temperatures, is the reduction of impurities at temperatures greater than 140 °C. Therefore, determining the optimal temperature is crucial for the synthesis of the desired particle size.

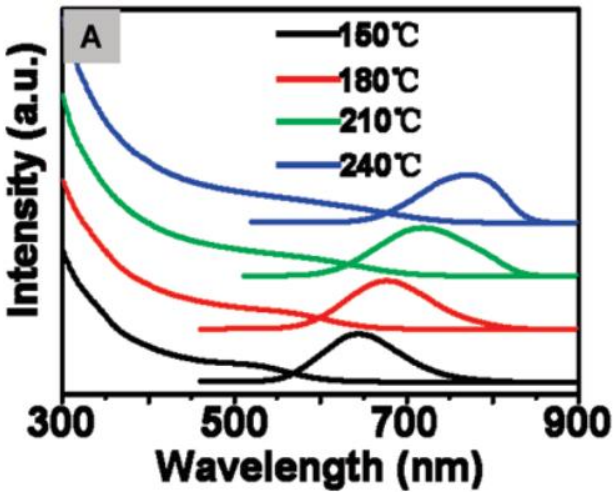

Fig. 2.14: UV-vis and photoluminescence spectra of Cu-Zn-In-S nanocrystals at different reaction temperatures [68].

2.3.3.5 Effect of precursors

Amidst the time and temperature influences, the precursors need to be considered in the study of nanoparticle syntheses. When precursors undergo decomposition, they form monomers which increase until the nucleation is complete and growth of the NPs is achieved. The selection of the precursors for the synthesis of crystalline NPs is crucial. The rate of reactivity and decomposition have an impact in the final morphology and size of the NPs [70, 71]. This is as a result of anisotropic and isotropic growth of the NPs. Anisotropic growth (i.e. nanowires/nanorods) favours the kinetic control which occurs when a high flux of the monomers react. Under kinetically controlled conditions, the rate of growth will depend on the reaction rate between the incoming monomer and the surface sites [72, 73]. Conversely, the isotropic growth (i.e. spheres) favours the thermodynamic control which occurs when a low flux of monomers react. The reactivity of the monomers can be mathematically represented by the following equation:

$$P \xrightarrow{k_f} M \qquad (2.5)$$

Where P represents the precursors, k_f represents the rate of formation or rate constant and M represents formed monomer after the decomposition process [73, 74]. During a first order reaction, the rate constant relies on the temperature and activation energy (E_a) and similarly, it can be represented by the following mathematical equation which incorporates the Arrhenius equation:

$$\frac{d[M]}{dt} = -\frac{d[P]}{dt} = Ae^{\left(\frac{-Ea}{RT_v}\right)}[P] \qquad (2.6)$$

The pre-exponential factor is denoted by A, temperature of the solution is denoted by T_v and the activation energy is denoted by E_a. Tabulated below are the three proposed mechanisms that can be used to predict the type of NPs that can occur [73, 74].

Table 2.2: Summary of three mechanisms to form ideal NPs.

Details	Mechanism 1	Mechanism 2	Mechanism 3
Reactivity	High	Moderate	Low
Activation Energy	Low	Medium	High
Binding energy of the ligand	Low	Moderate	High
Ideal temperature to activate monomers	Low or ambient	Slightly high	High
Formation of monomers	Occurs rapidly and results in high nucleation and growth rates	Occurs rapidly but is short-lived, then growth occurs thus, the rate of nucleation and growth are equivalent	Occurs slowly which results in the slow formation of the nuclei thus, prone to forming a mixture of small and large nuclei. Prone to Ostwald ripening
Yield	Low	Good	Low
Broad Size Distribution	Broad	Narrow	Broad

The successful synthesis of the NPs relies on the monomers to react at the ideal solution temperature and activation energy. Therefore, mechanism 2 is proposed to be the best method to follow to ensure the best engineered NPs.

2.3.3.6 The effects of precursor addition and molar ratios

Following the choice in precursor type, the order in which the precursors are added during a reaction plays an important role in the morphology, size and formation of the desired NPs. The

ternary and quaternary synthesis of NPs is known for the formation of secondary phases as well as impurities, which limit their full potential during application studies. Therefore, researchers have embarked on studying the order of precursor addition with the intention of synthesizing pure-phase NPs.

Ntholeng et al. have reported the effects of precursor addition during their synthesis of $CuInTe_2$ nanoparticles [75]. The synthetic approach studied two methods where the first method involved the simultaneous reaction of the two less reactive precursors (i.e. In and Te) followed by adding the highly reactive Cu-precursor at the elevated temperature of 250 °C then the NPs were allowed to grow. They reported that the addition of CuCl, induced supersaturation of the reaction mixture and as a result rapid nucleation and growth desired $CuInTe_2$ NPs occurred successfully. The second method involved the sequential addition in the order $InCl_3$ → Te → CuCl. The sequential addition was reported to exhibit more homogeneity and resulted in cubic NPs. On the other hand, the simultaneous reaction synthesis resulted in mixed morphologies and impure phases [75]. Similar studies were also reported by Guo *et al.* where the precursor addition of the ternary $CuInSe_2$ NPs were studied [76]. In summary, Guo and co-workers demonstrated that the precursor addition influences the crystal phase of the NPs. They reported that the chalcopyrite (stable phase) was achieved during the simultaneous addition of the specific precursors. Conversely, when the selenium chalcogen was added at elevated temperatures, the sphalerite (unstable phase) was formed. In addition to the varying crystal phases, it was reported that the change in precursor addition had a direct influence on the morphologies and properties of the NPs. These two studies are proof that the effects of precursor addition can help in engineering the desired NPs and better understand the mechanism of how the NPs are formed.

2.3.3.7 Effect of capping agents

The use of capping agents or lack thereof, has evolved over the years. Capping agents stem from the simple adsorption phenomenon that is best described by the Langmuir isotherm equation (2.7) which indicates that the surface adsorption is driven by the concentration of the absorbate in the bulk solution or the strong binding of the adsorbate to the surface of the material [77].

$$\theta = \frac{KC_{bulk}}{KC_{bulk} + 1} \qquad (2.7)$$

Where θ is the fraction of the surface sites occupied by the adsorbate molecules, K is the equilibrium constant of the adsorption and C_{bulk} is the concentration of the adsorbate in the bulk solution.

However, the mechanism of the capping agents is slightly different as it involves stronger covalent bonding. The review by Yang *et al*. dates back the use of capping agents from the traditional poly(vinyl pyrrolidone) which was first used as a stabilizer in the synthesis of NPs [77]. They then look at the evolution from the traditional to the more modern techniques which eliminate the use of capping agents. The first technique was the use of halide ions, which have the ability to surround the metal nanoparticles through covalent bonding in order to avoid/limit the use of capping agents. Secondly, was the combined use of a capping and reducing agent or even the sole use of reducing agents (i.e. citrate or citric acid) as capping agents. Thirdly, was the combination of capping agents with seed-mediated growth for the purpose of obtaining varying shapes/structures that would not be possible in a one-pot synthesis method. The last techniques was to not include the capping agent or removing the capping agent after synthesis, in the efforts of improving the catalytic performance [77].

There are various methods which use the multifunctional role of capping agents as colloidal stabilizers, reducing agents, solvent, prevent agglomeration, inhibit uncontrolled growth and provide modification which has an influence in the application of the nanoparticles [78-80]. A variety of capping agents exist from polymers, peptides, small ligands and surfactants. Polymers are often used in biomedical research, while small ligands are often used to replace long chain capping agent post synthesis. The use of surfactants such as long chain hexadecylamine (HDA), oleylamine (OLA), oleic acid (OA), ethylene glycol and 1-dodecanethiol (1-DDT) but not limited to, are among the commonly used in colloidal syntheses for application in photovoltaics, sensing, photonics, catalysis, optoelectronics and LEDs. The capping agents have a strong binding affinity to the surface of the nanoparticle. In this work a combination of surfactants were used however, OLA yielded the best nanoparticle results, as such it was used as the capping agent, solvent and stabilizer in the syntheses of the quaternary NPs.

2.4 Application of quaternary nanocrystals

Quaternary nanocrystals have been widely used as absorber layers in thin-film solar cells [59], window materials in multi-junction photovoltaic cells [51], and memory devices [81], optoelectronic devices [6] and QD-LEDs [22]. The newly developed size, shape and/or composition of the nanocrystals change their properties from their bulk counterparts, making them ideal candidates for photovoltaic application. Once electrical, optical, absorption coefficient and the direct band gap energy have been determined, the materials can be applied in thin-film solar cell applications. Similarly, to a variety of synthetic methods, there are several device assembly methods that can be used to fabricate solar cell devices. These methods include vacuum and non-vacuum based methods that have been reported thus far. The vacuum methods include sputter-coating, metal deposition and sulfurization. Among the non-vacuum fabrication methods, the solution-based techniques are known to be low-cost and have ease of processing. These non-vacuum fabrication methods include successive ionic layer adsorption and reaction (SILAR), spin-coating, dip-coating and drop-casting of nanomaterial inks. For the purpose of this study, solution-based synthetic methods and non-vacuum methods (drop-casting) were used for the fabrication of the dye-sensitized solar cell device.

2.4.1 Device: Dye-Sensitized Solar cell

Dye-sensitized solar cells (DSSCs) have arisen as a technically and economically credible alternative to the p-n junction photovoltaic devices. The mesoscopic property of the DSSC enable the absorption of more incident light owing to the large internal surface area [82]. The general mechanism of DSSCs is to divide its function of light absorption from charge carrier transport. The separate components of the DSSC make use of less raw materials to the costs associated with fabricating the device. Furthermore, DSSC have the ability to accept radiative light from both indoor (i.e. fluorescent light) and outdoor (i.e. sunlight) [82]. The dual function ensures the device can be used indoors and/or outdoors. Lastly, the progress made on DSSC makes it worthwhile to continue studying and finding alternatives to the fabrication material, techniques and improve its performance.

2.4.1.1 Architecture of a DSSC

Quaternary semiconducting nanoparticles have been recently used as alternative electro-catalysts to platinum catalysts in DSSCs. A typical DSSC device (Fig 2.15) undergoes a particular mechanism as briefly described below.

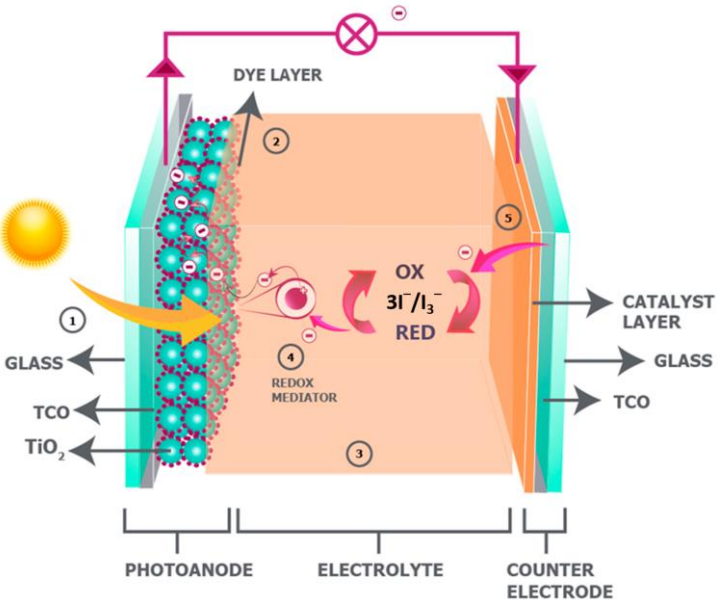

Fig. 2.15: Schematic of the components of a dye-sensitized solar cell [83].

2.4.1.2 Mechanism

Light passes through the transparent anode electrode and excites the dye molecules. The excited dye molecules inject electrons into the TiO_2 layer, which acts as a semiconductor. It is worth noting that the electrons originate from the dye upon absorption of light. The injected electrons flow through the external circuit towards the cathode electrode. The cathode electrode makes use of light-absorbing nanocrystals to increase the effective surface area and allow more light over a wider range of the visible spectrum to be absorbed. This allows the DSSC to absorb more light under cloudy conditions when compared to silicon-based photovoltaic cells. The electron from the external circuit further allows the flow of the electrons into the iodide/triiodide electrolyte. The electrolyte is responsible for transporting the electrons back to the dye molecules. Amidst the process, the dye is oxidized by receiving an electron from the iodide ion, which reduces the dye back to its original form. The iodide ions undergo an oxidation. The electrons that return to the device from the external circuit reduce the triiodide ions back to the iodide ions. The device then repeats itself by allowing the transparent anode electrode to receive sunlight that enables the excitation of the dye-sensitized TiO_2 nanoparticles. For this process to occur, there are three main components involved as detailed below.

2.4.1.3 Photoanode

Transparent conducting oxide (TCO) glass is traditionally used for the fabrication of the photoanode electrode. The glass substrates are typically coated with indium-doped tin oxide (ITO), fluorine-doped tin oxide (FTO) and others use molybdenum-doped indium tin oxide. The commonly used mesoporous layer is titanium dioxide (TiO_2) however, other alternatives such as zinc oxide (ZnO) and tin dioxide (SnO_2) have also been scarcely used. These material are characteristic of high surface area, which enables the loading of the dye to occur effortlessly and the wide band gap, enable high absorption in the UV range. These characteristics are an effort to improve the efficiency of the DSSC device. An integral part of the photoanode electrode is the use of a dye. Shalini *et al.* report on various types of dyes (i.e. Ruthenium-complex, metal-free organic, mordant and natural dyes including quantum dot and perovskite sensitizers) that can be utilized however, they are not widely reported [84]. The Ruthenium-based (Ru-based) dyes are the most widely used and reported because they yield greater than 10% conversion efficiencies within the device.

2.4.1.4 Electrolyte

DSSC can make use of either solid, polymer or liquid-state electrolytes. The electrolytes are responsible for the stability of the device. Graphene and polyethylene oxide (PEO) have been used as solid electrolytes and they exhibit long-term stability in comparison to the liquid electrolyte however, the efficiency is still fairly low [85]. In light of this, liquid electrolytes (i.e. cobalt-based, sulfide-based, ferrocene-based and nickel-based) are the most commonly used in particular the iodide/triiodide [83, 86-88]. The redox electrolyte helps track the charge transfer of the I^-/I_3^- ions between the counter electrode and the photoanode. In addition, the rudimentary function of the electrolyte is to regenerate itself and the dye.

2.4.1.5 Counter electrode

The counter electrode (CE) is the third main component of DSSC. Traditionally, platinum (Pt) has been used as a catalyst layer in the assembly of DSSC devices. Platinum has exhibited excellent performance and stability however, it has some limitations such as being expensive thus increases the fabrication costs and it is prone to corrosion in the presence of the iodide/triiodide electrolyte. In light of this, there is a need to develop novel catalysts that can maintain high performance and stability, reduce fabrication costs and resist corrosion in the presence of the iodide/triiodide.

Very few quaternary semiconducting nanocrystals have been used as electrocatalysts in DSSCs. However, the quaternary semiconducting nanocrystals that have been reported have shown promising results [19, 89-91]. Toluene, a nonpolar solvent, is used to disperse the quaternary nanoparticles. The nanoparticles are either spin-coated, dip-coated or drop-casted onto TCO glass (Fig. 2.16) and annealed to remove any remaining solvent and improve connect on the substrate.

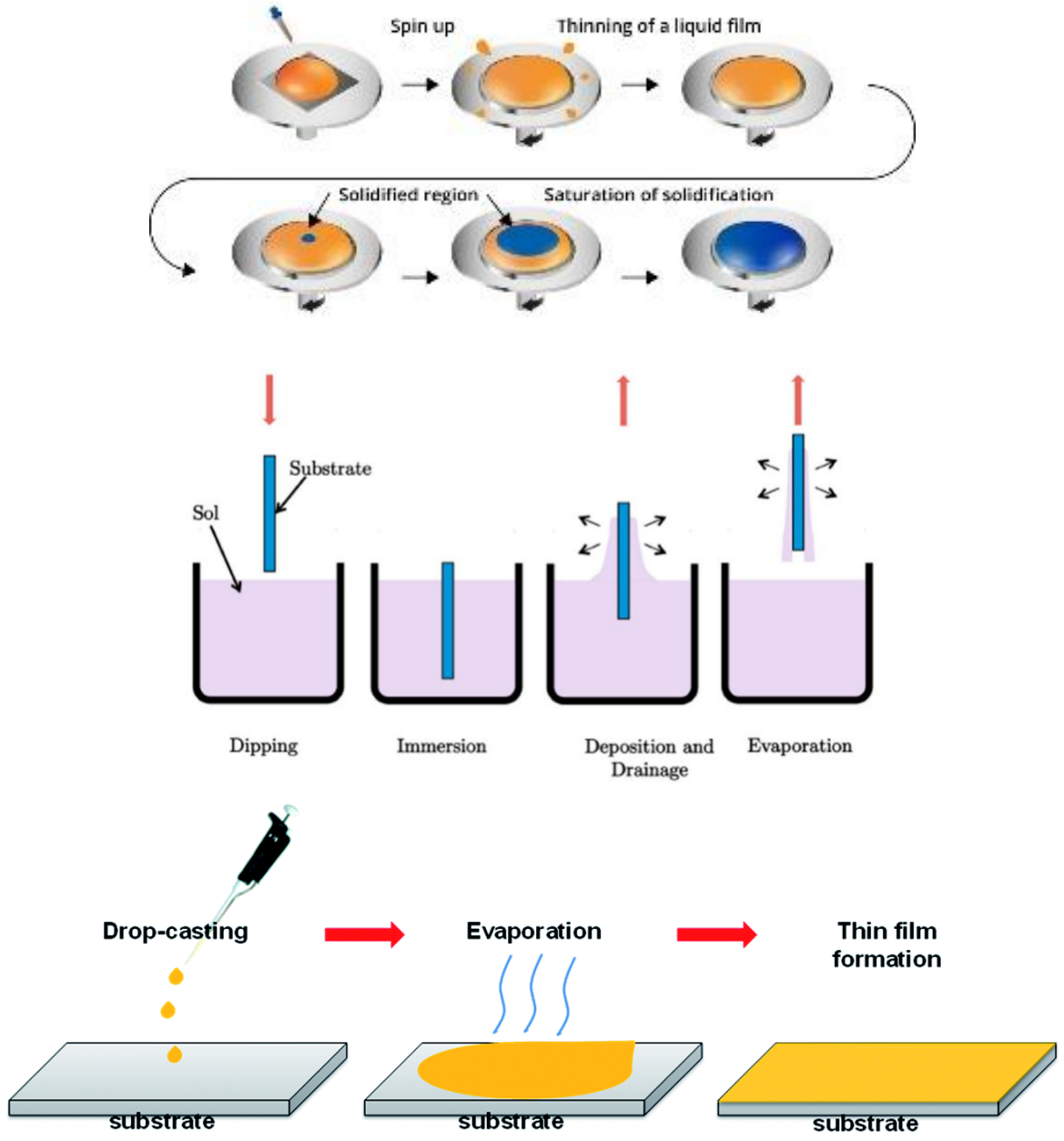

Fig. 2.16: Spin-coating, dip-coating and drop-casting techniques for depositing nano-inks onto conductive substrates [92-94].

2.5 Electrochemical Analysis

Based on either one of the deposition techniques mentioned various analytical techniques are applied to determine the electrochemical properties of the thin-film nanocrystals. In this study, the drop-casting method was applied to fabricate the CE. CEs are subjected to electrochemical measurements, where the evaluation of the electro-catalytic activity is measured firstly using a three-electrode system. The output of the three-electrode system are cyclic voltammograms (CVs) (Fig. 2.17) which illustrate the oxidation-reduction of iodide/triiodide. For the analysis of a DSSC, the oxidation-reduction of iodide/triiodide monitored. The oxidation-reduction process generally generates four peaks observed where Ox_1, Ox_2, Red_1 and Red_2 represent the following equations [95]:

$$\boldsymbol{Ox_1}: I^- \rightarrow I_3^- + 2e^- \qquad \boldsymbol{Ox_2}: I_3^- \rightarrow I_2 + 2e^- \qquad \text{(2.8) and (2.9)}$$

$$\boldsymbol{Red_1}: I_3^- + 2e^- \rightarrow I^- \qquad \boldsymbol{Red_2}: 3I_2 + 2e^- \rightarrow I_3^- \qquad \text{(2.10) and (2.11)}$$

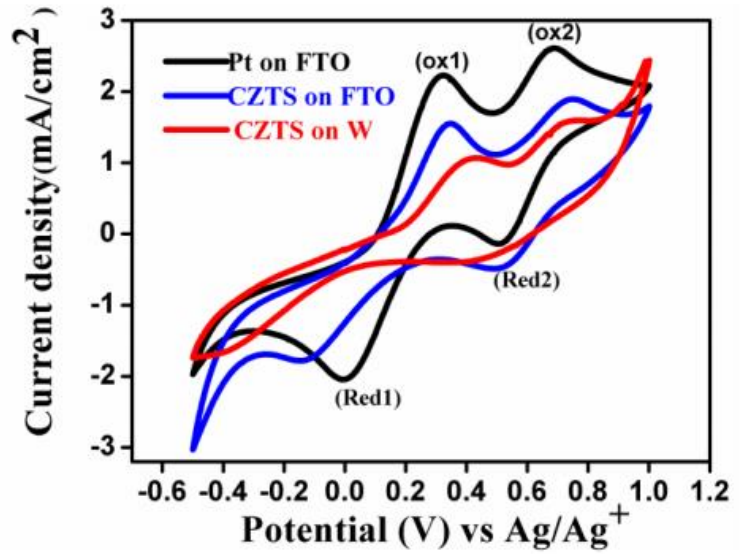

Fig. 2.17: The cyclic voltammograms of Pt, CZTS and CZTSe over a -0.6 – 1.2 potential difference [96].

The cyclic voltammogram help determine the catalytic activity of semiconducting material using the peak current (Red-1) which will be referred to in the text as $|J_{_Red\text{-}1}|$ and peak-to-peak separation (Epp). Peak current helps determine the current density value at the first reduction peak from negative to positive potential. Furthermore, peak-to-peak separation is measured

between the cathode (Red1) and anode (Ox1) potential difference as labelled in Fig. 2.17. The best performing counter electrode in a DSSC should mimic Pt and/or be better than Pt.

Part of the electrochemical analysis, is monitoring the charge transfer between the electrodes and the electrolyte. The electrochemical impedance spectroscopy (EIS) and J-V curves are suitable analytical techniques that can be further used to explore the electrochemical properties of the CEs. The Nyquist plot (Fig. 2.18(a)) is represented by Z' (real) and Z'' (imaginary) part of impedance. Notably, impedance depends on frequency and it does not rely on a constant. The characteristic shape of Nyquist plots are arcs (semi-circles) which determine the electrical properties of the symmetrical cells. A symmetrical cell is composed of two identical electrodes with cathode and anode capabilities. The semi-circle at low frequency (right side) determines the Nernst diffusion of the triiodide ions within the electrolyte. The second semi-circle at high frequency (left side) determines the charge transfer between the electrode and electrolyte interface [97]. The semicircle can also be accompanied by a straight line at an angle of 45° to the Z' axis. The line is as a result of diffusion which is created by Warburg impedance. The impedance spectra generates a circuit model equivalent which gives more information about the series/solution resistance (R_s), charge transfer resistance (R_{ct}), double layer capacitance (C_{dl}) and the Nernst diffusion (Z_w). The R_s explains the resistance of the electrolyte solution while the R_{ct} explains the impedance in its real component, where the R_{ct} value is measured based on the resistance experienced by electrons. Furthermore, the C_{dl} represents the electrical charge transfer at the metal/electrolyte interface and the Z_w measures the rate of ion diffusion.

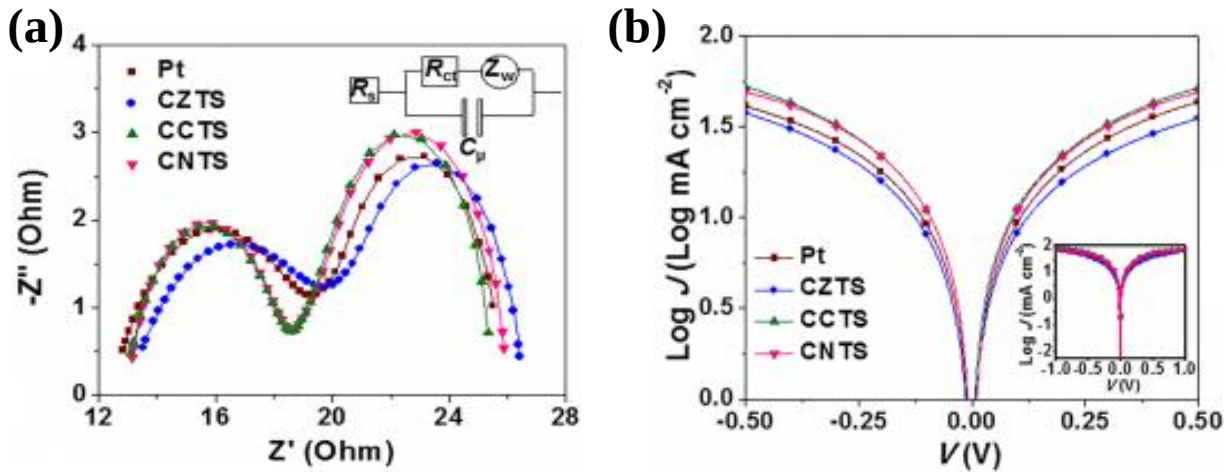

Fig. 2.18: The Nyquist (a) and Tafel polarization plots (b) of Pt, CZTS, CCTS and CNTS respectively [91].

The charge-transfer process is further characterized by Tafel polarization using the same symmetrical cells (Fig. 2.18(b)). Tafel polarization specifically studies the interfacial charge-transfer properties of the symmetrical cells. There are two significant properties obtained from Tafel plots namely, the exchange current density (J_0) and the limiting diffusion current density (J_{lim}). High J_0 and J_{lim} values, relative to the state-of-the-art Pt counter electrode indicate excellent catalytic activity [88, 97]. The calculation of the J_0 and J_{lim} values is detailed and applied experimentally in chapters 3 – 5.

2.6 Dye-sensitized solar cell performance

A solar cell is characterized by a current versus voltage measurement. The performance of a DSSC can be evaluated by using short circuit current (J_{SC}, mA.cm^{-2}), open circuit voltage (V_{OC}, V), power conversion efficiency/overall efficiency (PCE/η, %), fill factor (FF), maximum power output (P_{max}), and power input (P_{IN}) (as shown in Fig. 2.19) at a constant light level exposure.

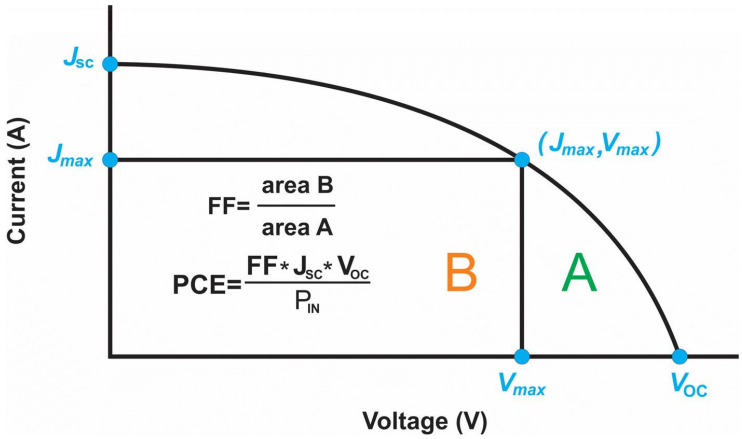

Fig. 2.19: Schematic illustrating the I/V curve for evaluating solar cell performance.

The current produces when negative and positive electrodes of the cell are short-circuited at a zero mV voltage. V_{OC} (V) is the voltage across negative and positive electrodes under open circuit condition at zero milliampere (mA) current or simply, the potential difference between the conduction band energy of semiconducting material and the redox potential of electrolyte. P_{max} is the maximum efficiency of the DSSC to convert sunlight into electricity. The ratio of maximum power output ($J_{mp} \times V_{mp}$) to the product ($V_{OC} \times J_{SC}$) gives FF as depicted in equation 2.12.

$$FF = \frac{Area\ A}{Area\ B} = \frac{J_{mp} \times V_{mp}}{J_{sc} \times V_{oc}} \qquad (2.12)$$

In addition, the overall efficiency (η) is the percentage of the solar energy (i.e. the shining of the sun on a photovoltaic cell converting it into electrical energy) where η increases with the decrease in the value of J_{SC} and an increase in the values of V_{OC}, FF, and molar coefficient of dye, respectively.

$$\eta\ (\%) = \frac{J_{sc} \times V_{oc} \times FF}{P_{in}} \qquad (2.13)$$

Once the band gap of each material has been determined, device architecture can be considered. Fig. 2.20a depicts a typical energy level diagram which illustrate the band gaps of each component and the movement of electrons within the device. In order to avoid recombination, the position of the valence band (VB) and conduction band (CB) are of uttermost importance. Yuan et al. reported that a decrease in band gap resulted in a decrease in resistivity and an improved surface photo-voltage caused by a better hole extraction due to a larger valence band offset (Fig. 2.20 (b)) [98].

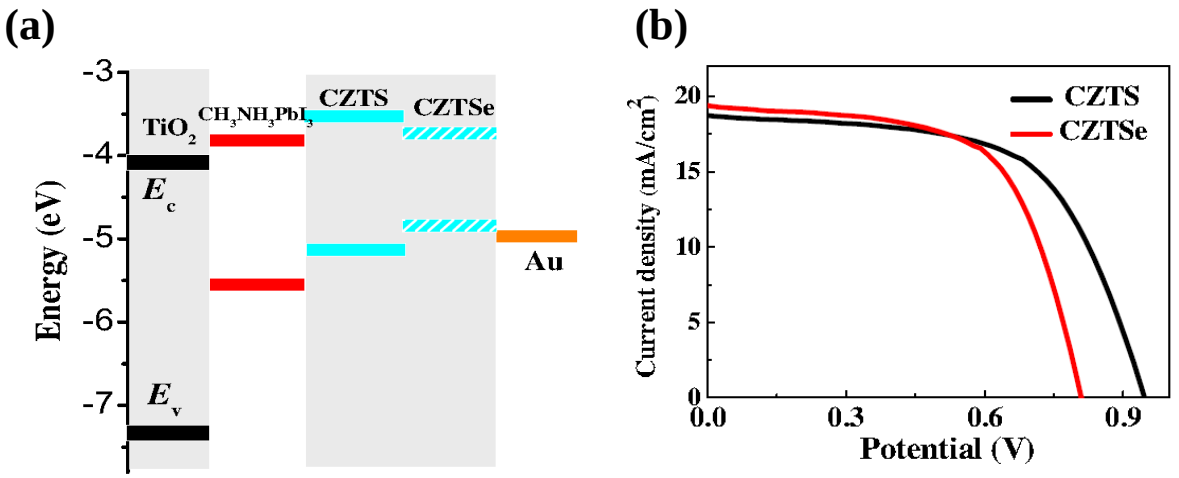

Fig. 2.20: The energy level diagram (a) and J-V curve plots (b) of CZTS and CZTSe [98].

The additional properties observed through the band tuning are the decrease in open circuit voltage (V_{oc}) and the decrease in recombination resistance which resulted in the overall decrease in efficiency of the device. Over the years, the power conversion efficiency has been

observed a steady increase from 7.4 – 7.9% for Cu_2ZnSnS_4, [88, 95], 8.0% for Cu_2FeSnS_4 [99], 8.2% for Cu_2NiSnS_4 and 8.3% for Cu_2CoSnS_4 [88] have been reported.

References

[1] V. G. Reshma, P. V. Mohanan, *Journal of Luminescence*, 205 (2019) 287-298.

[2] D. Mocatta, G. Cohen, J. Schattner, O. Millo, E. Rabani, U. Banin, *Science*, 332,**2011**, 77.

[3] J. Hu, L.-S. Li, W. Yang, L. Manna, L.-w. Wang, A.P. Alivisatos, *Science*, 292, **2001**, 2060.

[4] J. Wang, M.S. Gudiksen, X. Duan, Y. Cui, C.M. Lieber, *Science*, 293, **2001**, 1455.

[5] S. Govindraju, Synthesis and characterization of hybrid nanocomposites using polyvinylcarbazole and metal selenides to demonstrate photovoltaic properties, 2017

[6] D. Aldakov, A. Lefrancois, P. Reiss, *Journal of Materials Chemistry C*, 1 (2013) 3756-3776.

[7] S. Niki, M. Contreras, I. Repins, M. Powalla, K. Kushiya, S. Ishizuka, K. Matsubara, *Progress in Photovoltaic: Research and Applications*, 18 (2010) 453-466.

[8] J. Jean, A. Wang, V. Bulovic, *Journal of Organic Electrochemistry*, 31 (2016) 120-126.

[9] R. Nitsche, D. F. Sargent and P. Wild, *Journal of Crystal Growth*, 1 (1967) 52-53.

[10] W. Schafer, R. Nitsche, *Materials Research Bulletin*, 9 (1974) 645-654.

[11] C. Ma, H. Guo, K. Zhang, N. Yuan, J. Ding, *Materials Letters*, 186 (2017) 390-393.

[12] A. Saha, A. Figueroba, G. Konstantatos, *Chemistry of Materials*, 32 (2020) 2148-2155.

[13] J. W. Lekse, B. M. Leverett, C. H. Lake, J. A. Aitken, *Journal of Solid State Chemistry*, 181 (2008) 3217-3222.

[14] A. Lafond, C. Guillot-Deudon, J. Vidal, M. Paris, C. La, and S. Jobic, *Inorganic Chemistry*, 56 (2017) 2712-2721.

[15] J. He, Y. Guo, W. Huang, X. Zhang, J. Yao, T. Zhai, F. Huang, *Inorganic Chemistry*, 58 (2018) 9918-9924.

[16] G. Bousselmi, N. Khemiri, A. Benali, M. P. F. Graca, R. F. Santos, B. F. O. Costa, M. Kanzari, *Journal of Materials Science: Materials in Electronics*, 21 (2020) 18858-18869.

[17] L. Shi, C. Wu, J. Ding, *Journal of Alloys and Compounds*, 683 (2016) 46-50.

[18] S. Chatterjee, A. P. Pal, *Solar Energy Materials & Solar Cells*, 160 (2017) 233-240.

[19] Y. Cui, R. Deng, G. Wang, D. Pan, *Journal of Material Chemistry*, 22 (2012) 23136.

[20] M. Vishwakarmaa, D. Varandani, S.M. Shivaprasad, B.R. Mehta, *Solar Energy Materials & Solar Cells*, 174 (2018) 577-583.

[21] S. Sahayaraj, G. Brammertz, B. Vermang, T. Schnabel, E. Ahlswede, Z. Huang, S. Ranjbar, M. Meuris, J. Vleugel, J. Poortmans, *Solar Energy Materials & Solar Cells*, 171 (2017) 136-141.

[22] J. Zhang, R. Xie, W. Yang, *Chemistry of Materials*, 23 (2011) 3357-3361.

[23] S. –C. Shei, P. –Y. Lee, *IEEE Transactions on Nanotechnology*, 12 (2013) 532-538.

[24] D. Pareek, K. R. Balasubramaniam, P. Sharma, *RSC Advances*, 6 (2016) 68754-68759.

[25] A. Walsh, S. Chen, S. –H. Wei, X. –G. Gong, *Advanced Energy Materials*, 2 (2012) 400-409.

[26] C. Wang, S. Chen, J. –H. Yang, L. Lang, H. –J. Xiang, X. –G. Gong, A. Walsh, S. –H. Wei, *Chemistry of Materials*, 26 (2014) 3411-3417.

[27] A. Khare, B. Himmetoglu, M. Johnson, D. J. Norris, M. Cococcioni, E. S. Aydil, *Journal of Applied Physics*, 111(2012) 083707.

[28] B. G. Mendis, M. D. Shannon, M. C. J. Goodman, J. D. Major, R. Claridge, D. P. Halliday, K. Durose, *Progress in Photovoltaics: Research and Applications*, 22 (2014) 24-34.

[29] N. Kattan, B. Hou, D. J. Fermin, D. Cherns, *Applied Materials Today*, 1 (2015) 52-59.

[30] D. Liu, D. Han, M. Huang, Z. Zhang, T. Zhang, C. Dai, S. Chen, *Chinese Physics B*, 27 (2018) 018806.

[31] D. B. Khadka, J. Kim, *Journal of Alloys and Compounds*, 638 (2015) 103-108.

[32] C. J. Bosson, M. T. Birch, D. P. Halliday, C. C. Tang, A. K. Kleppe, P. D. Hatton, *Chemistry of Materials*, 29 (2017) 9829-9839.

[33] W. Wang, M. T. Winkler, O. Gunawan, T. Gokmen, T. K. Todorov, Y. Zhu, D. B. Mitzi, *Advanced Energy Materials*, (2013) 1301465.

[34] Q. Guo, G. M. Ford, W. –C. Yang, B. C. Walker, E. A. Stach, H. W. Hillhouse, R. Agrawal, *Journal of American Chemistry Society*, 132 (2010) 17384-17386.

[35] K. –J. Yang, D. –H. Son, S. –J. Sung, J. –H. Sim, Y. –I. Kim, S. –N. Park, D. –H. Jeon, J. Kim, D. –K. Hwang, C. –W. Jeon, D. Nam, H. Cheong, J. –K. Kang, D. –H. Kim, *Journal of Materials Chemistry A*, 4 (2016) 10151-10158.

[36] D. –H. Son, S. –H. Kim, S. –Y Kim, Y. –I. Kim, J. –H. Sim, S. –N. Park, D. –H. Jeon, D. –K. Hwang, S. –J. Sung, J. –K. Kang, K. –J. Yang, D. –H. Kim, *Journal of Materials Chemistry A*, 7 (2019) 25279-25289.

[37] A. M. Alanazi, F. Alam, A. Salhi, M. Missous, A. G. Thomas, P. O'Brien, D. J. Lewis, *RSC Advances*, 9 (2019) 24146.

[38] T. Gershon, Y. S. Lee, P. Antunez, R. Mankad, S. Singh, D. Bishop, O. Gunawan, H. Hopstaken, R. Haight, *Advanced Energy Materials*, 6 (2016) 1502568.

[39] D. Shin, T. Zhu, X. Huang, O. Gunawan, V. Blum, D. B. Mitzi, *Advanced Energy Materials*, 29 (2017) 1606945.

[40] H. Xin, S. M. Vorpahl, A. D. Collorda, I. L. Bralya, A. R. Uhla, B. W. Krueger, D. S. Ginger, H. W. Hillhousea, Physical Chemistry Chemical Physics, 17 (2015) 23859-23866.

[41] C. M. Sutter-Fella, J. A. Stuckelberger, H. Hagendorfer, F. L. Mattina, L. Kranz, S. Nishiwaki, A. R. Uhl, Y. E. Romanyuk, A. N. Tiwari, *Chemistry of Materials*, 26 (2014) 1420-1425.

[42] T. Gershon, B. Shin, N. Bojarczuk, M. Hopstaken, D. B. Mitzi, S. Guha, *Advanced Energy Materials*, (2014) 1400849.

[43] A. Cabas-Vidani, S. G. Haass, C. Andres, R. Caballero, R. Figi, C. Schreiner, J. A. Marquez, C. Hages, T. Unold, D. Bleiner, A. N. Tiwari, Y. E. Romanyuk, *Advanced Energy Materials*, 8 (2018) 1801191.

[44] Z. Wang, N. Brodusch, R. Gauvin, G. P. Demopoulos, *Nano Energy*, 53 (2018) 130-134.

[45] S. Berman, G. S. Gautam, E. A. Carter, *ACS Sustainable Chemistry & Engineering*, 7 (2019) 5792-5800.

[46] E. Chagarov, K. Sardashti, A. C. Kummel, Y. S. Lee, R. Haight, T. S. Gershon, *The Journal of Chemical Physics*, 144 (2016) 104704.

[47] N. B. M. Amiri, A. Postnikov, *Physical Review B*, 82 (2010) 205204.

[48] W. Setyawan, S. Curtarolo, *Computational Materials Science*, 49 (2010) 299-312.

[49] S. Saidi, S. Zriouel, L.B. Drissi, M. Maaroufi, *Computational Materials Science*, 152 (2018) 291-299.

[50] C. Persson, *Journal of Applied Physics*, 107 (2010) 053710.

[51] D. Pan, X. Wang, Z. H. Zhou, W. Chen, C. Xu, Y. Lu, *Chemistry of Materials*, 21 (2009) 2489-2493.

[52] J. P. Singh, M. Kumar, A. Sharma, G. Pandey, K. H. Chae, S. Lee, *Bottom-up and Top-Down approaches for MgO*, 2020.

[53] A. Kuriganova, N. Faddeev, M. Gorshenkov, D. Kuznetsov, I. Leontyev, N. Smirnova, *Processes*, 8 (2020) 947.

[54] Y. Sun, Z. Hu, J. Zhang, L. Wang, C. Wu, J. Xu, *Chemical Communications*, 52 (2016) 9821-9824.

[55] M. di Vece, *KONA Powder and Particle Journal*, 36 (2019) 72-87.

[56] Płócienni P, Guichaoua D, Zawadzka A, Korcala A, Strzelecki J, Trzaska P, B. Sahraoui, *Optical and Quantum Electronics*, 48(2016) 277.

[57] S. Kumar, P. Bhushan, S. Bhattacharya, *Springer*, (2018) 167-198.

[58] K. H. Lee, H. J. Jung, J. H. Lee, K. Kim, B. Lee, D. Nam, C. M. Kim, M. –H. Jung, N. H. Hur, *Solid State Sciences*, 79 (2018) 38-47.

[59] P. Balaz, M. Balaz, M. J. Sayagues, A. Eliyas, N. G. Kostova, M. Kanuchova, E. Dutkova, A. Zorkovska, *Crystals*, 7 (2017) 367.

[60] H. Zhou, W. –C. Hsu, H. –S. Duan, B. Bob, W. Yang, T. –B. Song, C. –J Hsu, Y. Yang, *Energy Environmental. Science*, 6 (2013) 2822-2838.

[61] J. Polte, *Crystal Engineering Communication*, 17 (2015) 6809-6830.

[62] R. Becker, W. Doring, *Annalen der Physik*, 24 (1935) 719-752.

[63] N. T. K. Thanh, N. Maclean, S. Mahiddine, *ACS Chemical. Review*, 114 (2014) 7610-7630.

[64] V. K. LaMer, R. H. Dinegar, *Journal of the American Chemical Society*, 72 (1950) 4847-4854.

[65] S. Arshadi, J. Moghaddam, M. Eskandarian, *Korean Journal of Chemical Engineering*, 31 (2014) 2020-2026.

[66] K. Qi, Y. Wang, R. Wang, D. Wu, G. –D. Li, *Journal of Material Chemistry C*, 4 (2016) 1895.

[67] M. Ibanez, R. Zamani, W. Li, A. Shavel, J. Arbiol, J. R. Morante, A. Cabot, *Crystal Growth and Design*, 12 (2012) 1085-1090.

[68] J. Zhang, R. Xie, W. Yang, *Chemistry of Materials*, 23 (2011) 3357-3361.

[69] X. Bai, F. Purcell-Milton, Y. K. Gun'ko, *Nanomaterials*, 9 (2019) 85.

[70] W. –D. Xiang, H. –L. Yang, X. –J. Liang, J. –S. Zhong, J. Wang, L. Luo, C. –P. Xie, *Journal of Materials Chemistry C*, 1 (2013) 2014.

[71] S. Mourdikoudis, L. M. Liz-Marzan, *Chemistry of Materials*, 25 (2013) 1465-1476.

[72] R. Koole, E. Groeneveld, D. Vanmaekelbergh, A. Meijerink, C. de Mello Donega, *Springer*, (2014) 13-51.

[73] T. Kolokoto, Colloidal synthesis of $NbSe_2$ nanoflowers and Nb_2Se_9 nanorods for application as counter electrode materials in dye sensitized solar cells, 2019.

[74] J. van Embden, A. S. R. Chesman, J. J. Jasieniak, *Chemistry of Materials*, 27 (2015) 2246-2285.

[75] N. Ntholeng, B. Mojela, S. Gqoba, M. Airo, S. Govindraju, M. J. Moloto, J. van Wyk, N. Moloto, *New Journal of Chemistry*, 40 (2016) 10259-10266.

[76] Q. Guo, S. J. Kim, M. Kar, W. N. Shafarman, R. W. Birkmire, E. A. Stach, R. Agrawal, H. W. Hillhouse, *Nano Letters*, 8 (2008) 2982–2987.

[77] T. –H. Yang, Y. Shi, A. Janssen, Y. Xia, *Angewandte Chemie International Edition*, 59 (2020) 15378-15401.

[78] N. Moloto, N. Revaprasadu, P.L. Musetha, M.J. Moloto, *Journal of Nanoscience and Nanotechnology*, 9 (2009) 4760-4766.

[79] R. Javed, M. Zia, S. Naz, S. O. Aisida, N. ul Ain, Q. Ao, *Journal of Nanobiotechnology*, 18 (2020) 172.

[80] H. Heinz, C. Pramanik, O. Heinz, Y. ding, R. K. Mishra, D. Marchon, R. J. Flatt, I. Estrela-Lopis, J. Llop, S. Moya, R. F. Ziolo, *Surface Science Reports*, 72 (2017) 1-58.

[81] S. P. Madhusudanan, K. Mohanta, S. K. Batabyal, *Journal of Solid State Electrochemistry*, 23 (2019) 1307-1314.

[82] D. Wei, *International Journal of Molecular Sciences*, 11 (2010) 1103-1113.

[83] H. Iftikhar, G. G. Sonai, S. G. Hashmi, A. F. Nogueira, P. D. Lund, *Materials*, 12 (2019) 1998.

[84] S. Shalini, R. Balasundaraprabhu, T. S. Kumar, N. Prabavathy, S. Senthilarasu, S. Prasanna, *International Journal of Energy Research*, 40 (2016) 1303-1320.

[85] M. S. Akhtar, S. Kwon, F. J. Stadler, O. B. Yang, *Nanoscale*, 5 (2013) 5403-5411.

[86] J. Theerthagiri, A.R. Senthil, J. Madhavan, and T. Maiyalagan, *Chemical Electrochemistry*, 7 (2015) 928-945.

[87] L. Wang, M. Al-Mamun, P. Liu, Y. Wang, H. G. Yang, H. F. Wang and H. Zhao, *NPG Asia Materials*, 7 (2015) 1-15.

[88] C-A. Tseng, C-P. Lee, *Physics*, 2 (2020) 412-424.

[89] J. –Y. Park, J. H. Noh, T. N. Mandal, S. H. Im, Y. Jun, S Seok, *RSC Advances*, 3 (2013) 24918.

[90] K. Mokurala, P. Bhargava, S. Mallick, *Solid State Physics*, 1591 (2014) 1488-1490.

[91] S. Lu, H. Yang, F. Li, Y. Wang, S. Chen, G. Yang, Y. Liu, X. Zhang, *Scientific Reports*, 8 (2018) 8714.

[92] https://www.spincoating.com/en/applications/sol-gel-process-spin-coater/208 [accessed: 02 December 2020].

[93] M. Aymerich, A. I. Gómez-Varela, E. Álvarez, M. T. Flores-Arias, *Materials*, 9 (2016) 728.

[94] X. Wu, C. Y. Toe, C. Su, Y. H. Ng, R. Amal, J. Scott, *Journal of Material Chemistry A*, 8 (2020) 15302-15318.

[95] K. Mokurala, A. Kamble, C. Bathina, P. Bhargava, S. Mallick, *Materials Today: Proceedings*, 3 (2016) 1778-1784.

[96] C. Bathina, K. Mokurala, P. Ravindran, P. Bhargava, S. Mallick, *Advanced Material Letters*, 7 (2016) 861-865.

[97] F. Yang, X. Tian, K. Zhang, X. Zhang, L. Liu, *ECS Journal of Solid State Science and Technology*, 7 (2018) P311-P316.

[98] M. Yuan, X. Zhang, J. Kong, W. Zhou, Z. Zhou, Q. Tian, Y. Meng, S. Wu, D. Kou, *Electrochimica Acta*, 215 (2016) 374-379.
[99] R. R. Prabhakar, N. H. Loc, M. H. Kumar, P. P. Boix, S. Juan, R. A. John, S. K. Batabyal, L. H. Wong, *ACS Applied Material Interface*s, 6 (2014) 17661-17667.

CHAPTER 3

Evaluating the effect of the substrate on the electrocatalytic performance of Cu_2ZnSnS_4 and $Cu_2ZnSnSe_4$ counter electrodes in dye-sensitized solar cells

3.1. Introduction

Although Pt has shown great electrocatalytic properties, its low abundance and elevated costs have impeded large-scale application. Moreover, the use of Pt as a counter electrode (CE) in a dye-sensitized solar cell (DSSC) has come under much scrutiny due to its stability or lack thereof in the triiodide/iodide electrolyte [1]. To circumvent this, research has been stimulated into finding alternative electrocatalysts that are free of noble or scarce metals, have surpassed the power conversion efficiency of crystalline-silicon/quaternary nanoparticles and are stable over harsh conditions.

Cu_2ZnSnS_4 (CZTS) and $Cu_2ZnSnSe_4$ (CZTSe) have not only emerged as attractive absorber materials in thin-film solar cells but also as candidates for CEs in DSSCs [2, 3]. CZTS and CZTSe are quaternary metal chalcogenides with desirable properties. They each have a direct bandgap within the range of 1.0 – 1.5 eV as well as a high absorption coefficient ($> 10^4$ cm^{-1}) [4, 5]. CZTS and CZTSe have been synthesized via a large number of methods but primarily as thin-films. Colloidal synthesis of CZTS and CZTSe however provides many advantages such as mild reaction conditions, easy manipulation of reaction parameters thereby resulting in tunable properties, the possibility of large-scale synthesis as well as the processability of the resultant nanoparticles [6, 7]. The processability allows for the fabrication of solution-based photovoltaics which can potentially lower the overall cost of photovoltaics.

Several studies report on the use of CZTS and CZTSe as CEs in DSSCs. Chen *et al.* reported on the in-situ hydrothermal syntheses of CZTS nanoparticles deposited on fluorine doped tin oxide (FTO) substrate for use as a CEs in DSSCs. The resultant solar cells had efficiencies ranging from 3.15% to 5.65% [8]. Mokurala and co-workers also reported on the use of various morphologies of hydrothermally synthesized CZTS on FTO as CEs in DSSCs. There are other substrates that have been explored in DSSCs namely: plastic; ITO-PEN; FTO and ITO; FTO and Titanium (Ti)-coated [9-12].

The power conversion efficiencies (PCE) of the nanoparticles were found to range from 7.4% to 7.8% [13]. On the other hand, hydrothermally and colloidally synthesized CZTSe CEs on FTO were found to have PCEs of 3.85% and 3.62%, respectively [14, 15]. Notably, in DSSCs is the use of FTO as the back and front contact. The back and front contacts play a crucial role in solar cells as they have a great influence on the efficiency and performance of the solar cell. The front and back contacts can influence the performance of a solar cell in terms of interfacial properties, charge mobility as well as the work function. High performance contacts must exhibit low resistivity, high conductivity, good chemical stability, low work functions and uniformity over the entire surface [16]. As such, herein, the use of CZTS and CZTSe as CEs in DSSCs is reported. Further comparison of the performance of the CEs deposited on three different substrates, namely vitreous carbon (VC), indium tin oxide (ITO) and FTO is conducted. VC is extremely impermeable, has exceptional strength, high resistance to corrosion, high thermal stability, and low resistivity, and has a low coefficient of thermal expansion; however, it has 60 – 80% light transmittance [17]. On the other hand, ITO and FTO are transparent conductive oxide with low resistivity; FTO is more chemically resistant than ITO [16].

3.2. Experimental section

3.2.1. Materials

Copper (I) chloride (CuCl, 97%), zinc chloride ($ZnCl_2$, 98%), stannic chloride ($SnCl_4 \cdot 5H_2O$, 97.5%), elemental sulfur (S, ≥ 99%), elemental selenium (Se, 99%), oleylamine (OLA, 70%), deuterated chloroform ($CDCl_3$, 99.8%), methanol (96%), ethanol (96%), toluene (anhydrous, 95%), hexane (anhydrous 95%), isopropanol (anhydrous, 99%), lithium perchlorate (≥ 95%), lithium iodide (99.9%), sodium iodide (anhydrous, ≥ 99.9%), lithium iodide (99.9%) iodine (≥99.8%), 4-*tert*-butylpyridine (98%) white titania paste, reflector (TiO_2, 20.0 wt%), Whatman™ glass microfiber filter paper, *N*-methyl-2-pyrrolidone (anhydrous NMP, 99.5%), vitreous carbon (surface resistivity ~ 2.5 – 3 Ω/sq), fluorine doped tin oxide coated glass slide (surface resistivity ~7 Ω/sq), indium doped tin oxide coated glass slide (surface resistivity ~ 8-12 Ω/sq) and N-719 dye (95%) were the materials used in the synthesis and analysis of quaternary chalcogenide nanoparticles. All chemicals were purchased from Sigma Aldrich, except for stannic chloride, which was purchased from Saarchem. All chemicals were used without any further purification.

3.2.2. Synthesis of the CZTS and CZTSe nanoparticles

The sequential hot-addition method was used to synthesize the nanoparticles. Oleylamine (OLA – 10 mL) was heated to 100 °C while stirring under nitrogen gas. This served as a purging process of the solvent/surfactant. At 100 °C, 1 mol CuCl was added until the solution turned yellow. This was followed by the addition of 1 mol $ZnCl_2$ where an orange colour change was observed, then 1 mol $SnCl_4 \cdot 5H_2O$ was added. The addition of $SnCl_4 \cdot 5H_2O$ caused a cloudy formation above the reaction mixture and a darker orange solution colour was observed. At this point, the reaction mixture was left to heat up to 220 °C where 1 mol elemental sulphur (S) or selenium (Se) was added to the respective reaction synthesis. The final addition changed the reaction mixture to black (CZTS) and dark grey (CZTSe). The reaction was left to run for 45 min. Thereafter, the particles were flocculated using ethanol, recovered by centrifugation at 7000 rpm and dissolved in toluene for characterization.

3.2.3. Fabrication of the dye-sensitized solar cells

Counter electrode fabrication

The ink of the counter electrodes were separately prepared by dispersing 40 mg of CZTS and CZTSe nanoparticles in a mixture of 1 mL toluene and 0.1 mL NMP. After 24 h of vigorous stirring, the homogenous solutions were sonicated for 10 min. This was followed by drop-casting the solutions onto pre-cleaned and pre-heated (at 80 °C) VC/ITO/FTO (area ~ 1.0 cm^2 for VC, area ~ 3.13 cm^2 for ITO and FTO) substrates. Once the ink was dry, each counter electrode was annealed at 80 °C for a further 10 min. Platinum was sputter-coated onto pre-cleaned VC/ITO/FTO as a reference, for comparative studies.

Photo-anode fabrication

Titania (TiO_2) paste was printed onto pre-cleaned VC/ITO/FTO substrates using the doctor blade method. The screen-printed substrates were then annealed at 350 °C for 30 min to remove any residual organic compounds and enable better contact between TiO_2 and the N-719 dye. The N-719 dye was then dissolved in methanol (3.0×10^{-4} M) and used to sensitize the TiO_2. A drop of the dye mixture was placed onto the annealed TiO_2 and left to dry overnight, in the dark at ambient conditions.

Device assembly

The photo-anode electrode was placed with the active layer facing up and the counter electrode facing down. The two electrodes were offset from each other and the Whatman filter paper was placed in between to define the active area and act as a sponge for the supporting redox electrolyte solution. The supporting redox electrolyte solution, which provides a negative electrochemical potential for the reduction process, was composed of 0.05 M iodine, 0.1 M lithium iodide, 0.1 M potassium iodide, 0.1 M sodium iodide and 0.5 M 4-*tert*-butylpyridine. The assembled device was held together length-wise by the fold back clips on both sides to create uniform distribution. The device architecture is shown in Fig. 10.

3.2.4. Characterization

The nanoparticles were characterized using the following techniques: UV-vis absorption measurements were conducted using a Varian Cary Eclipse (Cary 50) UV-vis spectrophotometer. The powdered samples were dispersed in toluene and placed in a 1 cm path length quartz cuvette for the spectral analysis. The X-ray diffraction (XRD) measurements were obtained using the Bruker D2 Phaser Powder X-ray diffractometer using Cu-Kα1 radiation (λ = 1.54060 Å) at 30 kV/30 mA using a glancing angle of incidence detector at an angle of 2°, for 2θ values between 10 - 90° in steps of 0.026° with a step time of 37 s and at a temperature of 25 °C. A few milligrams of the sample were placed on a zero background holder, flatten with a glass slide. The morphologies were obtained using a transmission electron microscope (TEM) FEI Tecnai T12 operated at 200 kV. The samples were dispersed in methanol and sonicated for 10 min. A drop of the suspended nanoparticles was then placed on a copper grid with a lacy carbon and left to dry at room temperature prior to analysing the sample. The Raman spectrum was obtained after a sample was placed into a quartz holder, using the Bruker Raman Senterra Spectrophotometer using the 532 nm excitation laser and at a very low laser power of 0.5 mV. X-ray photoelectron spectroscopy (XPS) analysis was conducted using a Thermo ESCAlab 250Xi spectrometer using a monochromatic Al Kα X-rays (300 W, 900 µm, and 1486.7 eV) as the excitation source. The FTIR spectra were obtained using a Bruker Tensor 27 Fourier Transform Infrared Spectrometer equipped with a diamond attenuated total reflectance crystal. Proton and carbon nuclear magnetic resonance (^{1}H and ^{13}C NMR) data were acquired on the 500 MHz Bruker AVANCE III spectrometer. Cyclic voltammetry (CV), electrochemical impedance (EIS), and Tafel polarization measurements were done using Biologic: VMP 300. A three-electrode system was used to conduct the CV measurements using the triiodide (I^{-}/I_3^{-}) redox electrolyte composed from 0.1 M $LiClO_4$, 0.01 M LiI, and 0.001 M I_2 dissolved in anhydrous acetonitrile, at a scan rate of 50 mV s^{-1}, using Pt

as the counter electrode, Ag/AgCl as the reference electrode and the synthesized CZTS/CZTSe as the working electrodes after being drop-casted on a glassy carbon electrode (GC, active area ~ 0.07 cm^2), vitreous carbon (VC, active area ~ 0.6 cm^2), platinum (Pt, active area ~ 0.05 cm^2), ITO and FTO (active area ~ 1.56 cm^2), respectively. EIS measurements were obtained using a symmetrical cell with two identical electrodes in the redox electrolyte used for DSSCs in the dark. The electrodes were analysed between 100 kHz and 100 MHz at varying open circuit potentials for each sample. The Tafel polarization analysis was conducted at a potential window of -1.0 to 1.0 V with a scan rate of 100 mVs^{-1}. The photocurrent-voltage (J-V) characteristic curves of the DSSCs were measured in ambient conditions using the HP 4141B source measure unit (SMU) under controlled illumination of 100 $mWcm^{-2}$ (AM 1.5G).

3.3. Results and discussions

3.3.1. Nanoparticle powder analysis

Following the synthesis, XRD studies were conducted to confirm the formation of CZTS and CZTSe nanoparticles. Shown in Fig. 3.1 are the XRD standard reference patterns and the patterns for the synthesized CZTS and CZTSe nanoparticles. The CZTS nanoparticles were indexed to a tetragonal kesterite crystal phase (space group I-42m, PDF: 00-026-0575) with diffraction peaks at 2θ values 28.50°, 30.59°, 33.15°, 47.49°, 56.28° and 58.82° corresponding to (112), (103), (200), (220), (312) and (224) diffraction planes, respectively. The diffraction pattern showed no signs of impurities. The broadness of the peaks was indicative of small crystallite sizes. Similarly, the CZTSe nanoparticles were indexed to a tetragonal kesterite crystal phase (space group I-42m, PDF: 00-052-0868) with (hkl) values (112), (204), (312) and (008) corresponding to 2θ values of 26.90°, 44.95°, 53.27° and 65.54°, respectively. Similarly, no impurities were detected from the CZTSe pattern and the peak widths were slightly narrower than those detected in CZTS, suggesting larger crystallite sizes. The crystallite sizes of both CZTS and CZTSe were estimated using the Scherrer equation from the most intense XRD peak [18]. The crystallite sizes were estimated to be 7 ± 0.60 nm for CZTS and 11 ± 0.84 nm for CZTSe respectively. The crystallite size indicates the successful synthesis NPs and quantum confinement within the nanoscale (i.e. 1 – 100 nm) range. The activity exhibited by the size of the NPs is anticipated to be better than the bulk CZTS and CZTSe materials respectively.

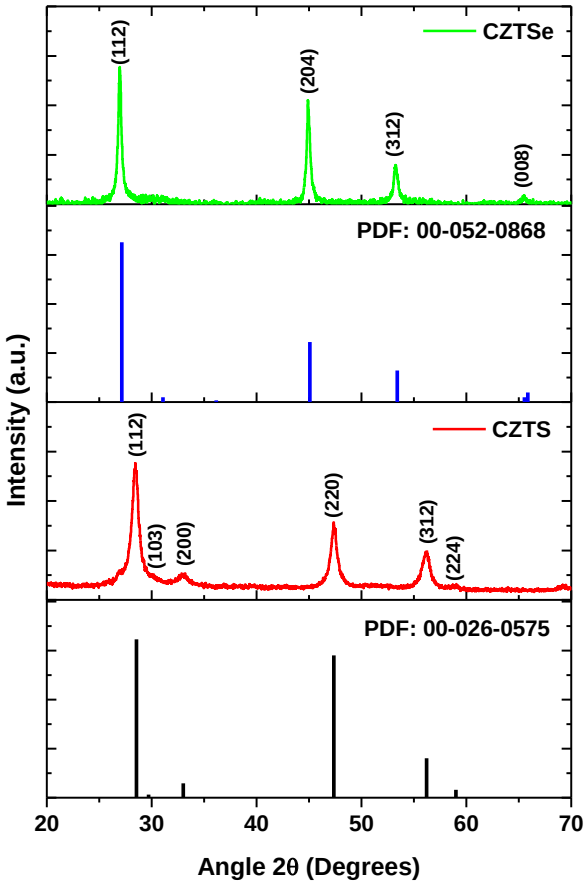

Fig. 3.1: X-ray diffraction patterns of CZTS, CZTSe and their standard reference patterns.

3.3.2: Raman analysis of CZTS and CZTSe nanoparticles

To further elucidate the structure of CZTS and CZTSe, Raman spectroscopy was conducted. The Raman spectra are shown in Fig. 3.2. The Raman spectrum of CZTS showed three peaks. Prominent peaks in the range of 287 cm^{-1} – 339 cm^{-1}, 349 cm^{-1} and 368 cm^{-1} have been shown to be consistent with the successful formation of CZTS nanoparticles [19, 20]. The 331 cm^{-1} peak is attributed to the A1 symmetry and is associated to the sulphur atom vibrations in CZTS, furthermore, it is consistent with the I-42m crystal lattice [21]. Furthermore, three peaks at 177 cm^{-1}, 188 cm^{-1} and 231 cm^{-1} were detected for CZTSe as shown in the Raman spectrum. The three peaks are attributed to the A-symmetry mode [22]. The peaks are consistent with the formation of CZTSe nanoparticles [22]. The weak peaks that are observed at ~138 cm^{-1}, 150cm^{-1}, 213 cm^{-1} for CZTSe and ~275 cm^{-1} for CZTS can be attributed to B symmetry [23].

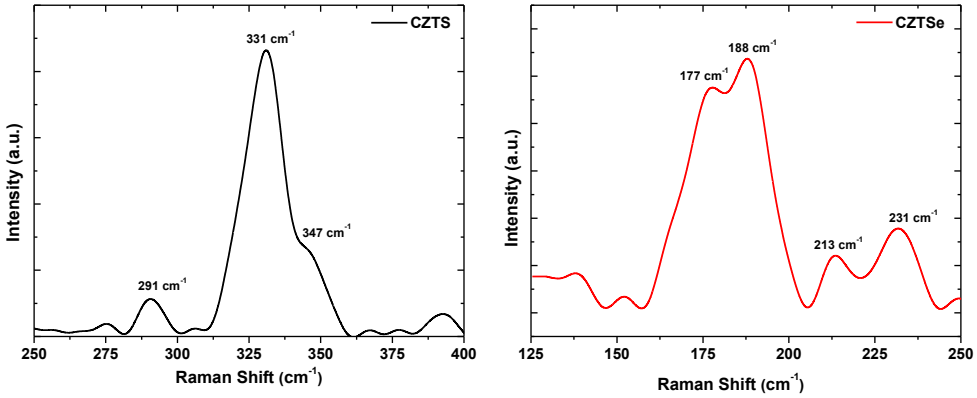

Fig. 3.2: Raman spectra of CZTS and CZTSe using a 532 nm laser.

3.3.3: XPS analysis of CZTS and CZTSe

The surface chemistry and atom bonding in the resultant NPs are evaluated by X-ray photoelectron spectroscopy (XPS). Shown in Fig. 3.3 are the XPS survey and high-resolution spectra of CZTS. The survey spectrum showed the elemental composition of CZTS as well as N 1s and C 1s associated with the capping agent OLA. The O 1s was attributed to the oxidation of the capping agent as no oxide impurities were observed in the XRD [24, 25]. The high-resolution core-level spectrum of the Cu 2p peak illustrated a doublet that is split into two peaks located at 952.3 eV and 932.6 eV. A peak separation of 19.88 eV was observed that is indicative of the presence of the Cu^{2+} species. The Zn 2p spectrum showed a doublet which was split into two peaks located at 1045.4 eV and 1022.3 eV. The peak separation was 23.03 eV and this was ascribed to the Zn^{2+} species. Furthermore, Sn 3d core-level spectrum illustrated two peaks which were deconvoluted to 495.2 eV and 486.7 eV. The peak separation of 8.45 eV was attributed to the Sn^{4+} species. The high-resolution spectrum of S 2p showed two peaks which were each deconvoluted to further two peaks. Both $2p_{3/2}$ and $2p_{1/2}$ doublets were associated with the S^{2-} species.

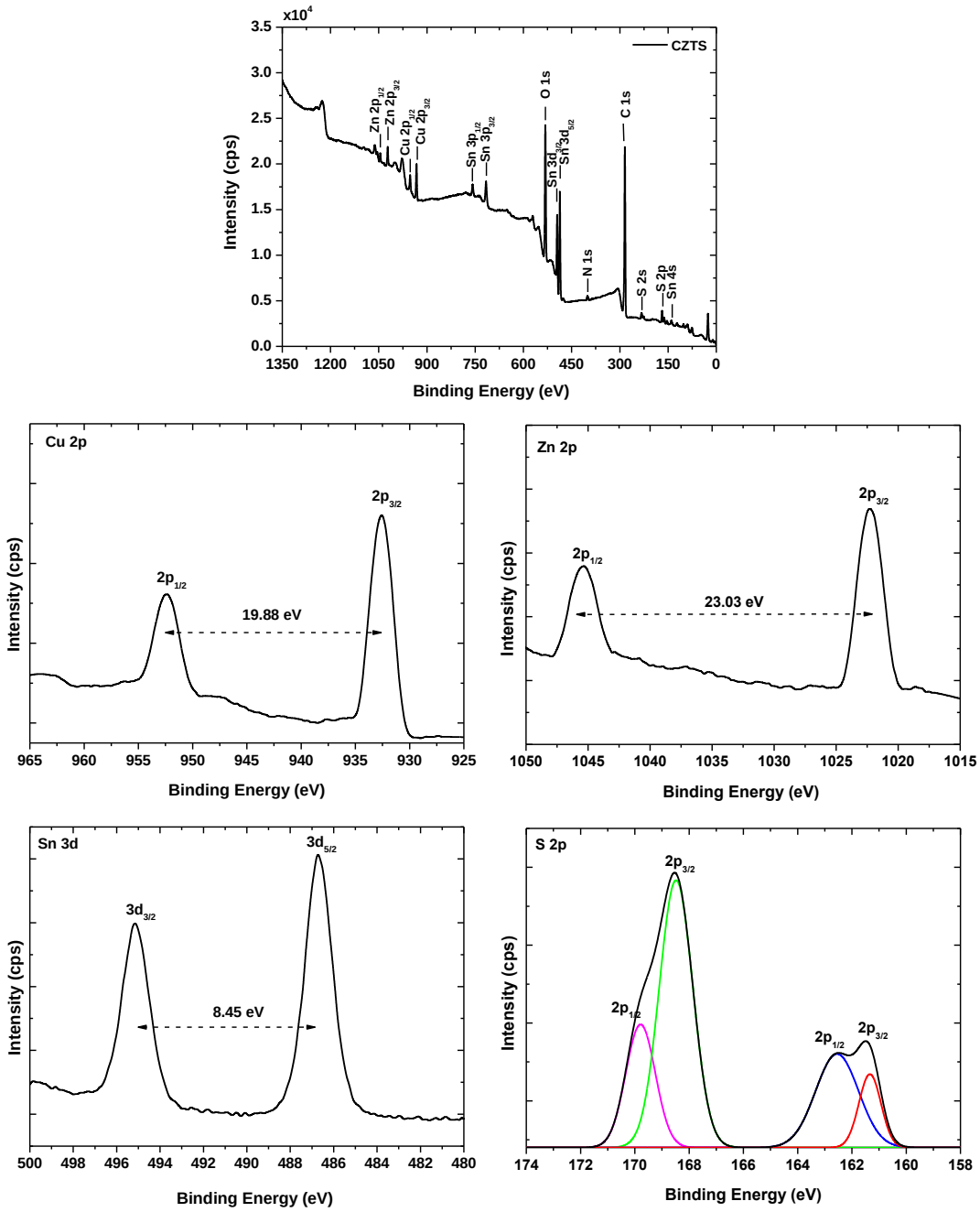

Fig. 3.3: XPS survey spectrum, Cu 2p, Zn 2p, Sn, 3d and S 2p high-resolution spectra of CZTS.

The XPS survey and core-level spectra of CZTSe are shown in Fig. 3.4. The survey spectrum is similar to that of CZTS with however selenium at low binding energies detected. The Cu 2p and Zn 2p high-resolution spectra showed the presence of Cu and Zn in a +2 state. Furthermore, the Sn 3d spectrum, illustrated two peaks which have been split to 494.8 eV and 486.3 eV. The difference in the doublet of 8.5 eV was ascribed to Sn^{4+}. Lastly, the Se 3d spectrum was

deconvulated to three peaks at 53.7 eV, 55.1 eV and 58.7 eV, respectively. The $3d_{5/2}$ and $3d_{3/2}$ peaks were associated with the Se^{2-} species while the peak at higher binding energies was attributed to SeO_x species.

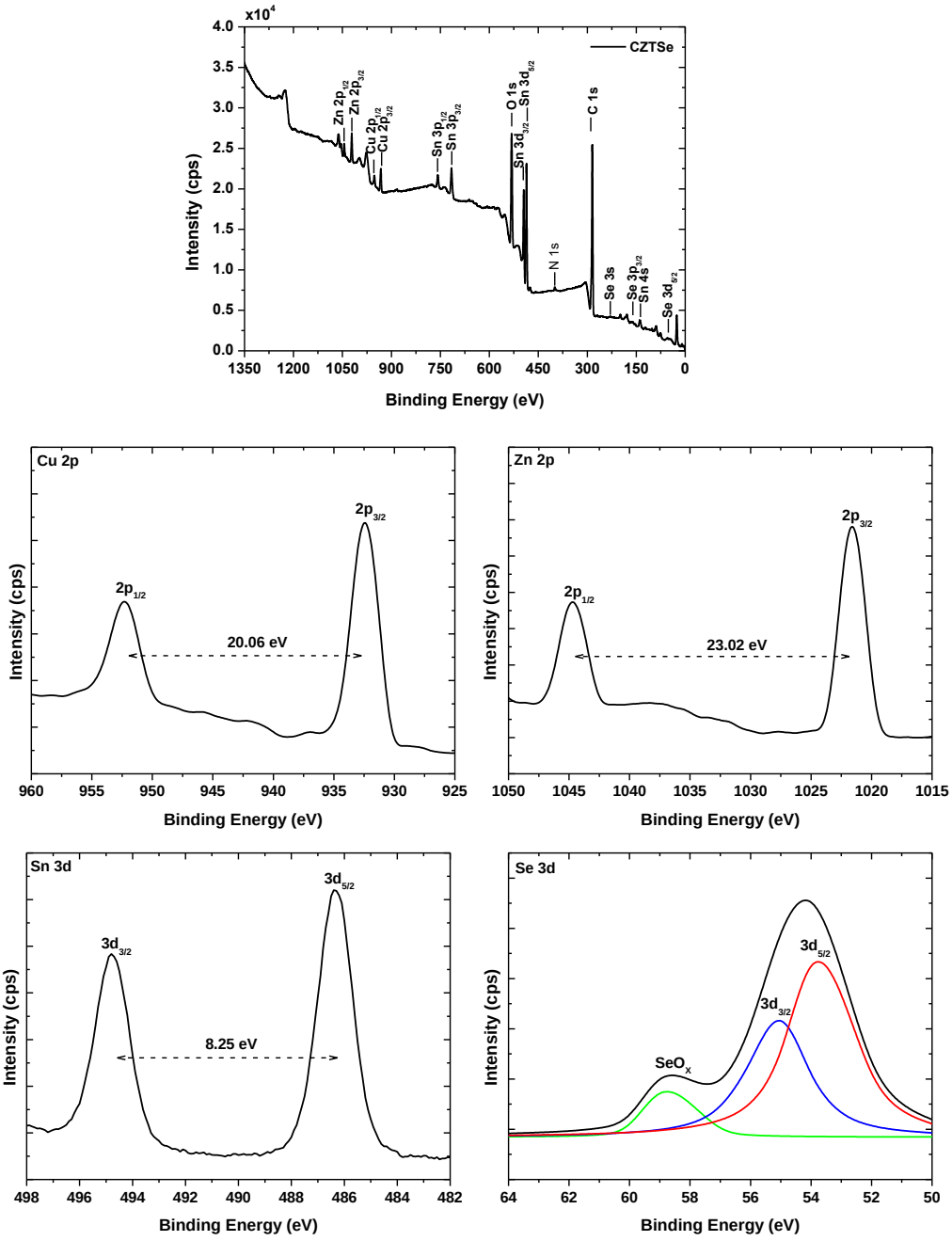

Fig. 3.4: XPS survey spectrum, Cu 2p, Zn 2p, Sn, 3d and Se 3d high-resolution spectra of CZTSe.

Apart from the constituents of CZTS and CZTSe, C, N and O were also detected. The C 1s, N 1s and O1s spectra of CZTS are shown in Fig. 3.5. The C1s illustrates the characteristic carbon

peaks namely, O – C = O; C – N/C – O and C – C peaks from the capping agent OLA. The N1s and O1s spectra also illustrate the characteristic nitrogen and oxygen peaks namely, NH_2, O – C = O, C = O and C – O respectively. Similarly, the CZTSe spectra are shown in Fig. 3.1S.

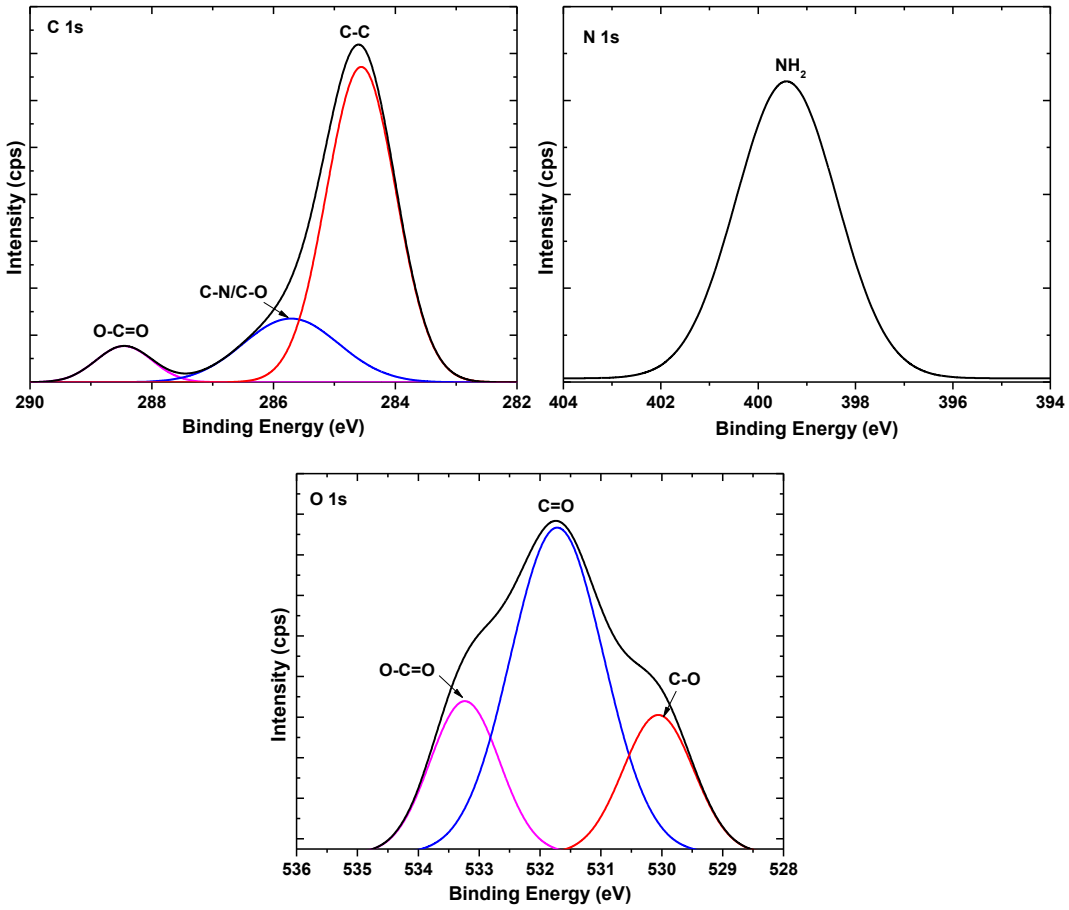

Fig. 3.5: C 1s, N 1s and O 1s high-resolution spectra for CZTS nanoparticles.

3.3.4: Surface characterisation of CZTS and CZTSe using FTIR and NMR

The C and N emanate from the OLA capping agent. Also evident from the C 1s and O 1s spectra is the surface oxidation of the capping agent. This is readily observed in XPS however usually not observed in bulk techniques such as FTIR and NMR [24]. Therefore, this strongly suggests that the oxidation is only on the surface.

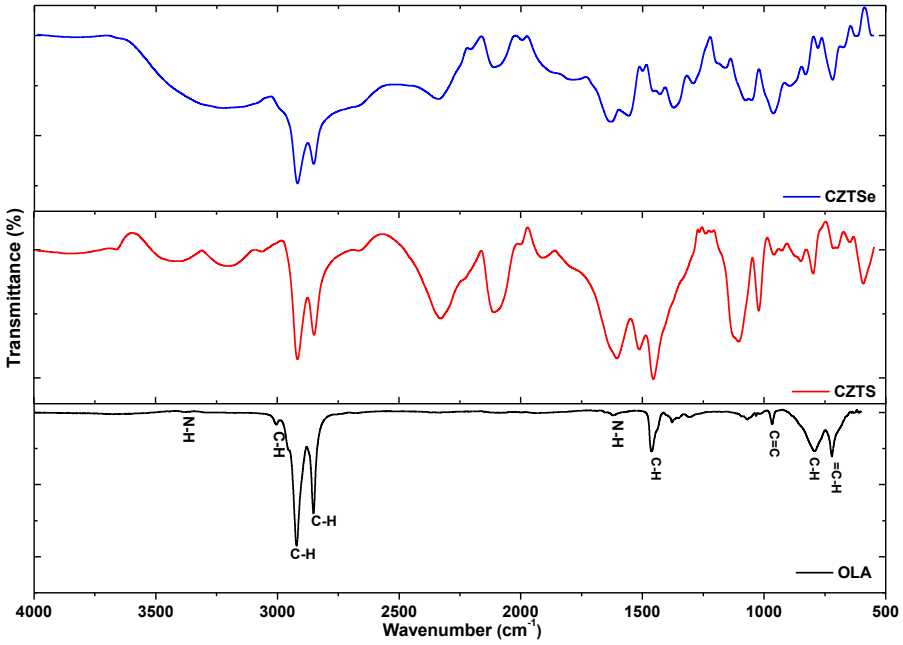

Fig. 3.6: FT-IR spectra of OLA, CZTS and CZTSe.

The nature of the capping of the nanoparticles can be further investigated using FT-IR and NMR spectroscopy. The FT-IR spectra of the as-synthesized OLA-capped CZTS and CZTSe nanoparticles are illustrated in Fig. 3.6. Three main functional groups were identified in pure OLA. These functional groups were C=C, CH_2/CH_3 and NH_2. Fig. 3.6 showed the spectra of OLA with the N-H stretch at 3376 cm^{-1}, N-H bend at 1617 cm^{-1}, C-H stretch at 3002 cm^{-1}, 2923 cm^{-1} and 2849 cm^{-1}, and the C-H bend at 1465 cm^{-1}. The intensity of the N-H bend/stretch was diminished due to the high intensity of the C-H bend/stretch. The OLA-capped CZTS and CZTSe showed the oleyl group within the 2850 – 3000 cm^{-1} region however, there was no visible peak at 3300 cm^{-1} due to the stretching of the NH_2 group observed. This suggests that OLA caps the nanoparticles through the amine hence weakening the signal. The peaks observed between the 2000 cm^{-1} and 2500 cm^{-1} region were attributed to overtones.

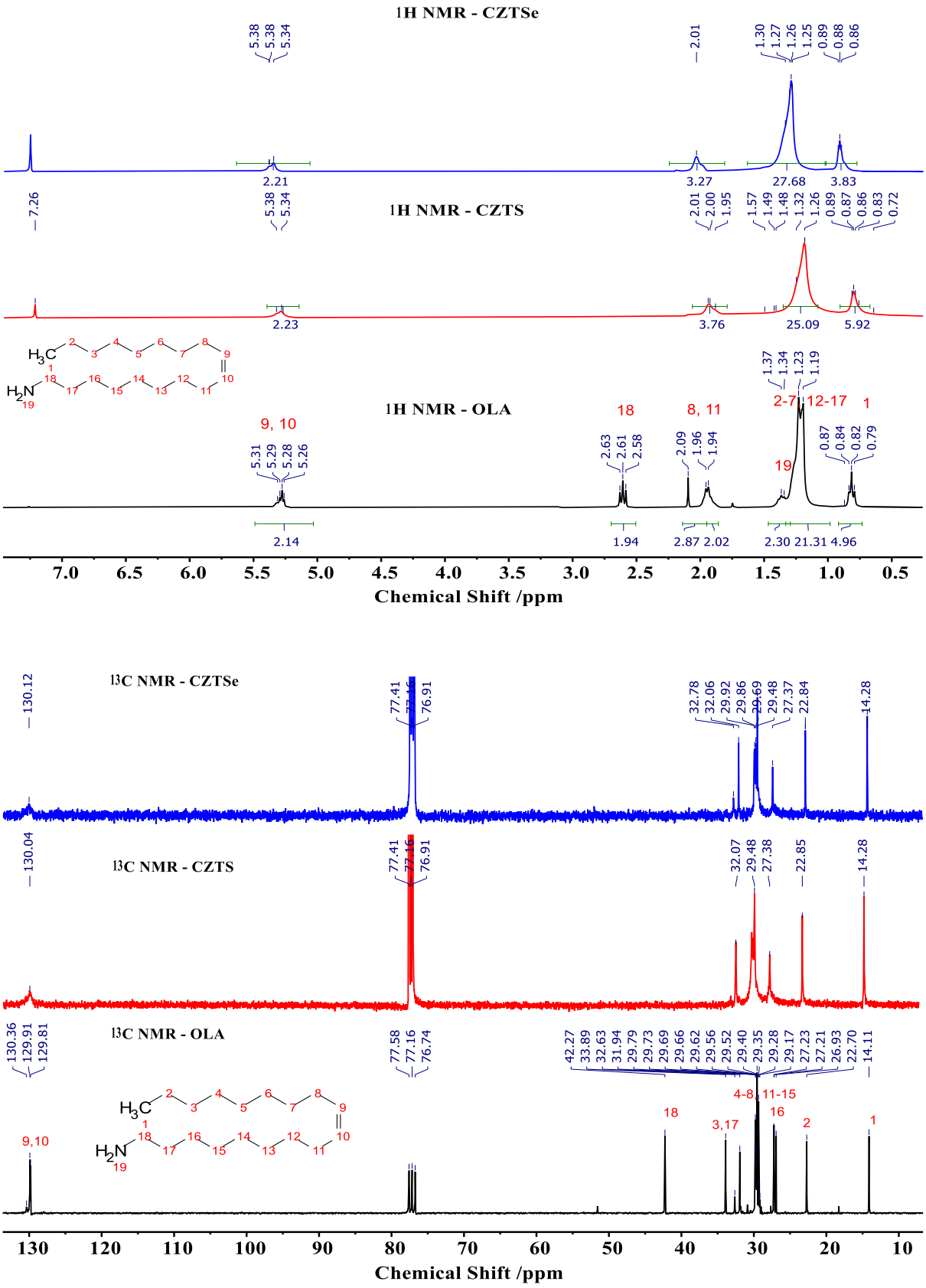

Fig. 3.7: ^{1}H NMR and ^{13}C NMR spectra of oleylamine, CZTS and CZTSe nanoparticles.

^{1}H and ^{13}C were used to further confirm the capping of the nanoparticles. Oleylamine has the molecular formula $C_{18}H_{37}N$. All the protons and carbons of OLA were accounted for in the NMR spectra (Fig. 3.7). The $–NH_2$ peak (*labelled 19*) was found in the 1.34 – 1.37 ppm region and it is a distinguishing peak in ^{1}H NMR. Similarly, the presence of the $–CH_2–NH_2$ peak (*labelled 1*) was found in the 2.58 – 2.63 ppm region in the proton spectrum. Therefore, the lack thereof in the NZTS spectrum, is indicative of the successful binding of the amine group to the surface of the NZTS. The distinguished peak in the ^{13}C spectrum is the $–CH_2–NH_2$ peak (*labelled 18*). The absence of the $–CH_2–NH_2$ peak, in the carbon spectrum of the NZTS nanoparticles, solidifies that the capping agent binds through the amine. The C – O, C = O and O – C = O peaks are not observed in the ^{13}C spectrum of the NZTS nanoparticles, suggesting that these species observed in the XPS, were only due to surface oxidation. Table 3.1 summaries the ^{1}H and ^{13}C NMR results of the pure OLA and NZTS nanoparticles.

Table 3.1: NMR assignments of OLA, CZTS and CZTSe nanoparticles.

Compound	**^{1}H NMR (δ ppm)**	**^{13}C NMR (δ ppm)**
OLA	$-CH_3-$ (0.79 – 0.87), $-CH_2-$ (1.19 – 1.23), $-NH_2$ (1.34 – 1.37), $-H_2C-HC=CH-CH_2-$ (1.94 – 2.09), $-H_2C-NH_2$ (2.58 – 2.63), -HC=CH- (5.26 – 5.31)	$-CH_3-$ (14.11), $-H_2C-CH_3$ (22.70), $-CH_2-$ (26.93 – 33.89), $-H_2C-NH_2$ (42.27), -HC=CH- (129.81 – 130.36)
CZTS	$-CH_3-$ (0.72 – 0.89), $-CH_2-$ (1.26 – 1.57), $-NH_2$ (1.95 – 2.01), -HC=CH- (5.34 – 5.38)	$-CH_3-$ (14.28), $-H_2C-CH_3$ (22.85), $-CH_2-$ (27.38 – 32.07), -HC=CH- (129.81 – 130.36)
CZTSe	$-CH_3-$ (0.86 – 0.89), $-CH_2-$ (1.25 – 1.30), $-NH_2$ (2.01), -HC=CH- (5.34 – 5.38)	$-CH_3-$ (14.28), $-H_2C-CH_3$ (22.84), $-CH_2-$ (27.37 – 32.78), -HC=CH- (130.12)

3.3.5: Morphological characterisation of CZTS and CZTSe

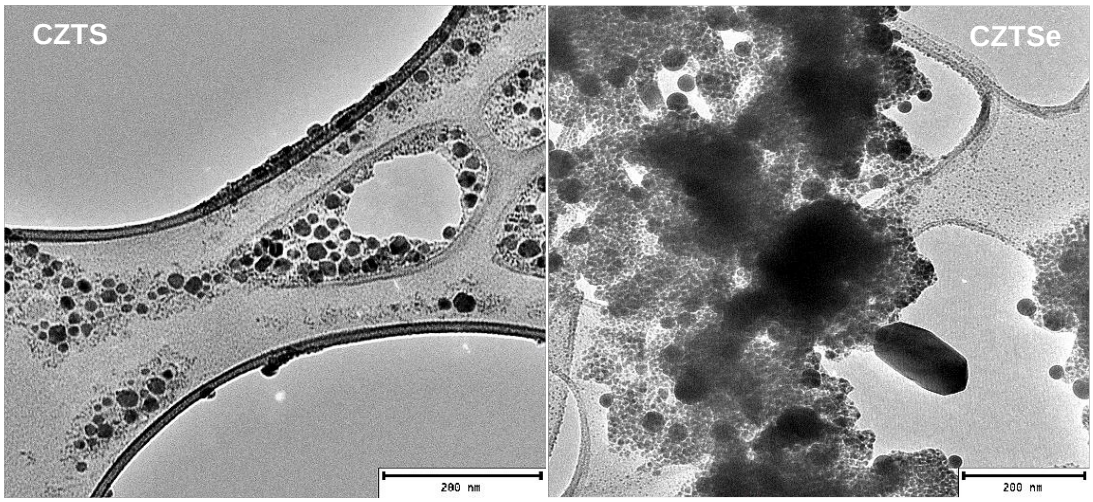

Fig. 3.8: TEM images of CZTS and CZTSe nanoparticles.

TEM analysis was conducted to determine the morphologies and sizes of the CZTS and CZTSe nanoparticles. Shown in Fig. 3.8 are the TEM images of CZTS and CZTSe nanoparticles. The CZTS particles were quasi-spherical in shape whilst the CZTSe particles were more spherical with an exception of a few elongated particles. Both particles were polydispersed and the CZTSe sample was highly agglomerated. The polydispersity and agglomeration could be advantageous in solar cell application as it improves the interconnectedness of particles thus resulting in easy charge transport [26].

3.3.6: Absorption analysis of CZTS and CZTSe nanoparticles

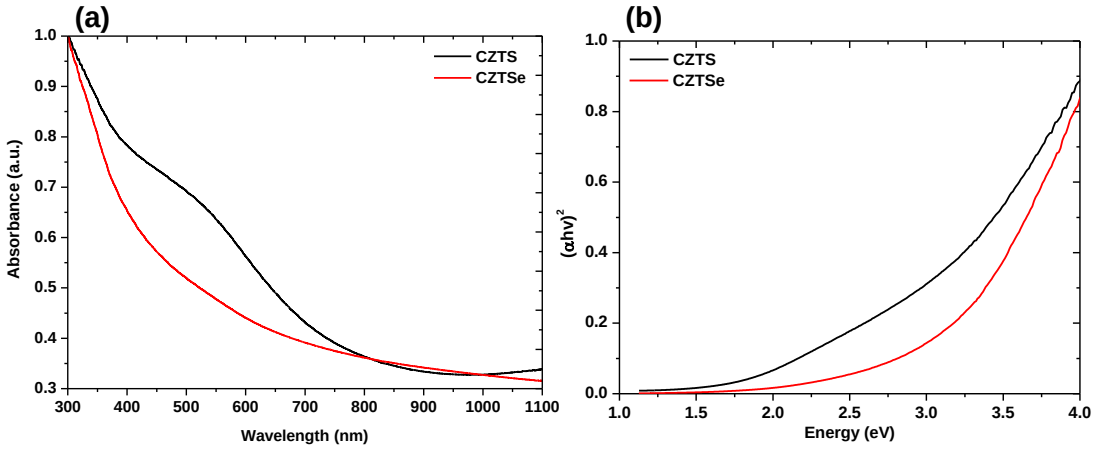

Fig. 3.9: UV-vis absorption spectra (a) and Tauc plot (b) of CZTS and CZTSe nanoparticles.

UV-vis absorption spectroscopy (Fig. 3.9) was conducted to determine the bandgap of the nanoparticles with the tauc plots illustrated in the inset. The absorption spectra of CZTS and CZTSe determined the band-gaps to be 1.3 and 1.8 eV, respectively. The band-gap energies reported for CZTS and CZTSe are in the range of 1.0 – 1.5 eV [4]. The blue-shift in the band-gap of the CZTSe nanoparticles is due to smaller particle sizes.

3.3.7. Electrochemical analysis of CZTS and CZTSe

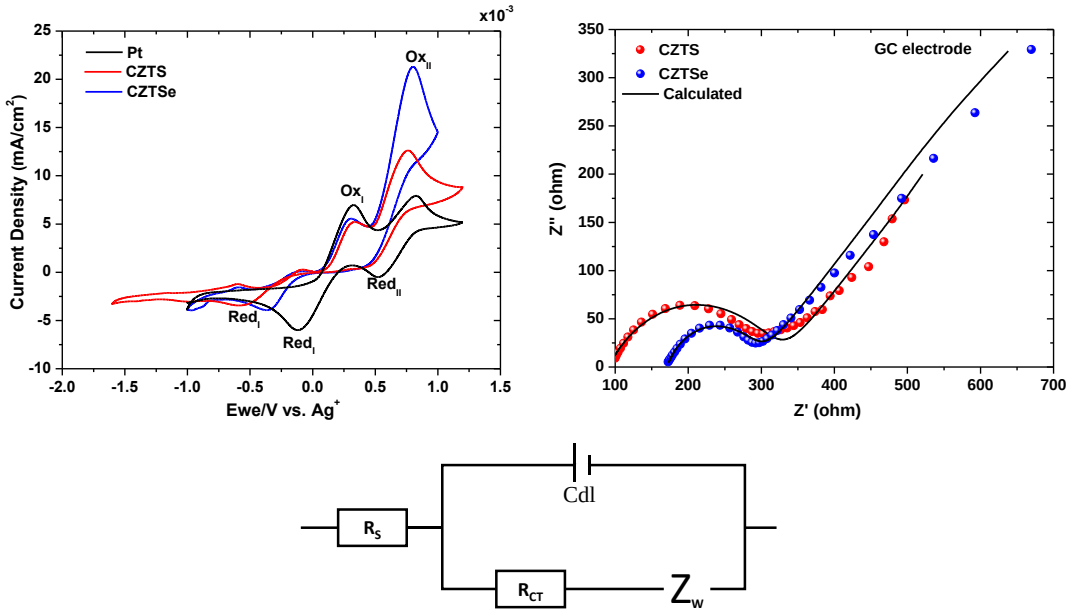

Fig. 3.10: Cyclic voltammetry of Pt, CZTS and CZTSe at a scan rate of 50 mV.s^{-1}, Nyquist plots of EIS for the symmetric cells with CZTS and CZTSe on GC and the electrochemical equivalent circuit.

The CZTS and CZTSe nanoparticles were drop-casted onto glassy carbon electrodes to investigate their electro-catalytic activities towards the reduction of the triiodide ions. The three-electrode system employed to conduct cyclic voltammetry measurements resulted in cyclic voltammograms. The CVs with the two-pairs of oxidation-reduction peaks shown in Fig. 3.10 correspond to the following equations:

$$I_3^- + 2e^- \leftrightarrow 3I^- \qquad (3.1)$$

$$3I_2 + 2e^- \leftrightarrow 3I_3^- \qquad (3.2)$$

The catalytic activity relies on two parameters namely, the peak current $|J_{_Red\text{-}1}|$ and the peak-to-peak separation (E_{pp}). Pt, CZTS and CZTSe peak current values were 6.07, 3.55, 3.93 mA.cm^{-2} and the E_{pp} values were 0.44, 0.82 and 0.67 V, respectively. The higher peak current and lower E_{pp} values for CZTSe in comparison to CZTS suggest better catalytic performance and larger reduction velocity [27]. The Red_I shift observed around the lower potential is an indication that the triiodide ions are getting difficult to reduce.

Table 3.2: CV and EIS parameters from counter electrodes drop-casted on glassy-carbon electrode

Counter electrode	E_{pp} (V)	J_{sc} (mA.cm^{-2})	R_s (ohm)	R_{ct} (ohm)
Pt wire	0.44	6.07	–	–
CZTS–GC	0.82	3.55	90.6	236
CZTSe–GC	0.67	3.93	57.5	680

The EIS was employed to evaluate the ability of the CEs to transfer charge to the electrolyte. The measurement was performed using symmetrical dummy cells with two identical electrodes enclosing the I_3^-/I^- electrolyte under non-illuminated conditions. The Nyquist plts shown in Fig. 3.11 of CZTS and CZTSe as well as the equivalent electrochemical circuit whose components depict the four impedance properties. The abbreviation, R_s signifies the series/solution resistance, while R_{ct} denotes the charge transfer resistance at the CE/electrolyte interface. Furthermore, the abbreviation C_{dl} corresponds to the double layer capacitance, which is utilized when the Nyquist plot outputs a perfect semi-circle and describes the charge storage capacity of the CEs. Lastly, Z_w signifies the Nernst diffusion element, often applied when a line found at a 45° angle to the semi-circle at the lower region designated to frequency and it explains whether diffusion-control occurs during the interaction between the CR and the electrolyte [28]. The two key parameters, R_s and R_{ct}, are summarized in Table 3.2. Notably, the CZTSe nanoparticles exhibited poor charge transfer was due to the higher R_{ct} value.

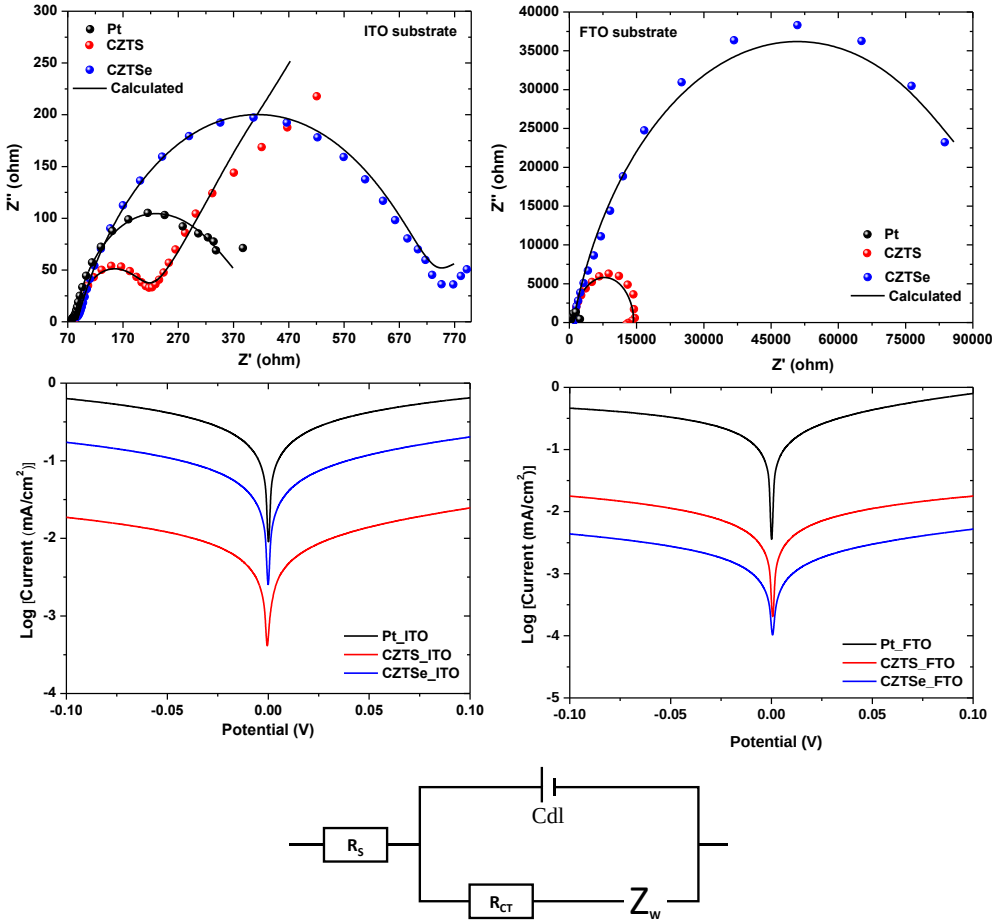

Fig. 3.11: Nyquist plots of EIS for the symmetric cells with Pt, CZTS and CZTSe on ITO and FTO substrates, Tafel plots Pt, CZTS and CZTSe electrodes on ITO and FTO substrates.

To evaluate the effect of the substrate on the electrocatalytic properties of CZTS and CZTSe, the nanoparticles were drop-casted onto ITO and FTO substrates and used in EIS and Tafel plot measurements. The same equivalent circuit model was observed for the symmetrical cell of the EIS measurements as that of the GC as shown in Fig. 3.11. The R_s and R_{ct} values for Pt, CZTS and CZTSe on both ITO and FTO are reported in Table 3.3. When using ITO as a substrate, Pt had the lowest R_s value, followed by CZTS–ITO and lastly CZTSe–ITO whilst the R_{ct} values were 282, 119 and 570 Ω for Pt–ITO, CZTS–ITO and CZTSe–ITO, respectively. The smaller the R_s value, the more conductive the material is. This suggests that Pt is most conductive followed by CZTS and lastly CZTSe. The CZTS having a lower R_s value as compared to the CZTSe is contrary to the observed trend when using glassy carbon. This suggests that the adherence of CZTS on ITO is far better than on glassy carbon. The diameter

of the semicircle on the high frequency region is due to charge transfer processes reflected on the R_{ct} values. The following trend was observed; CZTS–ITO < Pt–ITO < CZTSe–ITO. The lower value for CZTS was indicative of better charge transfer kinetics. Lower R_{ct} values are sought-after because they lead to higher J_{sc} and FF values. Changing the substrate to FTO resulted in higher R_s and R_{ct} values as compared to ITO and GC. This, therefore suggests that solar cells using FTO might perform poorer.

Table 3.3: Electrochemical performance parameters obtained from EIS & Tafel polarization plots based on CZTS and CZTSe nanoparticles on ITO and FTO substrates

Counter Electrode	R_s (ohm)	R_{ct} (ohm)	Log J_0 (mA.cm^{-2})	Log J_{lim} (mA.cm^{-2})
Pt–ITO	78.7	282	-4.34	-4.45
CZTS–ITO	84.4	119	-3.97	-10.4
CZTSe–ITO	94.6	570	-4.65	-7.30
Pt–FTO	85.5	4 789	-5.57	-5.48
CZTS–FTO	121	13 306	-6.02	-9.93
CZTSe–FTO	122	102 789	-6.90	-12.5

The Tafel polarization curves are depicted in Fig. 3.11 where the interfacial charge-transfer properties of the symmetrical dummy counter electrodes cells are studied. Two important parameters are observed from the polarization curves, namely the exchange current density (J_0) and the limiting diffusion current density (J_{lim}). Both parameters are affected by the anodic or cathodic contribution of each counter electrode and can be described using the following equation:

$$J_0 = {}^{RT}/_{nFR_{ct}} \qquad (3.3)$$

$$J_{lim} = 2nFDC/l \qquad (3.4)$$

where R represents the gas constant, T represents the temperature (298 K), F is Faraday's constant, n (n = 2) denotes the number of electrons, R_{ct} is the charge transfer resistance, D the diffusion coefficient, C is the concentration of I_3^-, and l is the spacer thickness [29]. From equation (3), J_0 is inversely proportional to R_{ct}. Therefore, J_0 can be correlated to the electrocatalytic activity of the CE. This implies that a large J_0 value has much better catalytic activity. Similarly, larger J_{lim} values indicate the larger diffusion coefficient D, which results in higher catalytic activity based on equation (4). The J_0 value of CZTS–ITO was high

symbolizing the best electrocatalytic activity. However, there is a slight discrepancy observed for the J_{lim} of CZTS–ITO when compared with that of CZTSe–ITO. The J_{lim} value was smaller and indicated the least catalytic activity. This was certainly unexpected and could be due to some form of recombination. Conversely, the J_0 and J_{lim} of the FTO substrate was in agreement with all the EIS data. This implies that CZTS–FTO displayed better charge-transfer and higher electrocatalytic activity than CZTSe–FTO.

3.3.8. Device fabrication: dye-sensitized solar cells of CZTS and CZTSe

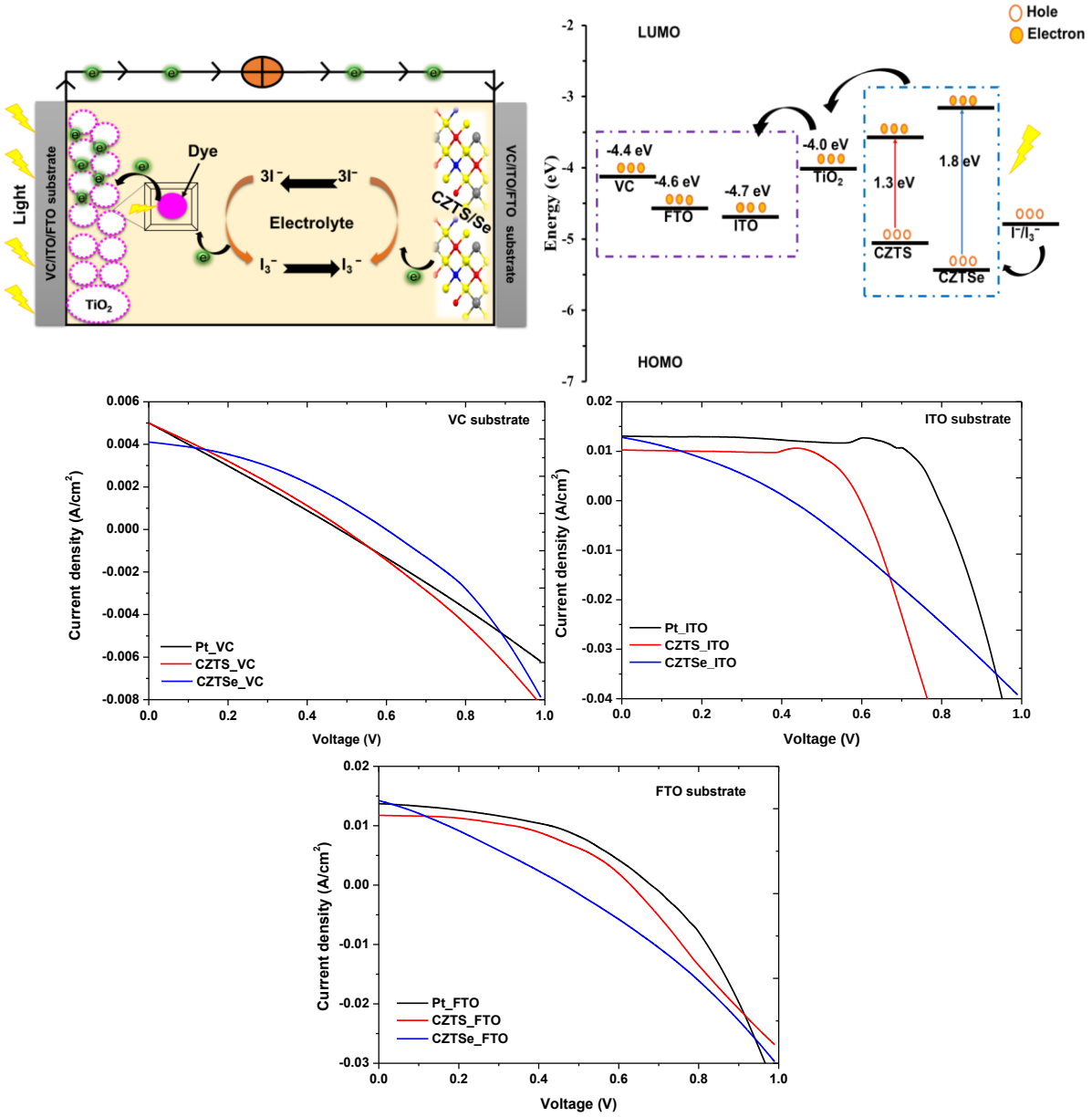

Fig. 3.12: DSSC set-up, band diagram and J-V curves of DSSCs of CZTS and CZTSe on VC, ITO and FTO substrates.

The CZTS and CZTSe nanoparticles were then used as CEs in DSSCs. Furthermore, following the CV and EIS results on glassy carbon, an additional vitreous carbon substrate was tested in conjunction with ITO and FTO. Shown in Fig. 3.12 is the solar cell architecture, band structure and the resultant current density-voltage (J-V) curves derived from the various substrates. The results are also summarized in Table 3.4. It was observed that the type of substrate used had an effect on the overall performance of the solar cell. The VC solar cells had the lowest PCEs. Even though the VC substrate has the lowest surface resistance, highest conductivity and the most stability towards chemical corrosion, it has the lowest transmittance, as such, not enough light reaches the active layer thereby hampering the performance. The ITO substrate performed better than the FTO substrate and this was consistent with the electrochemistry data. The CZTS was a better electrocatalyst than CZTSe. This could be due to the presence of SeO_x species on the surface of the CZTSe as observed in the XPS that most likely act as an insulator. Also notably from Fig. 3.12 and the data in Table 3.4 are the low FF values. The low FF values for the CZTSe CEs are due to the high R_s values and low shunt resistance (R_{sh}) values which are caused by increasing recombination at interfaces of the DSSCs [30].

Table 3.4: J-V parameters of DSSCs of Pt, CZTS and CZTSe on VC, ITO and FTO substrates

Counter Electrode	J_{sc} (mA.cm^{-2})	V_{oc} (V)	FF (%)	PCE (%)
Pt–VC	4.87	1.00	4	0.20
CZTS–VC	4.90	0.98	7	0.36
CZTSe–VC	4.12	0.99	11	0.43
Pt–ITO	13.38	0.95	52	6.57
CZTS–ITO	10.30	0.77	46	3.62
CZTSe–ITO	13.32	0.99	8	1.01
Pt–FTO	13.55	0.94	25	3.12
CZTS–FTO	11.74	0.97	18	2.07
CZTSe–FTO	13.10	0.99	6	0.79

.

3.4. Conclusions

The OLA-capped CZTS and CZTSe were successfully synthesized using the hot-addition method. Both materials crystallized in the kesterite phase with the I-42m space group. The structure was further confirmed by Raman spectroscopy. The surface chemistry of the

nanoparticles was determined using XPS, FT-IR and NMR. The XPS showed all the elemental composition of CZTS and CZTSe as well as the surface ligand (OLA) where oxidation was observed. In addition for the CZTSe nanoparticles, oxidation of selenium to SeO_x was observed. The FT-IR and NMR confirmed the capping of the nanoparticles through the amine group. The morphology of the CZTS nanoparticles was polydispersed quasi-spherical with an average size estimated from XRD of 7 ± 0.60 nm whilst CZTSe were agglomerated and polydispersed with an average size of 11 ± 0.84 nm. The obtained band-gaps for CZTS and CZTSe were 1.3 and 1.8 eV, respectively. The CZTS and CZTSe were used successfully as electrocatalysts in DSSCs. Using different substrates resulted in different PCEs. The VC substrate did not yield the desired result due to the opaque nature of the substrate which limits the transmittance of light. On the other hand, the FTO substrate exhibited low PCE, this could be due to the adhesion of the NPs to the substrate. However, this can only be confirmed by surface analysis of the thin film using SEM/AFM. In addition, the PCE values could have been affected by electron recombination observed through the low Voc values, film quality, and the reflection of the thin film. In this study, it has been reported that the type of substrate also has an impact on PCE in DSSC. Lastly, CZTS nanoparticles deposited on the ITO substrate gave the best performance with 3.62% PCE. This can be attributed to the more uniformed film quality observed visually on the substrate.

References

[1] D. Cao, X. Li, X. Yu, N. Cheng, P. Yang, B. Mi and Z. Gao, *Physica status solidi*, 217 (2019) 1-7.

[2] S. Lu, H. Yang, F. Yi, Y. Wang, S. Chen, G. Yang, Y. Liu and X. Zhang, *Scientific Report*, 8 (2018) 1-7.

[3] M.-S. Fan, J.-H. Chen, C.-T. Li, K.-W. Cheng and K.-C. Ho, *Journal of Materials Chemistry A, 3* (2015) 562-569.

[4] S. Ahn, S. Jung, J. Gwak, A. Cho, K. Shin, K. Yoon, D. Park, H. Cheong and J. H. Yun, *Applied Physics Letters*, 97 (2010) 021905-1 - 021905-3.

[5] R. Yan, L. Kang, Y. Sun and J. Zhang, *RSC Advances*, 8 (2018) 1469-11477.

[6] J. Wang, X. Xin and Z. Lin, *Nanoscale*, 3 (2011) 3040-3048.

[7] K. P. Mubiayi, D. M. G. Neto, A. Morais, H. P. Nogueira, T. Emílio de Almeida Santos, T. Mazon, N. Moloto, M. J. Moloto and J. Nei Freitas, *Materials Chemistry and Physics*, 242 (2020) 122449.

[8] S. Chen, A. Xu, J. Tao, H. Tao, Y. Shen, L. Zhu, J. Jiang, T. Wang and L. Pan, *ACS Sustainable Chemistry & Engineering*, 3 (2015) 2652-2659.

[9] H.C. Weerasinghe, F. Huang, and Y-B. Cheng, *Nano Energy*, 2 (2013) 174-189.

[10] W.T. Chiang, P.T. Lee, and R.Q. Hsu, *Manufacturing Science and Technology*, 3 (2015) 170-176.

[11] K. Sharma, V. Sharma and S.S. Sharma, *Nanoscale Research Letters*, 13 (2018) 381.

[12] A. Maharjan, *Journal Institute of Engineering*, 15(2020) 216-221.

[13] K. Mokurala, A. Kamble, C. Bathina, P. Bhargava and S. Mallick, *Materials Today: Proceedings*, 3 (2016) 1778-1784.

[14] Y.-F. Du, J.-Q. Fan, W.-H. Zhou, Z.-J. Zhou, J. Jiao and S.-X. Wu, *ACS Applied Materials Interfaces*, 4 (2012) 1796 – 1802.

[15] X. Xin, M. He, W. Han, J. Jung and Z. Lin, *Angewandte Chemie International Edition*, 50 (2011) 11739-11742.

[16] C. Platzer-Bjorkman, N. Barreau, M. Bar, L. Choubrac, L. Grenet, J. Heo, T. Kubart, A. Mittiga, Y. Sanchez, J. Scragg, S. Sinha and M. Valentini, *J. Phys Energy*, 1 (2019) 044005.

[17] S. Sharma, *Materials*,11 (2018) 1857.

[18] B. E. Warren, X-ray Diffraction 2nd Ed. (Dover, 1990).

[19] P. Fernandes, P. Salome and A. da Cunha, *Journal of Alloys and Compounds*, 509 (2011) 7600-7606.

[20] V. Kheraj, K. Patel, S. Patel and D. Shah, *Journal of Crystal Growth*, 362 (2013) 174-177.

[21] M. Dimitrievska, F. Boero, A. P. Litvinchuk, S. Delsante, G. Borzone, A. Perez-Rodriguez and V. Izquierdo-Roca, *Inorganic Chemistry*, 56 (2017) 3467-3474.
[22] R. Djemour, A. Redinger, M. Mousel, L. Gutay, X. Fontane, V. Izquierdo-Roca, A. Perez-Rodrigues and S. Siebentritt, *Optics Express*, 21 (2013) A695-A703.
[23] M. Guc, L.V. Izquierdo-Roca, X. Fontane, E. Arushanov, A. Perez-Rodriguez, *Journal of Applied Physics*, 114 (2013) 193514–1 – 193514–9.
[24] R. K. Sithole, L. F. E. Machogo, M. A. Airo, S. S. Gqoba, M. J. Moloto, P. Shumbula, J. Van Wyk and N. Moloto, *New Journal of Chemistry*, 42 (2018) 3042-3049.
[25] L. F. E. Machogo, P. Tetyana, R. Sithole, S. S. Gqoba, N. Phao, M. Airo, P. M. Shumbula, M. J. Moloto and N. Moloto, *Applied Surface Science*, 456 (2018) 973-979.
[26] H. Park, H-I. Kim, G-H Moon, W. Choi, *Energy and Environmental Science*, 9 (2016) 411-433.
[27] V. Murugadoss, J. Lin, H. Liu, X. Mai, T. Ding, Z. Guo and S. Angaiah, *Nanoscale*, 11 (2019) 17579-17589.
[428] G. Yue, W. Wu, X. Liu and H. Zheng, *Solar Energy*, 167 (2018) 137-146.
[29] X. Qian, H. Li, L. Shao, X. Jiang and L. Hou, *ACS Applied Materials & Interfaces*, 8 (2016) 29486-29495.
[30] Z. Huang, G. Natu, Z. Ji, M. He, M. Yu, and Y. Wu, *The Journal of Physical Chemistry C*, 116 (2012) 26239–26246.

CHAPTER 4

Novel colloidal synthesis of Li_2ZnSnS_4 nanoparticles and its application as counter electrodes in dye-sensitized solar cells

4.1. Introduction

The search for cheaper photovoltaics has sparked research in finding alternative materials to crystalline silicon (c-Si) as well as different solar cell configurations to maximize efficiency and reduce fabrication costs. Quaternary chalcogenide nanoparticles have been on the forefront of this endeavour. Copper-based metal chalcogenides have shown tremendous promise, with the flagship $Cu(In,Ga)Se_2$ (CIGS) solar cells achieving an efficiency greater than 24% [1]. More importantly, these solar cells employ thin film technology and as such are cheaper than c-Si to make [2]. However, the disadvantage of CIGS is the use of rather less abundant elements such as indium and gallium. To circumvent this, zinc and tin have been used as substituents to form Cu_2ZnSnS_4 (CZTS), $Cu_2ZnSnSe_4$ (CZTSe) and the mixed chalcogen $Cu_2ZnSn(S_xSe_{1-x})_4$ (CZTSSe) [3]. The Zn and Sn based solar cells unlike CIGS that employ solid-state thin film fabrication methods, use solution-based methods such as spin-coating, dip coating and drop-casting [4]. CZTS and its derivatives are part of the emerging photovoltaics. They have been used as active layers in inorganic solar cells as well as counter electrodes in dye-sensitized solar cells (DSSCs) [5, 6].

In general, a DSSC comprises a nanocrystalline titanium dioxide (TiO_2) which is modified by a Ruthenium dye, fabricated on a transparent conducting oxide (TCO) such as ITO/FTO, a Pt counter electrode (CE), and an electrolyte solution with a dissolved iodide ion/triiodide ion redox couple between the electrodes. The best DSSC has achieved an efficiency of just under 12% [7]. The modest efficiency can be balanced by further reducing the price of a DSSC; this can be achieved by replacing some of the components. Platinum is an excellent electrocatalyst, however, as well known, it is an expensive material. Several studies report on the use of CZTS and its derivatives as CEs in DSSCs. Mali *et al.* reported on the syntheses of PVP-CZTS and CA-CZTS nanofibers used as CEs in DSSCs and they showed a power conversion efficiencies (PCE) of 3.10% and 3.90%, respectively [8]. Mokurala and co-workers also reported on the use of various morphologies of hydrothermally synthesized CZTS as CEs in DSSCs. The PCE of the nanoparticles were found to range from 7.4% to 7.8% [9].

To further modify the properties of CZTS and potentially increase the efficiency in solar cells, researchers have sought out to replace the monovalent cation, divalent cation and the metal with a +4 oxidation state. The general formula for the copper chalcogenide quaternary nanoparticles is I_2-II-IV-VI_4. In this regard, Ag_2ZnSnS_4, Cu_2FeSnS_4 and Cu_2ZnGeS_4 and many other variations have been reported [9-11]. Common to all these modifications is the use of transition metals. The use of transition metals together with the substitution of the II, IV. VI elements and doping these material with alkali material has reached stagnancy with regards to the PCE (i.e. 12.3 – 12.6 %). Herein, the use of an alkali metal lithium (Li) as a replacement for the monocationic copper is proposed. Lithium has shown high conductivity in battery applications; as such, the premise is that Li_2ZnSnS_4 (LZTS) can potentially be a good candidate for solar cells. A few studies on LZTS report on the solid-state synthetic method [12, 13]. The use of solid-state methods has been successful however, this method uses extremely high temperatures in the range 500 – 2000 °C which has the potential to decompose the desired compound; the reaction times are from a couple of hours to several days and it requires an extensive amount of energy [14]. Herein, the colloidal synthesis of LZTS nanoparticles and their use as CEs in DSSCs are reported for the first time. The colloidal synthesis method applied in this study used temperatures in the range of 200 – 220 °C for less than three hours. Nanoparticles have different properties than their bulk counterparts due to quantum confinement effects. These include tunable band gap, multiple exciton generation and thermalization of excited states [15].

4.2. Experimental section

4.2.1. Materials

The chemicals used in this synthesis are the same as those used in Chapter 3 with the exception of the monovalent cation precursors. In this case, Lithium chloride (LiCl, 99.98%), lithium acetylacetonate (Li(acac), 99.95%) and lithium sulfide (Li_2S, 99.98%). All chemicals were purchased from Sigma Aldrich and used without any further purification.

4.2.2. Colloidal synthesis of LZTS nanoparticles

The hot injection colloidal method was used to synthesize the nanoparticles. Oleylamine (OLA – 10 mL) was heated to 100 °C while stirring under nitrogen gas. This served as a purging process of the solvent/surfactant. At 100 °C, the constituent precursors were added following

a set sequence tabulated in Table 4.1. After the addition of the last precursor, the temperature was raised to 220 °C and held for 45 min. The mole ratio of the precursors were varied to give a 1:1:1:1 and 2:1:0.25:2 Li:Zn:Sn:S samples across all three reactions. Then resultant particles were then flocculated using ethanol, recovered by centrifugation at 7000 rpm and dried at room temperature.

Table 4.1: Synthetic procedure of LZTS.

Reaction A	OLA $\xrightarrow[100\ °C]{}$ $ZnCl_2$ $\rightarrow$ $SnCl{\cdot}5H_2O$ $\rightarrow$ S $\xrightarrow[220\ °C]{}$ LiCl
Reaction B	OLA $\xrightarrow[100\ °C]{}$ Li(acac) $\rightarrow$ $ZnCl_2$ $\rightarrow$ $SnCl{\cdot}5H_2O$ $\xrightarrow[220\ °C]{}$ S
Reaction C	OLA $\xrightarrow[100\ °C]{}$ Li_2S $\rightarrow$ $ZnCl_2$ $\rightarrow$ $SnCl{\cdot}5H_2O$ $\xrightarrow[220\ °C]{}$ S

4.2.3. The process of the fabrication of dye-sensitized solar cells

Counter electrode fabrication

The same method used in Chapter 3 was followed. In this instance, the Li_2S 2:1:0.25:2 sample was used.

Photo-anode fabrication

The same method used in Chapter 3 was followed.

Device assembly

The same method used in Chapter 3 was followed.

4.2.4. Characterization

The same characterization techniques as in Chapter 3 were used. However, the Raman spectrum was obtained using the 785 nm excitation laser. In addition, solid-state ^{7}Li MAS NMR experiments were performed on a 11.8 T Bruker AVANCE III 500 MHz spectrometer (υ_0 = 194 MHz for ^{7}Li) using a Bruker 4.0 mm solids probe obtained using the one pulse MAS sequence at a spinning speed rate of 12 kHz.

4.3. Results and Discussions

4.3.1. Structural characterization of LZTS nanoparticles

Shown in Fig. 4.1 are the XRD patterns of LZTS synthesized using different lithium precursors and at different precursor ratios and the standard reference pattern for stannite. The LiCl and Li(acac) sources at both mole ratio configurations did not match perfectly with the reference pattern suggesting the presence of impurities such as some unreacted material and/or unknown and undesired crystal phase combinations. However as the source was changed to Li_2S, the 2:1:0.25:2 ratio matched perfectly with the reference pattern, however not all planes were diffracted suggesting preferred orientation. Because there is no reference pattern for PMCA, the calculation for the lattice constants was undertaken using equation 2.2.

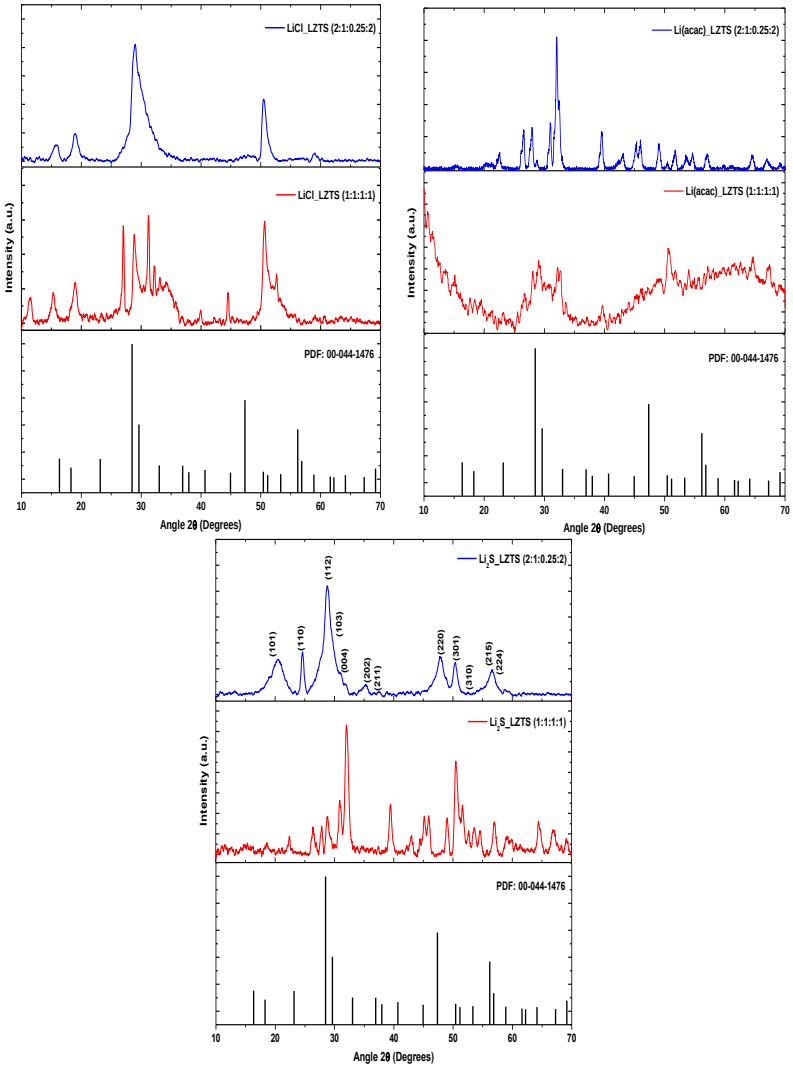

Fig. 4.1: X-ray diffraction patterns of LZTS nanoparticles synthesized using different lithium sources (LiCl, Li(acac), Li_2S) at different precursor ratios (1:1:1:1 and 2:1:0.25:2).

The LZTS (Fig. 4.2) crystallizes in similar structures as CZTS and CZTSe, the kesterite (KS, space group I4), stannite (ST, space group I42m), or primitive mixed Cu-Au (PMCA; space group P42m) crystal structures as discussed in Chapter 2 (i.e. section 2.2.5). Notably, a lengthy optimisation process was conducted to determine the best order and precursor for the synthesis of LZTS. However, only the final reaction order for each precursor is reported on and summarised in Table 4.1. The lithium chloride and lithium acetylacetonate precursors were selected based on the successful studies conducted with Cu-based quaternary material. Conversely, the lithium sulfide precursor was selected based on the solid-state synthesis of LZTS [12, 13] and it was thus incorporated in the colloidal synthesis discussed herein.

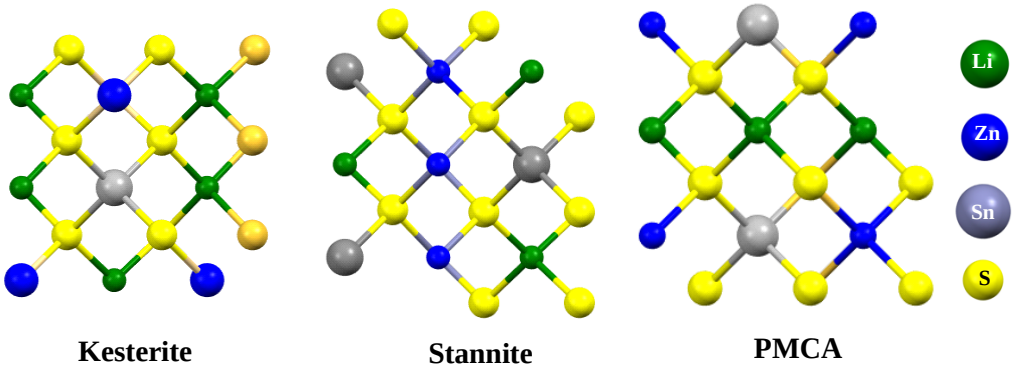

Fig. 4.2: the kesterite, stannite, and PMCA structural representations for LZTS.

The lattice constants a, b and c were determined for the Li_2S_LZTS (2:1:0.25:2) nanoparticles because that was the only sample that matched the standard reference pattern. The lattice constants were determined using the XRD experimental data and equation 2.2. The calculated experimental values are tabulated in Table 4.2 including the single crystal LZTS material, for structural comparison. The lattice constants of Li_2S_LZTS $c \approx a$ suggesting a PMCA crystal phase. The most common structure in CZTS is the kesterite phase and the stannite phase is readily observed. The possible reason for the formation of PMCA structure for LZTS is due to the difference in atomic radii of Cu (128 pm) and Li (152 pm). In addition, transition metals (Cu) are harder than alkali metals due to the number of unpaired electrons in their valence shells as such this might promote the distortion of the tetragonal structure in LZTS.

Table 4.2: Lattice parameters of tetragonal LZTS structures.

Structure	a=b (Å)	c (Å)	c/a	Ref.
Single Crystal (KS)	5.455	10.826	1.985	[16]
Li_2S_ LZTS (*exp.*)	7.222	11.199	1.551	

4.3.2. Morphological characteristics of LZTS nanoparticles

The TEM images of LZTS synthesized using different lithium sources and different mole ratios are shown in Fig. 4.3. The LiCl based nanoparticles were quasi-spherical, poly-dispersed and agglomerated. A slight increase in size was observed as the concentration was increased. The Li(acac) based nanoparticles were very small, forming agglomerated cloud-like morphologies. No visible changes were observed with the change in ratios. The Li_2S derived particles were small quasi-spherical nanoparticles, very well dispersed. A marginal increase in size was observed with the change in the ratios.

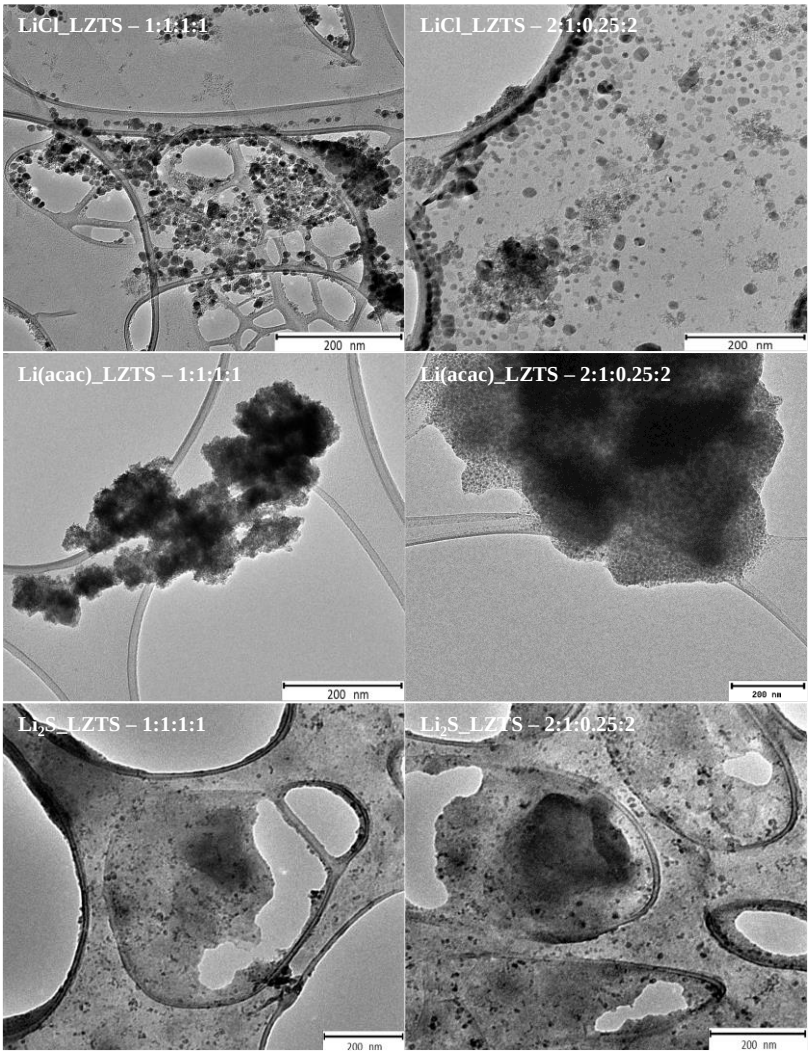

Fig. 4.3: TEM micrographs of LZTS nanoparticles synthesized using different lithium sources (LiCl, Li(acac), Li_2S) at different precursor ratios (1:1:1:1 and 2:1:0.25:2).

4.3.3. XPS analysis of LZTS nanoparticles

Similarly to Chapter 3, XPS was used. The survey spectra for the particles synthesized with different lithium sources and mole ratios are shown in Fig. 4.4. The spectra shows the same electron configurations of all present elements of the LZTS apart from lithium for the LiCl_LZTS and Li(acac)_LZTS NPs. The Li peak observed for the Li_2S NPs is also extremely small relative to the other elements. This is because XPS has very low sensitivity towards lithium, as it is a small atomic number. The C 1s, N 1s and O 1s observed in all the spectra is attributed to the capping agent OLA and its oxidation [16]. The scan survey spectra shows just a brief overview of the constituents' elements. In order to further discuss each element, the high solution spectra are explored in more detail below.

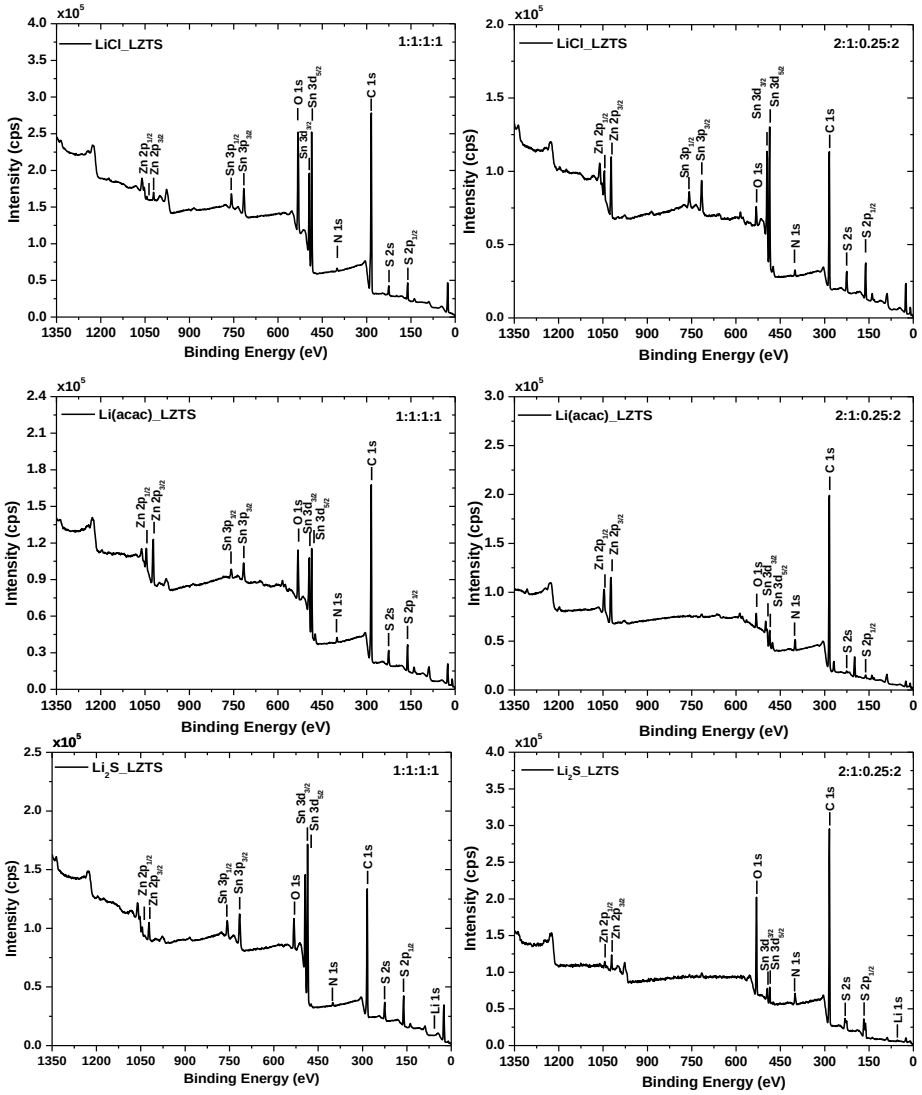

Fig. 4.4: XPS survey spectra of LZTS nanoparticles synthesized using different lithium sources (LiCl, Li(acac), Li2S) at different precursor ratios (1:1:1:1 and 2:1:0.25:2).

The Li 1s high-resolution spectra (Fig. 4.5) of the LZTS nanoparticles synthesized using different lithium precursors at different ratios. For all the samples, lithium was detected. The high-resolution spectrum is more sensitive to low concentrations as compared to the survey spectrum. Metallic lithium (Li^0) and Li-S were detected for all samples [16]. The intensity of the Li_2S derived particles (2:1:0.25:2) ratio was much high then the rest and this may be indicative of the formation of LZTS. It is worth noting that the intensity is based on difference between the origins of each peak to the highest point. This is in agreement with the observed XRD results.

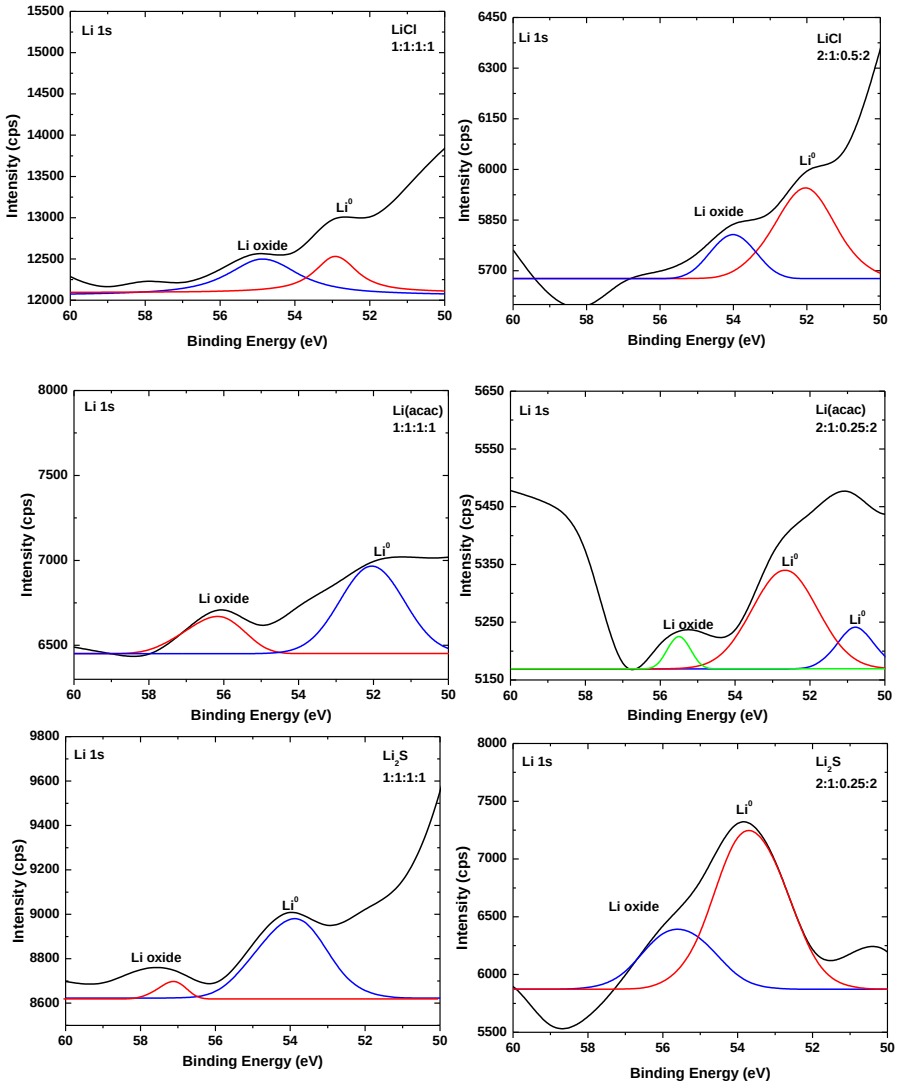

Fig. 4.5: Li 1s high-resolution spectra of LZTS nanoparticles synthesized using different lithium sources (LiCl, Li(acac), Li_2S) at different precursor ratios (1:1:1:1 and 2:1:0.25:2).

Shown in Fig. 4.6 are the Zn 2p, Sn 3d and S 2p high-resolution spectra of LZTS nanoparticles derived from the different lithium sources at 2:1:0.25:2 precursor ratios. The Zn 2p spectra for the LiCl source showed a doublet which was deconvoluted into two peaks located at 1045.4 eV and 1022.3 eV with a peak separation was 23.06 eV ascribed to the Zn^{2+} species. Furthermore, Sn 3d core-level spectrum illustrated two peaks which were deconvoluted to $3d_{3/2}$ (495.2 eV) and $3d_{5/2}$ (486.7 eV). The peak separation of 8.41 eV was attributed to the Sn^{4+} species. The high-resolution spectrum of S 2p showed two peaks which were each deconvoluted to further two peaks. Both $2p_{3/2}$ and $2p_{1/2}$ doublets were associated with the S^{2-} species. Generally, similar results were observed for Li(acac) and Li_2S derived LZTS

nanoparticles, apart from the Zn 2p spectrum of Li(acac) that showed doublets of doublets still attributed to the Zn^{2+} ions and the S 2p spectrum of Li_2S that showed a presence of SO_x species.

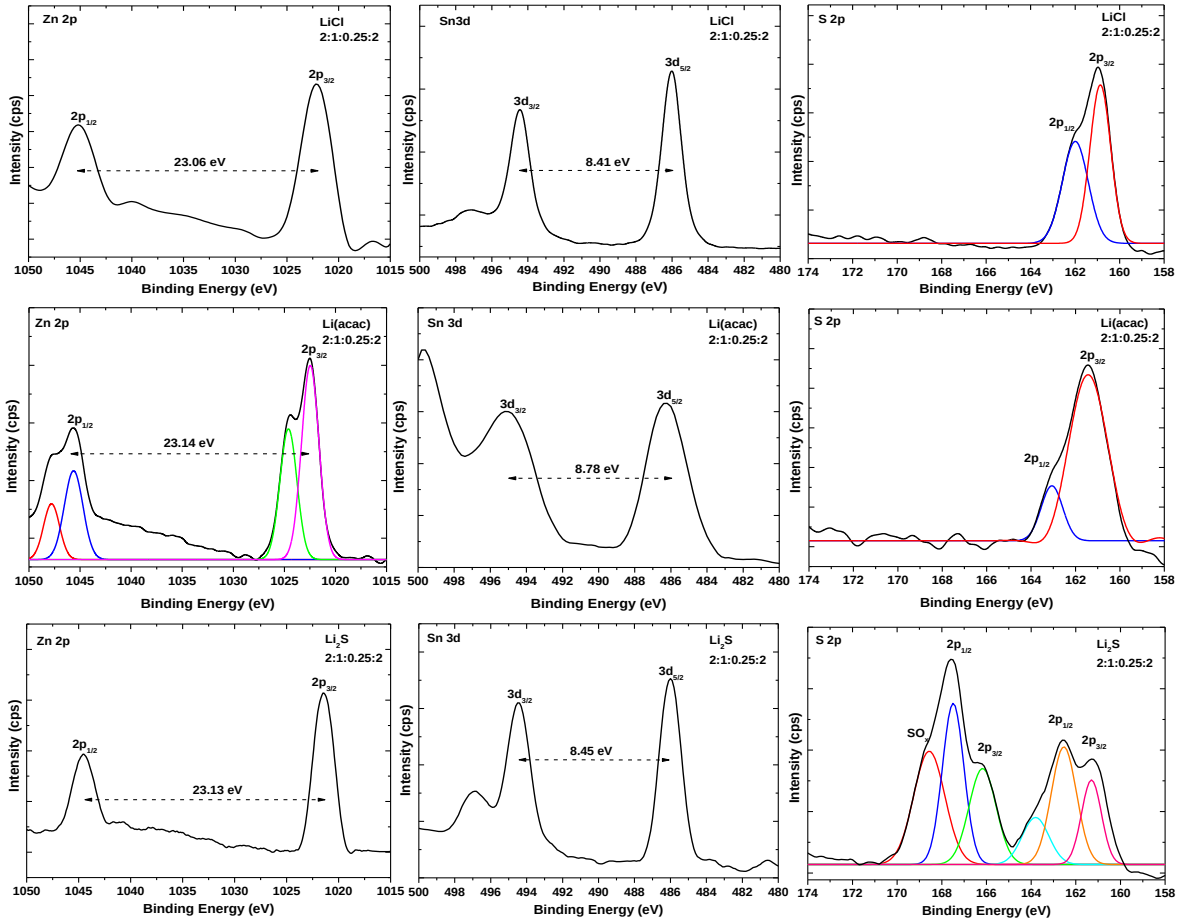

Fig. 4.6: Zn 2p, Sn 3d, S 2p high-resolution spectra of LZTS nanoparticles synthesized using different Li_2S at different precursor ratios 2:1:0.25:2.

4.3.4. NMR analysis of LZTS nanoparticles

To further confirm the formation of LZTS, ^{7}Li MAS NMR spectra of the different lithium precursors used and the corresponding LZTS nanoparticles are shown in Fig. 4.7. The signature lithium peak was observed in the commercial precursors LiCl, Li(acac) and Li_2S at 2-3 ppm [17]. The peak was also observed in the corresponding LZTS nanoparticles though slightly shifted. The shift confirming the coordination of Li. Notably the peaks observed from the SSNMR spectra indicate the local chemical environment surrounding the nucleus of interest. A single peak indicates a single local environment and two or more peaks indicate plural environments. Therefore, it is worth noting that the lithium precursors are hygroscopic in nature. Therefore, the two peaks observed for the Li_2S and Li(acac) precursors could be due to

the adsorption of moist air during the packing process of the material into the rotor. This phenomenon was not observed with LiCl due to its seemingly more stable nature.

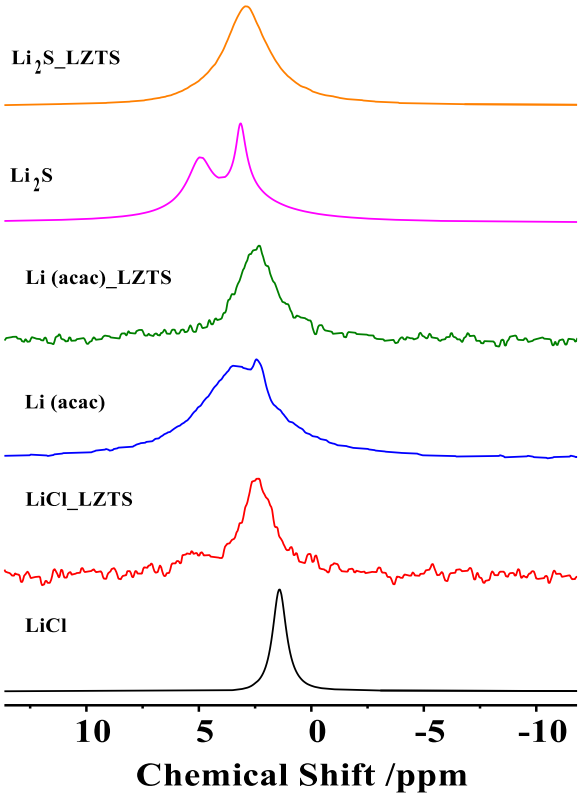

Fig. 4.7: ^{7}Li MAS NMR spectra of the LiCl, Li(acac) and Li_2S and the corresponding LZTS spectra.

4.3.5. Absorption analysis of LZTS nanoparticles

Similarly to Chapter 3, the organic ligand that caps the nanoparticles forms an integral part of the Li_2S_LZTS structure. Therefore, to identify the nature of OLA, FT-IR, XPS, and liquid state NMR (*Fig. 4.1S – Fig.4.11S*) were employed [15, 16]. The optical properties of the LZTS nanoparticles synthesized using different precursors and ratios are shown in Fig. 4.8. The band gap for 1:1:1:1 LiCl, Li(acac) and Li_2S derived particles were 2.42 eV, 2.39 eV and 3.09 eV respectively and as the ratio was changed, the band gaps were 3.13 eV, 3.23 eV and 3.14 eV, respectively. The band gap for LZTS nanoparticles derived from Li_2S did not change with the change of ratio.

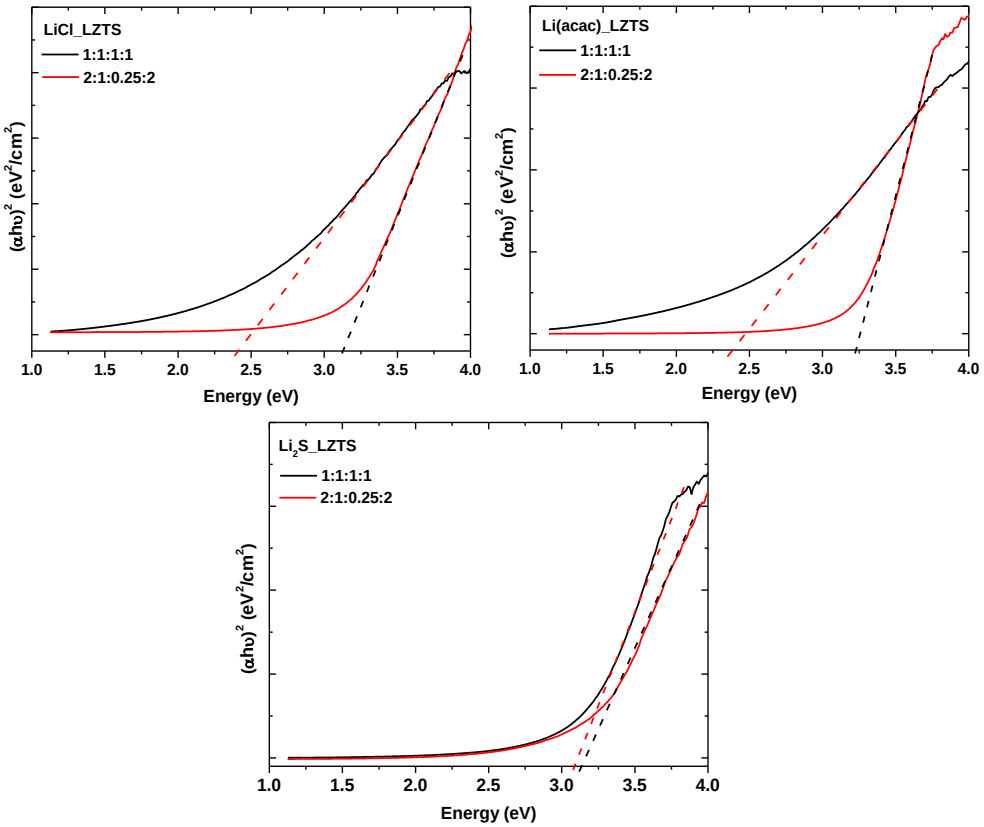

Fig. 4.8: Tauc plots derived from UV-vis absorption spectra of LZTS nanoparticles synthesized using different lithium sources (LiCl, Li(acac), Li_2S) at different precursor ratios (1:1:1:1 and 2:1:0.25:2).

4.3.5. Raman analysis of LZTS nanoparticles

Based on the XRD, TEM, XPS and the NMR results which confirmed the desired crystal phase, morphology, chemical composition and the chemical/electronic environment of the quaternary NPs for solar cell application; the best sample was evidently the LZTS nanoparticles synthesized from Li_2S using a 2:1:0.25:2 Li:Zn:Sn:S ratio (*see appendix: Fig. 4.12S for LiCl_LZTS and Li(acac)_LZTS Raman spectra)*. Henceforth, all the characterization and application were based on this sample. Shown in Fig. 4.9 is the Raman spectrum of Li_2S_LZTS. A prominent peak at 318 cm^{-1} attributed to the A_1 mode of the tetragonal PMCA structure was observed [18]. Additional peaks at ~248 cm^{-1} and ~330 cm^{-1} – 363 cm^{-1} were attributed to the B_2 and A_1 modes, respectively [19]. This further confirmed the formation of LZTS. Furthermore, the Raman analysis showed no evidence of secondary phases.

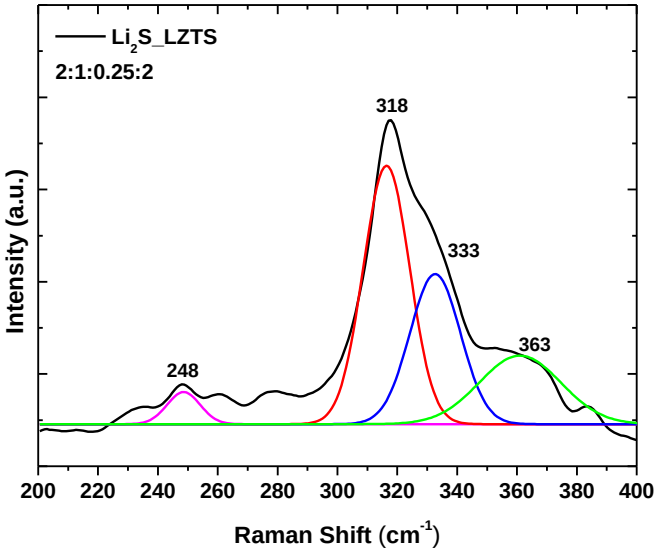

Fig. 4.9: Raman spectrum of LZTS nanoparticles synthesized using Li_2S and 2:1:0.25:2 ratio.

4.3.6. Application of LZTS as a counter electrode in dye-sensitized solar cells

The LZTS nanoparticles synthesized from Li_2S (2:1:0.25:2) were drop-casted onto a glassy carbon electrode to investigate the electro-catalytic activity towards the reduction of the triiodide ions (Fig. 4.10). Similarly to Chapter 3, the three-electrode system employed to conduct cyclic voltammetry measurements resulted in cyclic voltammograms (CVs). The Pt and LZTS peak current values were 3.53 and 3.16 $mA.cm^{-2}$ and the E_{pp} values were 0.33 and 0.61 V, respectively (Table 4.3). Similarly, to the CZTS and CZTSe CEs, the higher peak current and lower E_{pp} values suggest better catalytic performance and larger reduction velocity [20]. The Red_I shift observed around the lower potential is indicative of the poor reversibility of the reaction.

Table 4.3: CV and EIS parameters from the LZTS counter electrodes drop-casted on glassy-carbon electrode

Counter Electrode	Epp (V)	J_{sc} (mA.cm^{-2})	R_s (ohm)	R_{ct} (ohm)
Pt	0.33	3.53	–	–
LZTS – GC	0.61	3.16	81.6	451

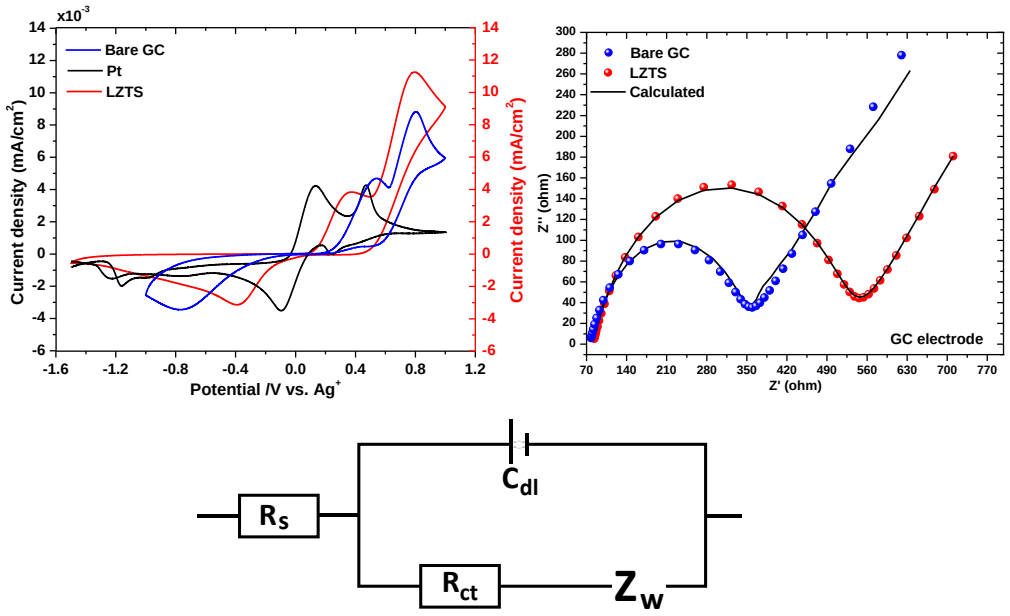

Fig. 4.10: Cyclic voltammetry of Pt and LZTS at a scan rate of 50 mV.s^{-1}, Nyquist plot of the EIS for the symmetric cell with LZTS on GC and the electrochemical equivalent circuit.

Similarly to Chapter 3, EIS measurements were performed using symmetrical dummy cells with two identical electrodes enclosing the I_3^-/I^- electrolyte under non-illuminated conditions. Fig. 4.11 shows the Nyquist plots of Pt and LZTS as well as the equivalent electrochemical circuit whose impedance components and abbreviations have been explained in Chapter 3. The two key parameters, R_s and R_{ct}, are summarized in Table 4.3. The high R_{ct} value was indicative of the poor charge transfer.

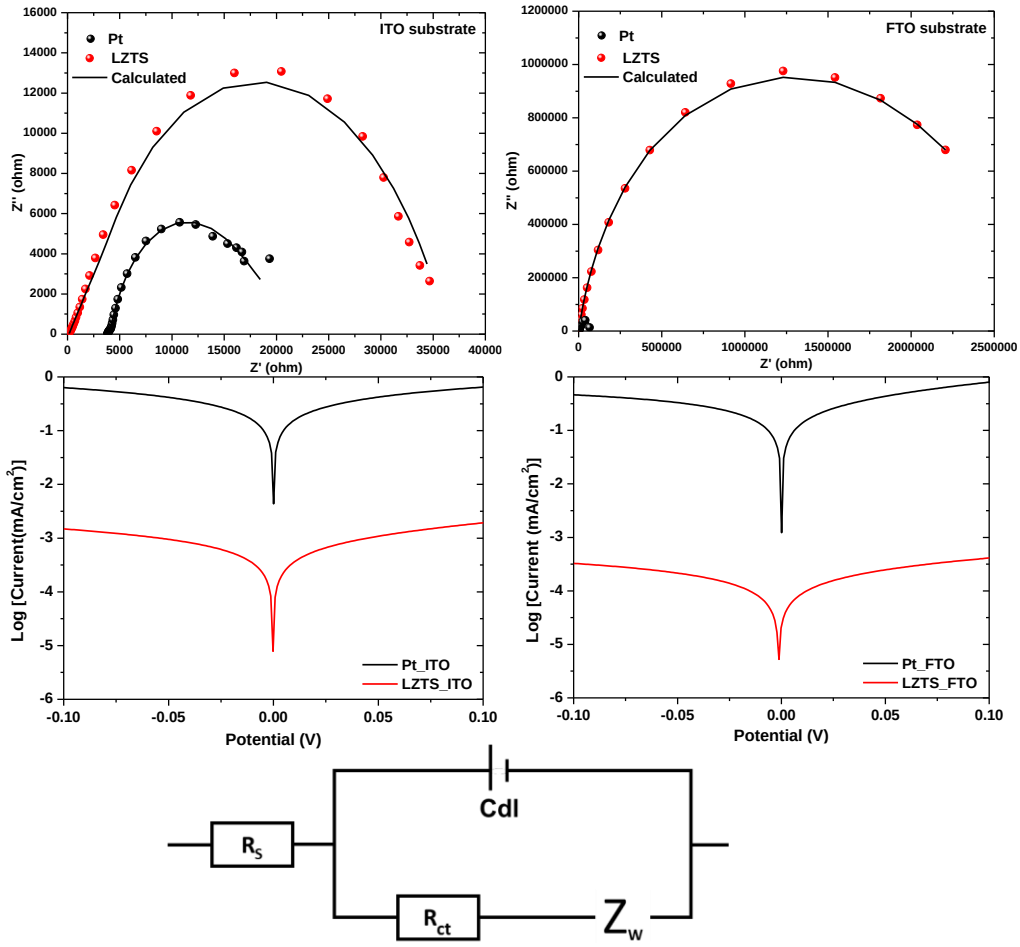

Fig. 4.11: Nyquist plots of EIS for the symmetric cells with Pt and LZTS on ITO and FTO substrates, Tafel plots of Pt and LZTS electrodes on ITO and FTO substrates.

Similarly, the effect of the substrate on the electrocatalytic properties of LZTS were investigated after the NPs were drop-casted onto ITO and FTO substrates and used in EIS and Tafel plot measurements. The same equivalent circuit model was observed for the symmetrical cell EIS measurements as that of the GC as shown in Fig. 4.11. The R_s and R_{ct} values for Pt and LZTS on both ITO and FTO are reported in Table 4.4. When using ITO as a substrate, Pt had the lowest R_s value as compared to the FTO substrate. Similarly, LZTS had a lower R_s value when the substrate was ITO. The lower R_s values for Pt for both substrates compared to LZTS suggests that Pt is more conductive. The charge transfer process represented by the diameter of the semicircle on the high frequency region reflected on the R_{ct} values. Lower R_{ct} values are sought-after because they lead to higher J_{sc} and FF values. Changing the substrate to FTO resulted in higher R_s and R_{ct} values as compared to ITO. Once again, it was observed that using FTO for solar cells might result in poor performance. The varied performance can

be due to a variety of reasons, with one possible reason being the possibility of better adhesion of the NPs to the ITO substrate as opposed to the FTO substrate. Thin-film analysis (i.e. SEM/AFM) could be done to further confirm this hypothesis.

Table 4.4: Electrochemical performance parameters obtained from EIS & Tafel polarization plots based on LZTS nanoparticles on ITO and FTO substrates

Counter Electrode	R_s (ohm)	R_{ct} (ohm)	Log J_0 ($mA.cm^{-2}$)	Log J_{lim} ($mA.cm^{-2}$)
Pt – ITO	78.7	282	-4.34	-4.45
LZTS – ITO	139.4	396	-4.49	-13.5
Pt – FTO	85.5	4.8×10^3	-5.57	-5.48
LZTS – FTO	267.6	2.5×10^6	-8.29	-15.4

The Tafel polarization curves are depicted in Fig. 4.11 where the interfacial charge-transfer properties of the symmetrical dummy counter electrodes cells are studied. Similarly to chapter 3, the J_0 and J_{lim} are reported. The J_0 value of LZTS–ITO was comparable to the state-of-the-art Pt suggesting good electrocatalytic activity. The J_{lim} value of LZTS using the ITO substrate was however smaller than Pt indicating lesser catalytic activity. Conversely, the J_0 and J_{lim} of LZTS using the ITO substrate were higher than the corresponding FTO, further suggesting that ITO should be the substrate of choice.

4.3.7. Device fabrication: dye-sensitized solar cells

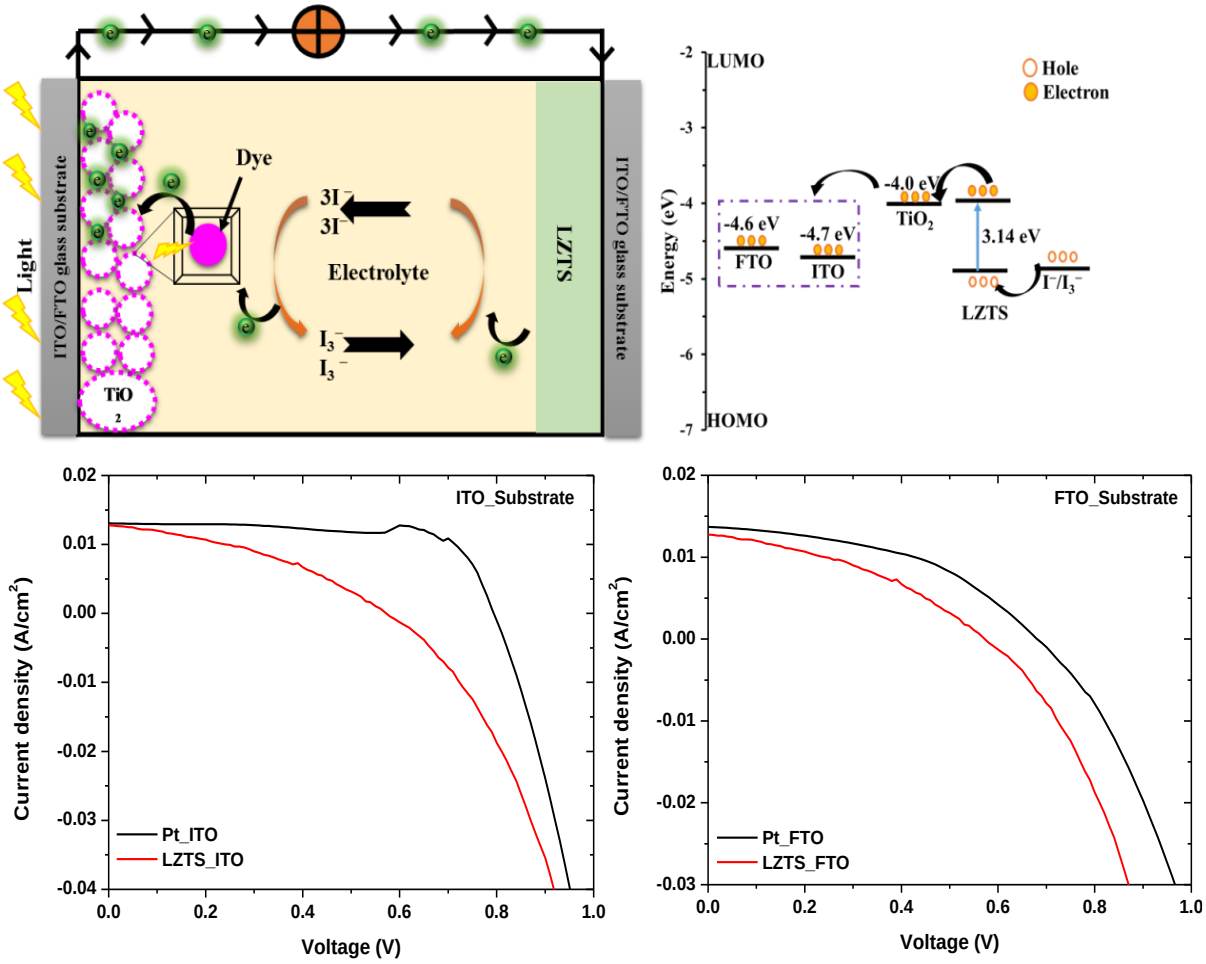

Fig. 4.1: DSSC set-up, band diagram and J-V curves of DSSCs of LZTS on ITO and FTO substrates.

In the same way, the LZTS nanoparticles were then used as CEs in DSSCs. Shown in Fig. 4.12 is the solar cell architecture, band structure and the resultant current density-voltage (J-V) curves derived from the two substrates. The performance of LZTS was compared against the state-of-the-art Pt electrode, however, it must be noted that these devices require further optimization. The results are also summarized in Table 4.5. Similarly to the CZTS and CZTSe study, it was observed that the change in substrate influenced the overall performance of the solar cell. The ITO substrate performed marginally better than the FTO substrate, although consistent with the electrochemistry data, the degree of change was lower than expected. This is strongly indicative of the need for optimization of the fabrication process. Also notably from Fig. 4.12 and the data in Table 4.5 are the low FF values across all samples. The low FF values

are due to the high R_s values and low shunt resistance (R_{sh}) values that are caused by the increased recombination at the interface of the DSSCs [21].

Table 4.5: J-V parameters of DSSCs of Pt and LZTS on ITO and FTO substrates

Counter Electrode	J_{sc} (mA.cm^{-2})	V_{oc} (V)	FF (%)	PCE (%)
Pt – ITO	13.38	0.95	52	6.57
LZTS – ITO	12.93	0.92	19	2.26
Pt – FTO	13.55	0.94	25	3.12
LZTS – FTO	12.67	0.87	20	2.19

4.4. Conclusions

LZTS nanoparticles were successfully synthesized for the first time using the hot-addition method. Varying the lithium source from LiCl to Li(acac) and Li_2S and the Li:Zn:Sn:S ratio from 1:1:1:1 to 2:1:0.25:2 resulted in a formation of LZTS nanoparticles with varying properties. The LiCl and Li(acac) derived particles, irrespective of ratios used resulted in the formation of impurities (i.e. unreacted material and/or unknown phases) as observed from the XRD patterns. The XPS, ^{7}Li MAS NMR and Raman spectroscopy confirmed the presence of lithium and the formation of LZTS. The Li_2S source, and the 2:1:0.25:2 ratio, resulted in the purest particles as such were used as CEs in DSSCs for the first time. Two types of substrates were utilized, namely ITO and FTO. The LZTS were used successfully as electrocatalysts in DSSCs. Using different substrates resulted in different PCEs. LZTS nanoparticles on ITO gave the best performance with 2.26% PCE. The PCE is comparable to the 3.62% of CZTS, 1.01% of CZTSe and 6.57% of Pt reported in Chapter 3. Furthermore, the PCE of CZTS was reported at 0.66% by Katagiri *et al.* [22] and this increased to 1.61% reported by Moritake *et al.* [23]. The LZTS material illustrates a higher PCE when compared to the first reported CZTS PCE values. This suggests that there is great potential in the LZTS material as a CE to reach and/or surpass the current reported PCE values for quaternary NPs. It must be noted that further optimization is still required.. Nevertheless, we have demonstrated that LZTS can be used as CEs in DSSCs.

References

[1] N. E. I. Boukortt, S. Patanè, *Optik*, 218 (2020) 165240.

[2] V. Probst, W. Stetter, W. Riedl, *Thin Solid Films*, 387 (2001), 262-267.

[3] P. Chawla, S. Jain, P. Vashishtha, M. Ahamed, S. N. Sharma, *Superlattices and Microstructures* 113 (2018) 502-509.

[4] K. P. Mubiayi, D. M. G. Neto, A. Morais, H. P. Nogueira, T. Emílio de Almeida Santos, T. Mazon, N. Moloto, M. J. Moloto and J. Nei Freitas, *Materials Chemistry & Physics*,. 242 (2020) 122449.

[5] S. Chen, A. Xu, J. Tao, H. Tao, Y. Shen, L. Zhu, J. Jiang, T. Wang and L. Pan, *ACS Sustainable Chemistry & Engineering* 3 (2015) 2652-2659.

[6] K. Mokurala, A. Kamble, C. Bathina, P. Bhargava and S. Mallick, *Materials Today: Proceedings*, 3 (2016) 1778-1784.

[7] M. Gratzel, *Curr. Opin. Colloid Interface Science*. 4 (1999) 314-21.

[8] S. S. Mali, P. S. Patil, C. Kook Hong, *ACS Applied Materials & Interfaces*, 6 (2014) 1688-1696.

[9] C. Ma, H. Guo, K. Zhang, Y. Li, N. Yuan, J. Ding, *Materials Letters*, 207 (2017) 209-212.

[10] Sharadrao A. Vanalakar, Pramod S. Patil, Jin H. Kim, *Solar Energy Materials and Solar Cells*, 182 (2018) 204-219.

[11] S. Sahayaraj, G. Brammertz, B. Vermang, T. Schnabel, E. Ahlswede, Z. Huang, S. Ranjbar, M. Meuris, J. Vleugels, J. Poortmans, *Solar Energy Materials and Solar Cells*, Volume 171, 2017, 136-141.

[12] J. W. Lekse, B. M. Leverett, C. H. Lake, J. A. Aitken, *Journal of Solid State Chemistry*, 181(2008) 3217-3222.

[13] A. Lafond, C. Guillot-Deudon, J. Vidal, M. Paris, C. La and S. Jobic, *Inorganic Chemistry*, 56 (2017) 2712-2721.

[14] Y. B. Smida, R. Marzouki, S. Kaya, S. Erkan, M. F. Zid, A. H. Hamzaoui, *IntechOpen*, (2020) 1-16. [DOI: http://dx.doi.org/10.5772/intechopen.93337]

[15] L. F. E. Machogo, P. Tetyana, R. Sithole, S. S. Gqoba, N. Phao, M. Airo, P. M. Shumbula, M. J. Moloto and N. Moloto, *Applied Surface Science*, 456 (2018) 973-979.

[16] R. K. Sithole, L. F. E. Machogo, M. A. Airo, S. S. Gqoba, M. J. Moloto, P. Shumbula, J. Van Wyk and N. Moloto, *New Journal of Chemistry*, 42 (2018) 3042-3049.

[17] A. Boulant, P. Maury, J. Emery, J.-Y. Buzare and O. Bohnke, *Chemistry of Materials*, 21 (2009) 2209-2217.

[18] A. Alanazi, F. Alam, A. salhi, M. Missous, A. Thomas, P. O'Brien and D. Lewis, *Royal Society of Chemistry Advance*, 9 (2019) 24146-24153.
[19] D. B. Khadka, J. Kim, *Journal of Alloys and Compounds*, 638 (2015) 103-108.
[20] V. Murugadoss, J. Lin, H. Liu, X. Mai, T. Ding, Z. Guo and S. Angaiah, *Nanoscale*, 11 (2019) 17579-17589.
[21] X. Qian, H. Li, L. Shao, X. Jiang and L. Hou, *ACS Applied Materials Interfaces*, 8 (2016) 29486-29495.
[22] H. Katagiri, N. Sasaguchi, S. Hando, S. Hoshino, J. Ohashi, T. Yokota, *Solar Energy Materials and Solar Cells*, 49 (1997) 407-414.
[23] N. Moritake, Y. Fukui, M. Oonuki, K. Tanaka, H. Uchiki, *Physica Status Solidi C*, 6 (2009) 1233-1236.

CHAPTER 5

The effect of Na-based precursors in the novel colloidal synthesis of Na_2ZnSnS_4 quaternary semiconducting nanocrystals and its application in dye-sensitized solar cells

5.1. Introduction

The development of renewable energy is sought after because of the environmentally friendly nature and long-term sustainability. The Cu-based quaternary semiconducting material have emerged from the chalcopyrite absorber layer material $CuIn_{1-x}Ga_xSe_2$ (CIGS). The power conversion efficiency (PCE) of CIGS has led to the further development of the popular CZTS and its derivatives, which are among the emerging *third generation* photovoltaics. To date, the use of alkali metals (K, Li, Na, Ca) have been used as dopants in the fabrication of solar cells [1-3]. The incorporation of alkali metals has shown significant improvement in the optical, crystallization, morphological and electrical properties of the Cu-based quaternary material [4, 5]. Among these alkali metals, the incorporation of sodium has been of particular interest.

The rudimentary method that was first reported in the incorporation of sodium was through the use of soda-lime glass (SLG) [6]. The diffusion of the sodium from the SLG to the Cu-based material, enhanced the electrical properties of the solar cell device. In recent years, to better understand the type of sodium (NaCl, NaF) that can be utilized, the amount and/or concentration of sodium required in the fabrication of solar cells and the effect it has on the composition of the Cu-based material has been studied [4-8]. The studies have focused on the diffusion methods, pre-treatment, in-synthesis and post-treatment of Na in solar cells. The diffusion method supplies minimum amount of Na and shows minimal effect in the efficiency of the solar cells. On the other hand, the pre-, in-synthesis and post-treatment of Na has resulted in the impact of morphology, increase in grain size and growth in the crystal of the Cu-based material. Werner *et al.* has reported that improving the open circuit voltage (V_{oc}), resulted in an increased conversion efficiency [9]. In addition, doping has shown to improve film conductivity of quaternary semiconducting material and prevent the formation of impurities such as secondary/ternary phases which are known to hinder the electrical performance [7].

The presence of Na has been reported to enhance crystallization and grain size regardless of the method it is introduced into the quaternary material/device fabrication. Therefore, the improvement in the crystal structure could help increase the efficiency of solar cells [8]. In this work, the replacement of Cu with Na, as an earth-abundant element with excellent electrical conductivity is proposed. The premise to develop Na_2ZnSnS_4 nanoparticles can yield promising semiconducting material for application in photovoltaics. Thus far, the synthesis NZTS has conducted using solid-state method only [10, 11]. Herein, , the colloidal synthesis of the chalcopyrite-type of NZTS nanoparticles is reported for the first time. The colloidal synthesis of NZTS is targeted to provide an improved crystallite structure of NZTS for its potential use as a counter electrode (CE) in dye-sensitized solar cells (DSSCs).

5.2. Experimental section

5.2.1 Materials

The same chemicals in Chapter 3 were used except for the monovalent cation precursors. In this case, sodium chloride (NaCl, anhydrous ≥ 99.0%), sodium sulfide nonahydrate ($Na_2S{\cdot}9H_2O$, ≥ 98%). All chemicals were purchased from Sigma Aldrich and used without further purification.

5.2.2 Colloidal synthesis of Na_2ZnSnS_4 nanoparticles

The methodology for the synthesis of NZTS was similar to that of LZTS reported in Chapter 4. Briefly, 10 mL of OLA was heated to 100 °C, while stirring under nitrogen gas. At 100 °C, the constituent precursors were added following a set sequence tabulated in Table 1. Following the addition of the third precursor, the temperature was raised to 220 °C. At 220 °C, the last precursor was added and held for 45 min. The mole ratio of the precursors were varied extensively to yield 1:1:1:1 and 2:1:0.5:4 of the Na:Zn:Sn:S samples for both reactions. The resultant particles were then flocculated using ethanol, recovered by centrifugation at 7000 rpm and dried at room temperature. Two Na precursors namely sodium chloride (NaCl) and sodium sulfide nonahydrate ($Na_2S{\cdot}9H_2O$) were used for this study.

Table 5.1: Synthetic procedure of NZTS

Reaction A	OLA $\xrightarrow[100\ °C]{\Delta}$ NaCl $\xrightarrow{\Delta}$ $ZnCl_2$ $\xrightarrow{\Delta}$ $SnCl{\cdot}5H_2O$ $\xrightarrow[220\ °C]{\Delta}$ S
Reaction B	OLA $\xrightarrow[100\ °C]{\Delta}$ $ZnCl_2$ $\xrightarrow{\Delta}$ S $\xrightarrow{\Delta}$ $Na_2S{\cdot}9H_2O$ $\xrightarrow[220\ °C]{\Delta}$ $SnCl{\cdot}5H_2O$

5.2.3 Device fabrication of the dye-sensitized solar cells

Counter electrode fabrication

The same method as in Chapter 3 was followed. However, the Na_2S 2:1:0.5:4 sample was used.

Photo-anode fabrication

The same method as in Chapter 3 was followed.

Device assembly

The same method as in Chapter 3 was followed.

5.2.4 Characterization

The same characterization techniques as in Chapter 3 were used. However, the solid-state ^{23}Na MAS NMR experiments were performed on a 11.8 T Bruker AVANCE III 500 MHz spectrometer (υ_0 = 132 MHz for ^{23}Na) using a 4.0 mm solids probe obtained using the one pulse MAS sequence at a spinning rate of 12 kHz.

5.3. Results and Discussion

5.3.1. Structural characterization of NZTS nanoparticles

The NZTS crystallizes in similar structures as CZTS, CZTSe and LZTS i.e. kesterite, stannite, or primitive mixed Cu-Au crystal phases. Notably, a lengthy optimisation process was conducted to determine the best order and precursor for the synthesis of NZTS. However, only the final reaction order for each precursor is reported and summarised in Table 5.1. The sodium chloride was selected based on the successful studies conducted with copper chloride-based

quaternary material. In addition, chloride is known as a good leaving group and thus, using any chloride-based precursor is ideal. Conversely, the sodium sulfide precursor was selected based on the successful synthesis of Li_2S_LZTS. The X-ray diffraction (XRD) of these structures are very similar with only small distinguishing features as previously mentioned in Chapter 3. The kesterite phase is usually 0.2° shifted from stannite and PMCA due to the larger distortion of the latter. The stannite and the PMCA are difficult to distinguish; however, the stannite is a more stable phase and such it is more prevalent of the two [12].

However, as previously discussed in Chapters 3 and 4, using the XRD experimental data and the lattice constants a, b and c, small differences in the XRD pattern can be detected and thus the two crystal structures can be distinguished. Fig. 5.1 shows the XRD patterns of NZTS nanoparticles synthesized using NaCl and $Na_2S{\cdot}9H_2O$ precursors, at different molar ratios and referenced to the standard stannite pattern. Both mole ratios of the NaCl-based precursor did not match perfectly with the reference pattern suggesting the presence of impurities (i.e. unreacted material and/or a variety of unknown and undesired crystal phase combinations). However, the change in precursor to $Na_2S{\cdot}9H_2O$ (which will be referred to as Na_2S) with the 2:1:0.5:4 (Na:Zn:Sn:S) ratio, matched perfectly with the reference pattern, however, not all planes were diffracted or were accounted for, suggesting preferred orientation. The energy difference between the PMCA and stannite phase is in the range 3–5 meV/atom and cannot be easily distinguished by just using XRD [13, 14].

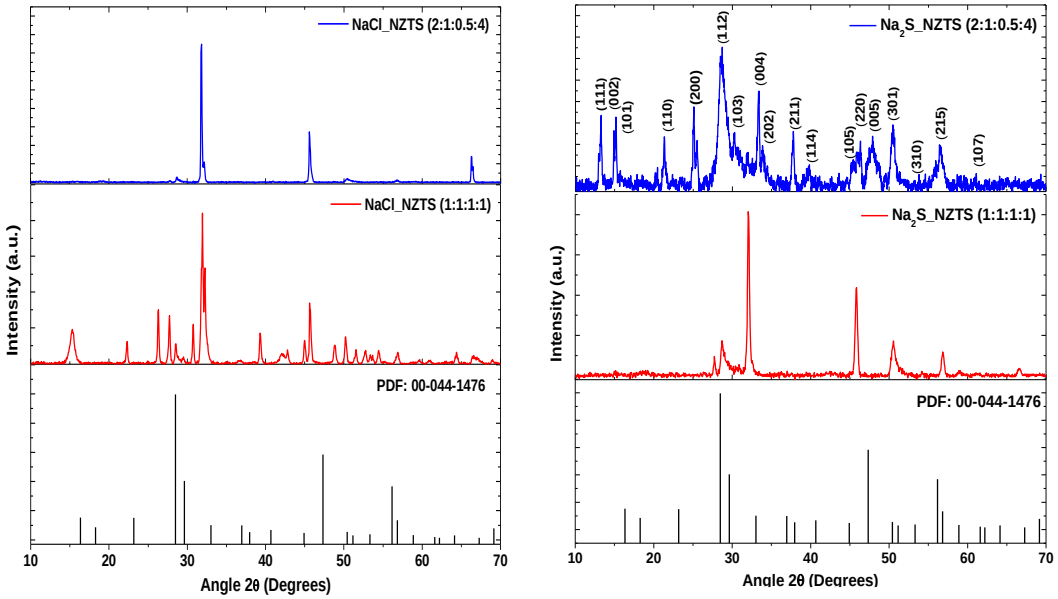

Fig. 5.1: X-ray diffractograms of the Na_2ZnSnS_4 nanoparticles synthesized with different sodium precursors (NaCl and Na_2S), precursor ratios (1:1:1:1 and 2:1:0.5:4) and the standard reference pattern.

Equation 2.2 and the XRD experimental data were used to determine the lattice constants a, b and c for Na_2S_NZTS (2:1:0.5:4) nanoparticles because similarly to Li_2S_LZTS, it was the only sample that matched the standard reference pattern. The calculated experimental values are tabulated (Table 5.2) including the single crystal stannite NZTS material, for structural comparison. The tetragonal distortion ratio of the single crystal stannite NZTS material is similar and comparable to that of the Na_2S_NZTS nanoparticles. In addition, the lattice constants of Na_2S_NZTS c ≈ a suggesting a PMCA crystal phase. Therefore, similarly to the LZTS nanoparticles, the preferred orientation of NZTS is closer to PMCA. The slight change in crystalline parameters could be due to the increased atomic radii of Cu (128 ppm) and Na (186 ppm). Lithium and sodium are group one alkali metals and this suggests that the nanoparticles could have similar properties. In addition, transition metals (Cu/Ag) are harder than alkali metals due to the number of unpaired electrons in their valence shells as such; this might promote the distortion of the tetragonal structure in NZTS.

Table 5.2: Lattice parameters of tetragonal NZTS structures.

Structure	a=b (Å)	c (Å)	c/a	Reference
Single crystal (ST)	6.480	9.120	1.407	[10]
	6.484	9.134	1.409	[11]
Na_2S_NZTS (*exp.*)	8.320	11.978	1.440	

5.3.2. Solid-state NMR characterization of NZTS nanoparticles

To confirm the presence of sodium in the formation of NZTS, ^{23}Na MAS NMR was conducted. The NaCl precursor and the corresponding NZTS nanoparticles are shown in Fig. 5.2. The ^{23}Na MAS NMR peaks have been reported over a wide range that is between 50 and -50 ppm. The sodium peak was observed in the commercial NaCl precursor at 9.92 ppm, which is within range [15]. The NaCl based nanoparticles with the 1:1:1:1 ratio was observed to have two peaks at 9.99 and 3.12 ppm. This suggests that, the nanoparticles could have at least two different Na sites. The peak at 3.12 pm could be due to oxidation of sodium [16]. The 2:1:0.5:4 ratio of the NaCl based nanoparticles detected one peak at 9.85 ppm. The Na_2S_NZTS depicted peaks at 9.84 and 9.98 ppm for the 1:1:1:1 and 2:1:0.5:4 ratios respectively. Due to the highly hygroscopic nature of $Na_2S{\cdot}9H_2O$, the NMR analysis could not be conducted. The slight shifts observed in all the samples were indicative of the presence of Na and that the individual samples are indistinctly different from each other.

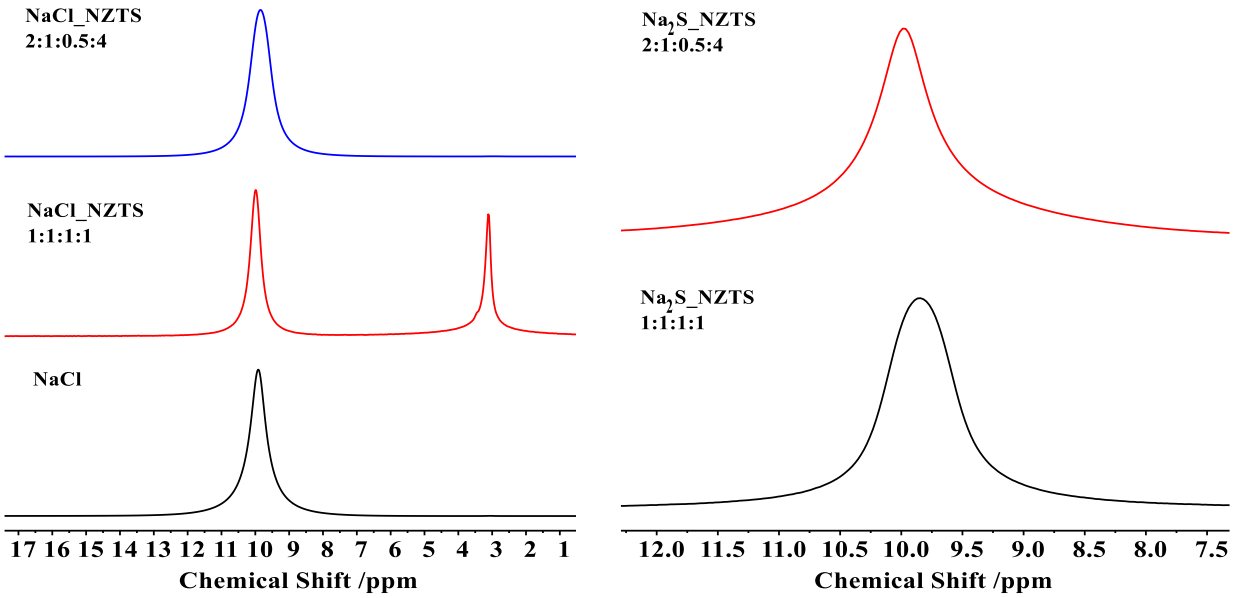

Fig. 5.2: ^{23}Na MAS NMR spectra illustrating the ratio study of NZTS using NaCl and Na_2S as different sodium precursors, including the NaCl starting material.

5.3.3. XPS characterization of NZTS nanoparticles

The XPS survey spectra (Fig. 5.3) show all the elements of NZTS with the exception of the NaCl-based nanoparticles (1:1:1:1) ratio. The evaluation of the surface also illustrates other elements observed namely, C, N and O because of the surfactant – OLA [17]. The C 1s, N 1s and O 1s spectra from all the NZTS nanoparticles are shown in *Fig. 5.1S to Fig. 5.4S*. The detection of these elements is indicative of the successful capping of the nanoparticles.

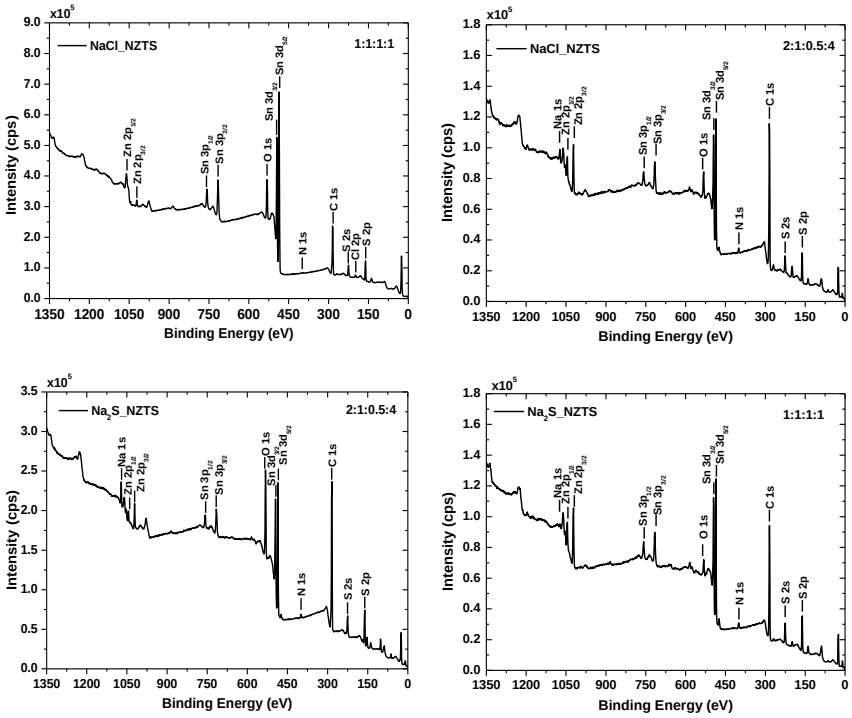

Fig. 5.3: survey spectra of the three Na precursor sources for 1:1:1:1 and 2:1:0.25:2 ratios.

The Na 1s high-resolution spectra (Fig. 5.4) illustrated the quantity of sodium for the NZTS nanoparticles including the hidden peaks not observed in the survey spectrum for NaCl-based (1:1:1:1) ratio nanoparticles. The high-resolution spectrum is more sensitive to low concentrations in comparison to the survey spectrum therefore, sodium was detected for all samples. The 1:1:1:1 ratio NaCl and Na_2S-based nanoparticles indicated a low concentration of Na 1s as anticipated. The intensity of the Na_2S_NZTS nanoparticles with the 2:1:0.5:4 ratio was much higher compared to the NaCl_NZTS nanoparticles and this was indicative of the presence of enough Na hence the formation of NZTS that is consistent with the XRD results.

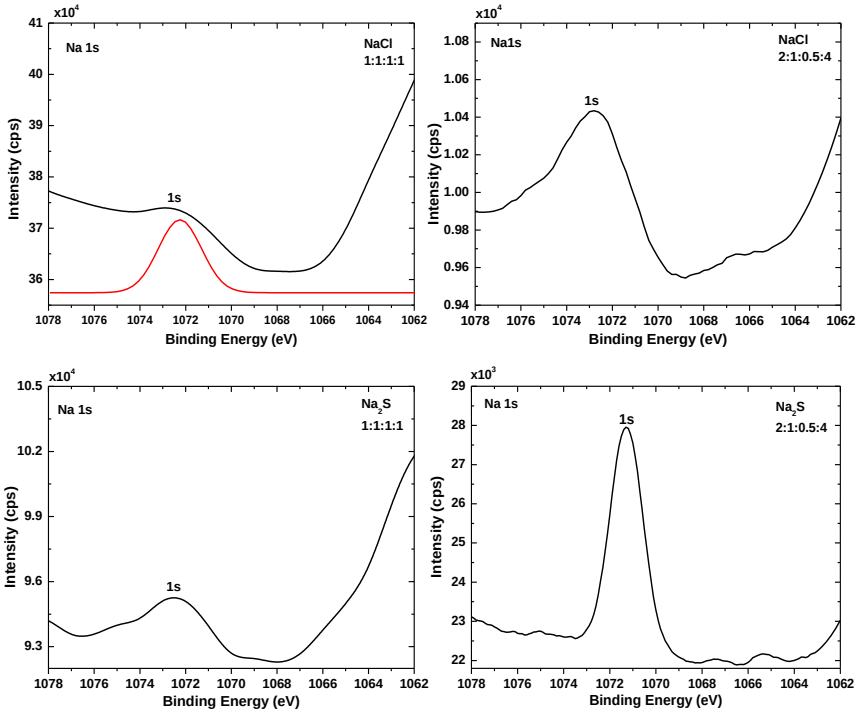

Fig. 5.4: Na 1s high-resolution spectra of NZTS nanoparticles synthesized from different sodium sources (i.e. NaCl and Na_2S) at different precursor ratios.

The high-resolution spectra of Zn 2p, Sn 3d and S 2p for both 1:1:1:1 and 2:1:0.5:4 ratios of the NZTS nanomaterial are observed below (Fig. 5.5 – 5.7). The Zn 2p peaks illustrated a doublet that is split into peaks found at ~1044 eV ($2p_{1/2}$) and ~1021 eV ($2p_{3/2}$). The difference in the split is in the range 22.39 eV – 23.17 eV and is ascribed to the Zn^{2+} species. Similarly, the Sn 3d peaks showed a doublet, with a split at ~494 eV ($3d_{3/2}$) and ~485 eV ($3d_{5/2}$). The difference is much smaller in range 8.38 eV – 8.46 eV. The peak separation is ascribed to the Sn^{4+} ion species. The Sn 3d NaCl_NZTS 1:1:1:1 has two pairs of peaks as illustrated. The difference between the dominant peaks is 8.40 eV and difference between the shoulder peaks is 8.38 eV. Both peaks are assigned to $3d_{3/2}$ and $3d_{5/2}$ respectively. The shoulder peaks are shifted downwards due to the alignment of the energy bands at the interface. The shoulder peaks could be attributed to the presence of an oxide (i.e. SnO_x). Lastly, the S 2p showed a prominent peak with a shoulder peak that is deconvoluted into $2p_{1/2}$ and $2p_{3/2}$ respectively. The deconvoluted peaks are associated with S^{2-} species. The oxidation states identified for each element are in good agreement with what has been previous observed for similar material such

as CZTS, CZTSe and Na-doped CZTS [18-21]. The atomic percentages of each element are shown in *Table 5.1S – 5.4S*.

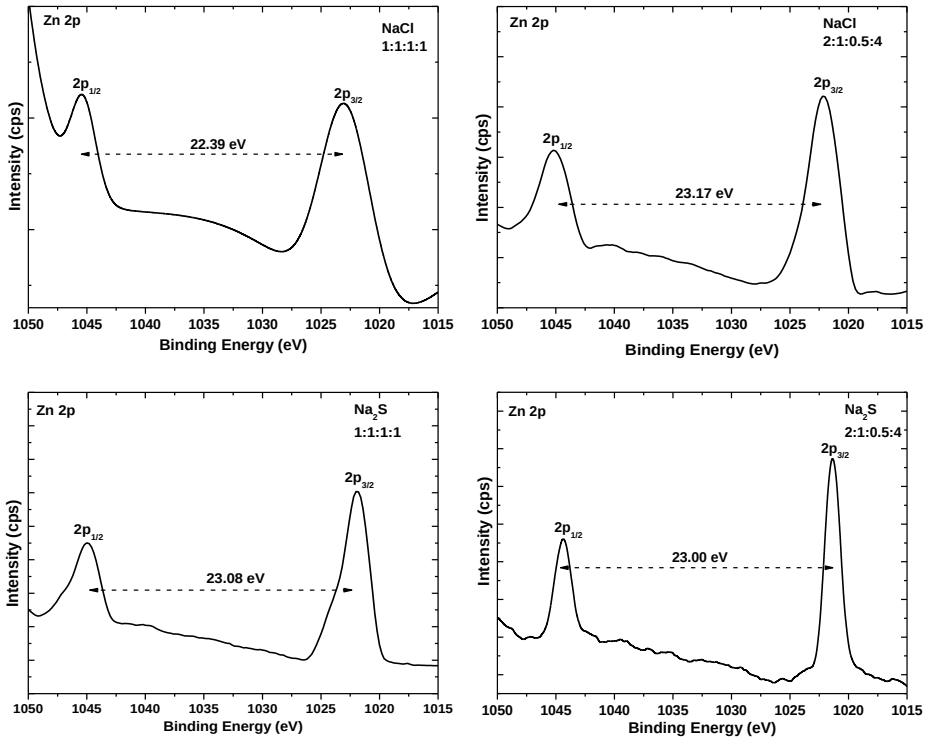

Fig. 5.5: The high-resolution spectra of Zn 2p NZTS.

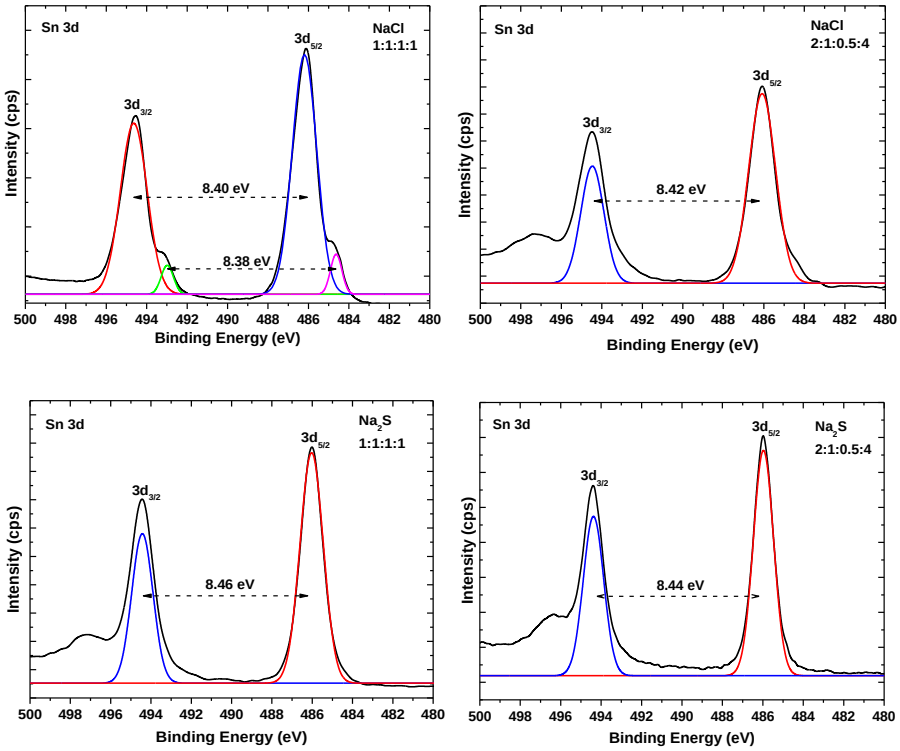

Fig. 5.6: The high-resolution spectra of Sn 3d NZTS.

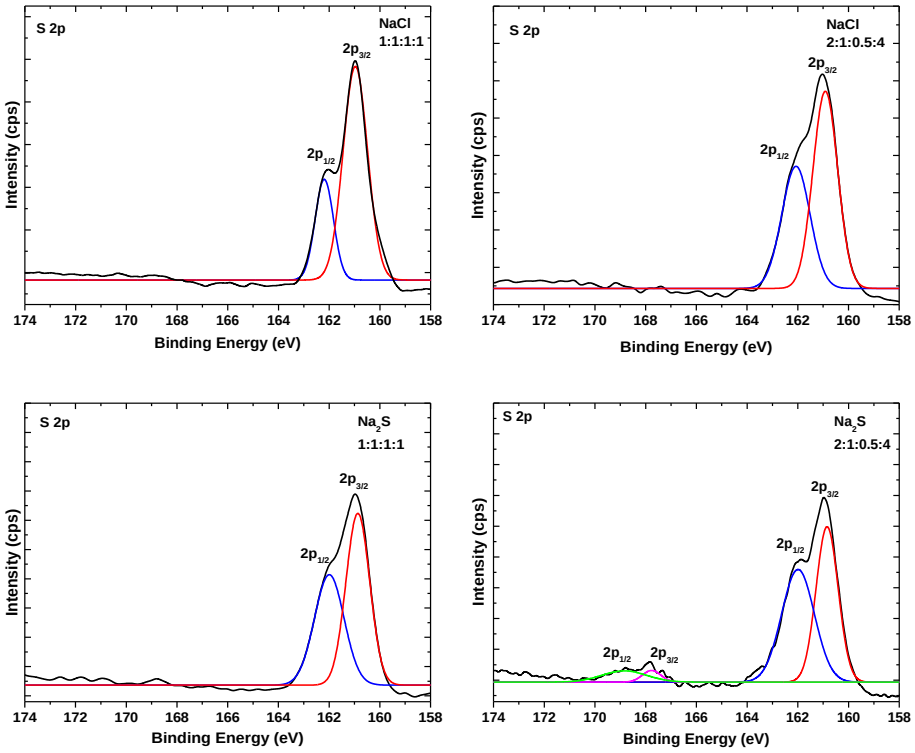

Fig. 5.7: The high-resolution spectra of S 2p of NZTS.

5.3.4. Morphological characterization of NZTS nanoparticles

The TEM images shown in Fig. 5.8 were from the different precursors and mole ratios. The NaCl-based nanoparticles were mostly spherical, poly-dispersed and agglomerated. The 2:1:0.5:4 NaCl-based nanoparticles showed a wide range of sizes. The Na_2S_NZTS nanoparticles with the 1:1:1:1 ratio, show some mixed morphology and agglomeration causing the particles to appear cubic, elongated and closely packed. The 2:1:0.5:4 ratio Na_2S_NZTS nanoparticles, illustrate quasi-spherical morphology and poly-dispersed.

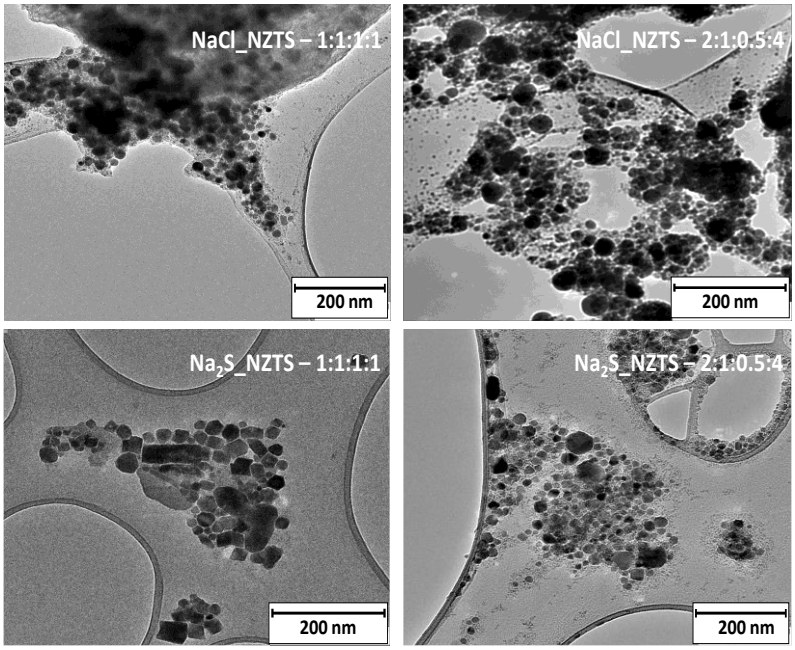

Fig. 5.8: TEM micrographs of NZTS nanoparticles synthesized from different sodium precursors (NaCl and Na_2S) at different ratios (1:1:1:1 and 2:1:0.5:4).

5.3.5. Optical analysis of NZTS nanoparticles

The band gaps of the NaCl and Na_2S derived nanoparticles were determined through optical absorption spectroscopy. The Tauc plots were derived from UV–vis spectra (Fig. 5.9) show the extrapolated band gap values for 1:1:1:1 and 2:1:0.5:4 ratio NaCl-based nanoparticles were 1.36 eV and 2.62 eV respectively. On the other hand, the Na_2S-based nanoparticles illustrated 3.04 eV and 3.28 eV band gaps for 1:1:1:1 and 2:1:0.5:4 ratios, respectively. The Na_2S nanoparticles depict wider band gap values in comparison to NaCl derived nanoparticles. Wide band gap semiconductors are reported to have desirable properties such as high electron saturation velocity and high electric breakdown field [22, 23]. The wide band gap material can be applied under high temperature (i.e. ~300 °C compared to the maximum of ~100 °C of silicon material), power, frequency and anti-radiation environments [22, 23] making the Na_2S_NZTS material very desirable for the application of solar cells in harsh environments.

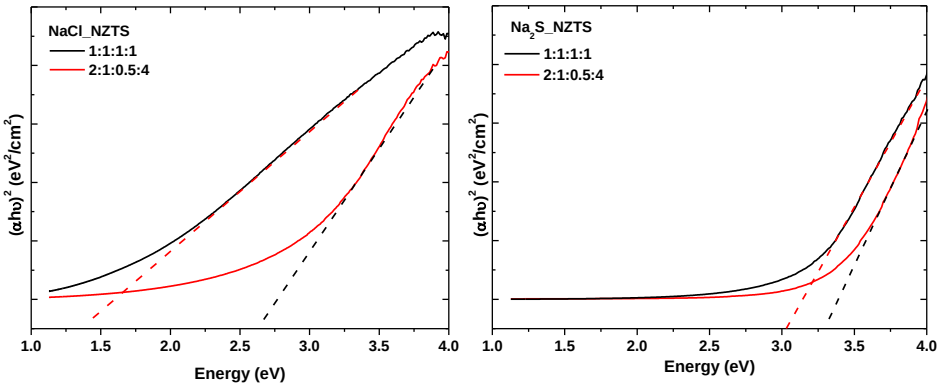

Fig. 5.9: Tauc plots of NZTS nanoparticles using NaCl and Na_2S precursors with varying mole ratios (1:1:1:1 and 2:1:0.5:4).

5.3.6. Raman characterization of NZTS nanoparticles

In light of all the above characterization results and the complete transformation of the precursors into NZTS, the Na_2S_NZTS (2:1:0.5:4) nanoparticles were used for further characterization (*see appendix*: Fig. 5.8S for NaCl_NZTS). The Raman spectrum illustrated below, further confirmed the crystal structure of the nanoparticles. Fig. 5.10 illustrated a prominent peak at 348 cm^{-1}, which was within range of stannite crystal structures [10]. The additional Raman peaks, deconvoluted at 288 cm^{-1}, 307 cm^{-1} and 387 cm^{-1} belong to the A_1 mode, the 316 cm^{-1} and 364 cm^{-1} belonged to the B_2 mode and the 330 cm^{-1} and 376 cm^{-1} belonged to the E mode [24].

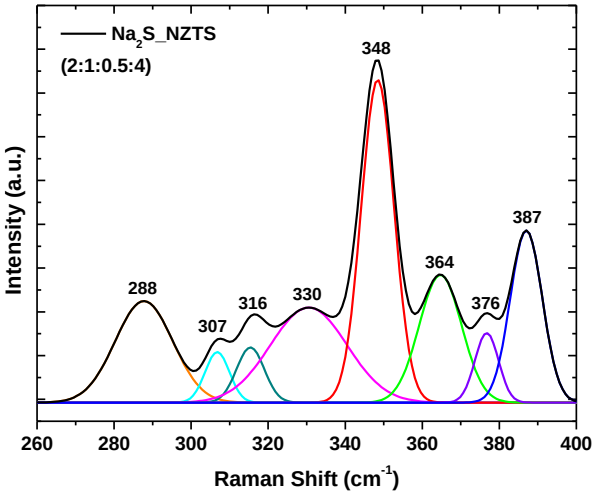

Fig. 5.10: Raman spectrum of Na_2S_NZTS 2:1:0.5:4 ratio nanoparticles using the 785 nm laser.

5.3.7. FT-IR and liquid-state NMR of NZTS nanoparticles

The organic capping ligand was determined using XPS, FT-IR and NMR [16, 25]. From FT-IR, the main functional groups were identified in the pure OLA and NZTS nanoparticles. Similar to Chapter 3, the observed functional groups were the C=C, CH_2/CH_3 and NH_2. Fig. 5.5S showed the spectra of OLA with the N-H stretch at 3376 cm^{-1}, the N-H bend at 1617 cm^{-1}, the C-H stretch were found at 3002 cm^{-1}, 2923 cm^{-1}, 2849 cm^{-1} and the C-H bend at 1465 cm^{-1}. The intensity of N-H bend/stretch was diminished due to the high intensity of the C-H bend/stretch. The OLA-capped NZTS nanoparticles showed peaks in the range 2849 – 3002 cm^{-1} region, that are characteristic of the oleyl group but no peak was observed at 3300 cm^{-1} due to the N-H stretch. This suggests the successful capping of OLA through the amine, henceforth the weakening of the signal. The peaks observed in the 2000 cm^{-1} region were attributed to overtones.

NMR spectroscopy was done to elucidate the capping agent. The NMR spectra are shown in *Fig. 5.6S* and *Fig. 5.7S*. The summary of the results is tabulated in Table 5.3. All protons and carbons were accounted for in the pure OLA as observed from the ^1H NMR and ^{13}C NMR, such that functional groups ($CH_3(CH_2)_7CH=CH(CH_2)_7CH_2NH_2$) are depicted on the spectrum. The OLA was distinguished by the $-NH_2$ (1.34 – 1.37 ppm) and the $-CH_2-NH_2$ (2.58 – 2.63 ppm) chemical shifts in the ^1H spectrum and the $-CH_2-NH_2$ (42.27 ppm) peak in the ^{13}C spectrum. The $-NH_2$ protons and the $-CH_2-NH_2$ protons in both the CZTS and CZTSe spectra were diminished. This further suggested that the capping agent OLA was bound to the

nanoparticles through the amine. The ^{13}C NMR spectra for CZTS and CZTSe further showed the absence of the $-CH_2-NH_2$ carbon peak, again cementing the conclusion that the capping agent binds through the amine. No C-O, C=O or O-C=O peaks were observed in the ^{13}C NMR spectra of CZTS and CZTSe thereby suggesting that these species were only as a result of surface oxidation.

Table 5.3: NMR assignments for OLA and Na_2S_NZTS (2:1:0.5:4) nanoparticles.

Compound	^1H NMR (δ ppm)	^{13}C NMR (δ ppm)
OLA	$-CH_3-$ (0.79 – 0.87), $-CH_2-$ (1.19 – 1.23), $-NH_2$ (1.34 – 1.37), $-H_2C-HC=CH-CH_2-$ (1.94 – 2.09), $-H_2C-NH_2$ (2.58 – 2.63), -HC=CH- (5.26 – 5.31)	$-CH_3-$ (14.11), $-H_2C-CH_3$ (22.70), $-CH_2-$ (26.93 – 33.89), $-H_2C-NH_2$ (42.27), -HC=CH- (129.81 – 130.36)
Na_2S_NZTS (2:1:0.5:4)	$-CH_3-$ (0.85 – 0.90), $-CH_2-$ (1.27), $-NH_2$ (1.77 – 2.94), -HC=CH- (5.34, 5.38)	$-CH_3-$ (14.27), $-H_2C-CH_3$ (22.84), $-CH_2-$ (27.37 – 32.77), -HC=CH- (130.12)

5.3.8 Electrochemical characterization of Na_2S_NZTS nanoparticles

The NZTS nanoparticles where investigated as potential electrocatalysts. Cyclic voltammetry measurements were conducted using the three-electrode system and the results were reported in the cyclic voltammograms (CVs) shown in Fig. 5.11.

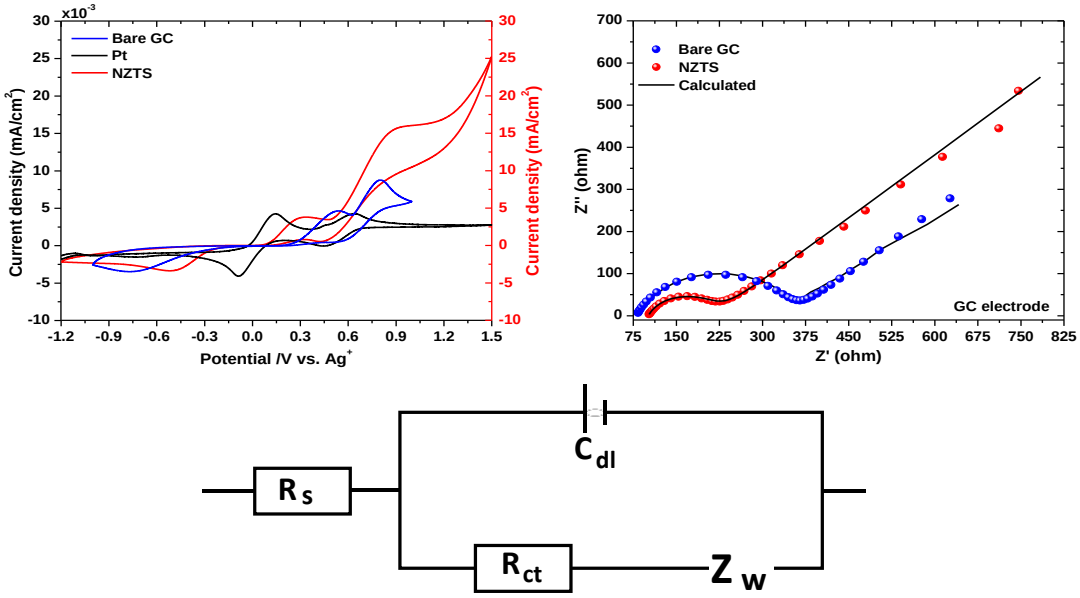

Fig. 5.11: Cyclic voltammograms of Pt and Na_2S_NZTS (2:1:0.5:4) counter electrodes analysed at a scan rate of 50 mV/s (a), EIS plot of NZTS counter electrode on a glassy carbon substrate (b) and the equivalent electrochemical circuit model (c).

There are two rudimentary parameters, i.e. peak current $|J_{_Red\text{-}1}|$ and peak-to-peak separation (E_{pp}), which illustrate the catalytic activity of the electrodes. Table 5.4 summarizes the E_{pp} values 0.44 (Pt) and 0.85 (NZTS) while the $|J_{_Red\text{-}1}|$ values are 6.07 mA/cm^2 and 3.88 mA/cm^2 respectively. The higher peak current and lower E_{pp} values suggest better catalytic performance and larger reduction velocity [26]. The Red_I shift observed for the NZTS and Pt electrodes towards the positive potential are indicative of good reversibility of the reaction relative to the bare GC.

Table 5.2: CV and EIS parameters for NZTS on glassy carbon substrate.

Counter Electrode	Epp (V)	J_{sc} (mA.cm^{-2})	R_s (ohm)	R_{ct} (ohm)
Pt	0.44	6.07	–	–
NZTS – GC	0.85	3.88	101.7	120

The EIS measurement (Fig. 5.12) was conducted on the glassy-carbon substrate with Na_2S_NZTS (2:1:0.5:4) ratio nanoparticles. The Nyquist plot exhibits an arc (semi-circle) and the insert illustrates the electrochemical equivalent circuit that was generated from fitting the experimental data. The various symbols on the circuit represent the four impedance properties: R_s – series resistance, R_{ct} –charge transfer resistance, C_{dl} – double layer capacitance, Z_w – Nernst diffusion element. The R_s represents the bulk solution resistance of the electrolyte while the R_{ct} is the charge transfer resistance at the CE/electrolyte interface. Low R_{ct} values are ideal because they are indicative of good charge transfer. Moreover, the C_{dl} corresponds to electrical double layer capacitance, employed when a perfect semi-circle is obtained from the Nyquist plot and explains the charge storage capacity of the counter electrodes. In addition, the Z_w represents Nernst diffusion that is generally employed when a line is at 45° to the semi-circle at the lower frequency region. It further explains whether the interaction of the CE and the electrolyte are diffusion-controlled [26]. Further EIS measurements were conducted on symmetrical dummy cells, drop-casted with two identical counter electrode material on ITO and FTO substrates respectively. The electrodes were filled with I^-/I_3^- electrolyte and measured in the dark. Similarly, to the GC substrate, the same equivalent circuit model was observed for the symmetrical cells (Fig. 5.12).

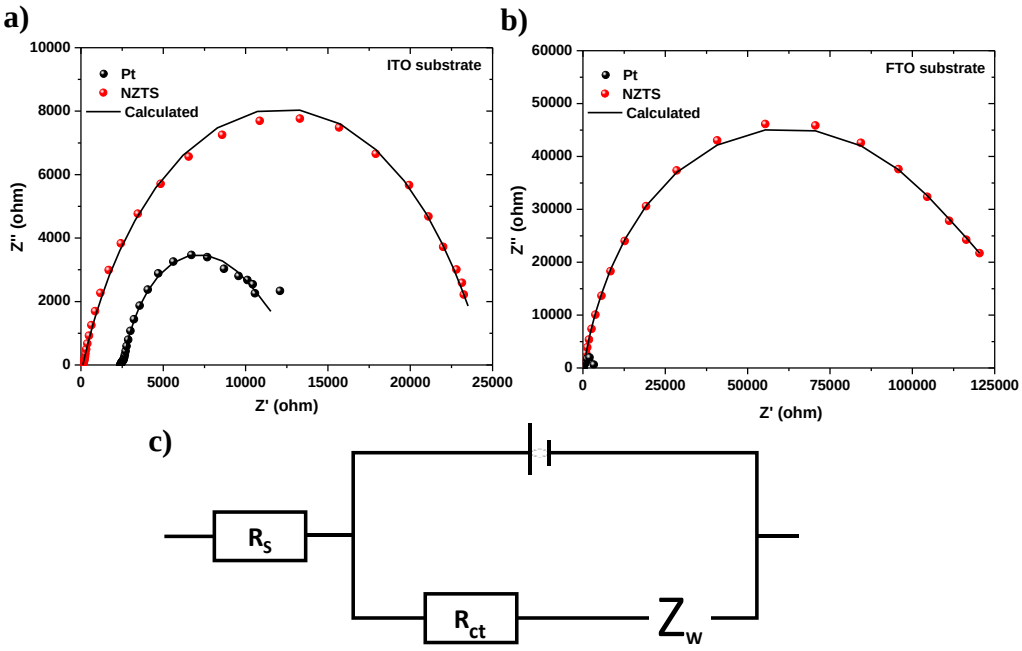

Fig. 5.12: (a) The equivalent circuit model of Na_2S_NZTS (2:1:0.5:4) with the EIS measurements on (b) ITO (left) and (c) FTO.

The R_s and R_{ct} values were reported in Table 4 for Pt and NZTS nanoparticles on ITO and FTO substrates. Pt and NZTS display lower R_s values on ITO substrates when compared to the FTO substrate. Regardless of the substrate, the conductive of Pt is still unmatched. As previously charge transfer is exhibited through the diameter of the semi-circle on the high frequency region and it is reflected by the R_{ct} values. For optimal device performance, low R_{ct} values are desirable because they lead to high peak current (J_{sc}) and fill factor (FF) values. The change in substrates from ITO to FTO showed that R_s and R_{ct} values increased. Therefore, the increase suggests that FTO based solar cells might demonstrate poor performance.

Table 5.3: Electrochemical performance parameters obtained from EIS and Tafel polarization plots based on Na_2S_NZTS (2:1:0.5:4) nanoparticles on ITO and FTO.

Counter Electrode	**R_s (ohm)**	**R_{ct} (ohm)**	**Log J_0 ($mA.cm^{-2}$)**	**Log J_{lim} ($mA.cm^{-2}$)**
Pt – ITO	78.7	282	-4.34	-4.45
NZTS – ITO	119.6	341	-5.27	-12.68
Pt – FTO	85.5	4.8×10^3	-5.57	-5.48
NZTS – FTO	166	1.2×10^5	-6.98	-13.01

The Tafel plots are depicted in Fig. 5.13 and the log values are summarized in Table 5.4. The J_0 and J_{lim} values of NZTS-ITO were smaller when compared to Pt, suggesting the material has lesser electrocatalytic activity. In addition, the NZTS J_0 and J_{lim} values of the ITO substrate were higher than FTO, which further cements the use of ITO as the substrate of choice.

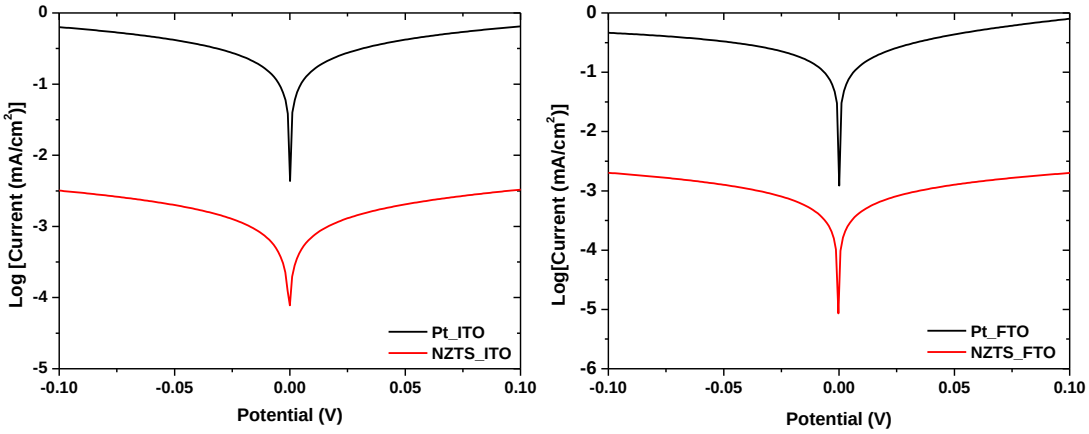

Fig. 5.13: Tafel polarization curves of Pt and Na_2S_NZTS (2:1:0.5:4) using dummy symmetrical electrodes on ITO and FTO substrates.

5.3.9 Device fabrication: dye-sensitized solar cells

The J-V curves are illustrated in Fig. 5.14. The Pt and NZTS CEs were analysed under the same conditions. Table 5.5 summarizes all the values that further determine the performance of CEs.

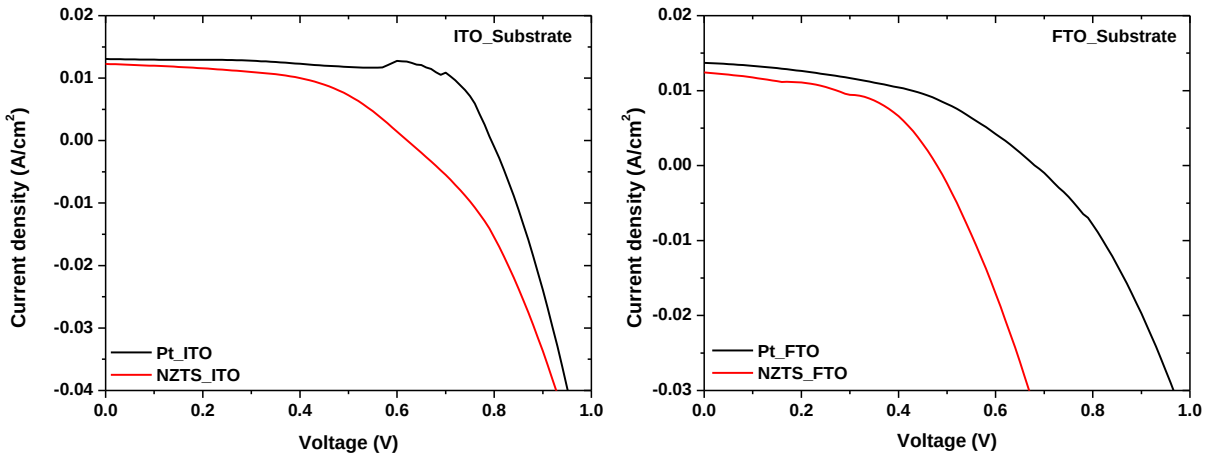

Fig. 5.14: J-V curves of DSSCs of Pt and Na_2S_NZTS 2:1:0.5:4 on ITO and FTO substrates.

Table 5.4: J-V parameters of DSSCs of Pt and NZTS on ITO and FTO substrates.

Counter Electrode	J_{sc} ($mA.cm^{-2}$)	V_{oc} (V)	FF (%)	PCE (%)
Pt – ITO	13.38	0.95	52	6.57
NZTS – ITO	12.28	0.93	34	3.93
Pt – FTO	13.55	0.94	25	3.12
NZTS – FTO	12.46	0.67	31	2.62

Changing from ITO to FTO substrates continues to prove that the effect of the substrate does influence the overall performance of a device. The ITO substrate was observed to perform marginally better than FTO substrate. Similarly to LZTS, the varied performance can be due to better adhesion of the NPs to the ITO substrate as opposed to the FTO substrate. As mentioned thin-film analysis (i.e. SEM/AFM) could be done to further confirm this hypothesis. It was anticipated that NZTS would display more comparable results to the state-of-the-art Pt due to the promising electrochemical results observed however; the degree of change was lower than expected. Therefore, the fabrication process of the device requires further optimization. Similarly, to LZTS the FF values obtained are much lower than expected. This was due to the high series resistance and low shunt resistance (R_{sh}), caused by increased recombination at the DSSC interfaces [27].

5.4. Conclusions

The NZTS nanoparticles were successfully synthesized for the first time using the hot-addition colloidal method. The NaCl and Na_2S precursors with the ratios 1:1:1:1 and 2:1:0.5:4 representing Na:Zn:Sn:S resulted in various crystallite formations of NZTS nanoparticles. The NaCl based nanoparticles resulted in impurities (i.e. unreacted material and/or a variety of unknown and undesired crystal phase combinations) as observed in the XRD patterns. The ^{23}Na MAS NMR, XPS and Raman spectroscopy confirmed the presence of sodium and the complete transformation of the precursors into NZTS nanoparticles. Na_2S in the 2:1:0.5:4 ratio, resulted in the purest particles hence, they were used as CEs in DSSCs. In addition, Na_2S precursor was found to be the more suitable precursor due to its highly reactive nature when compared to the NaCl precursor. Two transparent conductive oxides (TCOs) namely, ITO and FTO substrates were used. It is worth noting that the NZTS nanoparticles were successfully utilized as electrocatalysts in DSSCs. The use of different substrates resulted in varying PCEs. The NZTS

nanoparticles on ITO substrate resulted in the best performance and reported a 3.93% PCE. NZTS nanoparticles have demonstrated viable CE properties in DSSCs however, as previously mentioned, further full optimization is required such as varying the layers of the NPs, exploring different electrolytes and/or dye.

References

[1] Z. Tong, C. Yan, Z. Su, F. Zeng, J. Yang, Y. Li, L. Jiang, Y. Lai, F. Liu, *Applied Physics Letters*, 105 (2014) 223903.

[2] Z. Wang, N. Brodusch, R. Gauvin, G. P. Demopoulos, *Nano Energy*, 53 (2018) 130-134.

[3] S. Berman, G. S. Gautam, E. A. Carter, *ACS Sustainable Chemical Engineering*, 7 (2019) S792-S800.

[4] C. Andres, T. Schwarz, S. G. Haass, T. P. Weiss, R. Carron, R. Caballero, R. Figi, C. Schreiner, M. Burki, A. N. Tiwari, Y. E. Romanyuk, *Solar Energy*, 175 (2018) 94-100.

[5] T. Abzieher, T. Schnabel, M. Hetterich, M. Powalla, E. Ahlswede, *Physics Status Solidi A*, 213 (2016) 1039-1049.

[6] H. Xin, S. M. Vorpahl, A. D. Collord, I. L. Braly, A. R. Uhl, B. W. Krueger, D. S. Ginger, H. W. Hillhouse, *Physical Chemistry Chemical Physics*, 17 (2015) 23859-23866.

[7] T. Gershon, B. Shin, N. Bojarczuk, M. Hopstaken, D. B. Mitzi, S. Guha, *Advanced Energy Materials*, 5 (2015) 1400849.

[8] C. M. Sutter-Fella, J. A. Stuckelberger, H. Hagendorfer, F. L. Mattina, L. Kranz, S. Nishiwaki, A. R. Uhl, Y. E. Romanyuk, A. N. Tiwari, *Chemistry of Materials.*, 26 (2014) 1420-1425.

[9] M. Werner, C. M. Sutter-Fella, Y. E. Romanyuk, A. N. Tiwari, *Thin Solid Films*, 582 (2015) 308-312.

[10] G. Bousselmi, N. Khemiri, A. Benali, M. P. F. Graca, R. F. Santos, B. F. O. Costa, M. Kanzari, *Journal of Materials Science: Material Electron*, 21 (2020) 18858-18869.

[11] J. He, Y. Guo, W. Huang, X. Zhang, J. Yao, T. Zhai, F. Huang, *Inorganic Chemistry*, 58 (2018) 9918-9924.

[12] C. Persson, *Journal of Applied Physics*, 107 (2010) 053710.

[13] A. Khare, B. Himmetoglu, M. Johnson, D. J. Norris, M. Cococcioni, E. S. Aydil, *Journal of Applied Physics*, 111(2012) 083707.

[14] B. G. Mendis, M. D. Shannon, M. C. J. Goodman, J. D. Major, R. Claridge, D. P. Halliday, K. Durose, *Progress in PV: Research and Applications*, 22 (2020) 24-34.

[15] T. Iijima, T. Yamase, K. Nishimura, *Solid State Nuclear Magnetic Resonance*, 76-77 (2016) 15-23.

[16] L. Gao, J. Chen, Y. Liu, Y. Yamauchi, Z. Huang, X. Kong, *Journal of Materials Chemistry A*, 6 (2018) 12012-12017.

[17] R. K. Sithole, L. F. E. Machogo, M. A. Airo, S. S. Gqoba, M. J. Moloto, P. Shumbula, J. Van Wyk and N. Moloto, *New Journal of Chemistry*, 42 (2018) 3042-3049.

[18] O. Selyshchev, Y. Havryliuk, M. Y. Valakh, V. Yukhymchuk, O. Raievska, O. L. Stroyuk, V. Dzhagan, D. R. T. Zahn, *ACS Applied Nano Materials*, 3 (2020) 5706-5717.

[19] X. Zhang, Y. Xu, J. Zhang, S. Dong, L. Shen, A. Gupta, N. Bao, *Scientific Reports*, 8 (2018) 248.

[20] M. A. Munoz-Marquez, M. Zarrabeitia, E. Castillo-Martinez, A. Eguia-Barrio, T. Rojo, M. Casas-Cabanas, *ACS Applied Materials Interfaces*, 7 (2015) 7801-7808.

[21] P. –Y. Lee, S. –P. Chang, S. –J. Chang, *Journal of Environmental Chemical Engineering*, 3 (2015) 297-303.

[22] A. Yoshikawa, H. Matsunami and Y. Nanishi, *Wide Bandgap Semiconductors*, (2007) 1-24.

[23] L.-C., Tien and C.-H. Ho, *Gallium Oxide*, (2019) 67-90.

[24] S. P. Ramkumar, Y. Gillet, A. Miglio, M. J. van Setten, X. Gonze, G. –M. Rignanese, *Physics Review B*, 94 (2016) 224302.

[25] L. F. E. Machogo, P. Tetyana, R. Sithole, S. S. Gqoba, N. Phao, M. Airo, P. M. Shumbula, M. J. Moloto and N. Moloto, *Applied Surface Sciences*, 456 (2018) 973-979.

[26] V. Murugadoss, J. Lin, H. Liu, X. Mai, T. Ding, Z. Guo and S. Angaiah, *Nanoscale*, 11 (2019) 17579-17589.

[27] X. Qian, H. Li, L. Shao, X. Jiang and L. Hou, *ACS Applied Materials Interfaces*, 8 (2016) 29486-29495.

CHAPTER 6
Overall conclusions and recommendations

6.1. Conclusions

The findings in this thesis report on the colloidal synthesis of quaternary semiconducting nanoparticles CZTS and CZTSe, including the first time colloidal synthesis of LZTS and NZTS nanoparticles respectively. The optical properties of the CZTS and CZTSe illustrated band gaps of 1.3 eV and 1.8 eV respectively. While the Li_2S-LZTS 2:1:0.25:2 and Na_2S-NZTS 2:1:0.5:4 ratio demonstrated wide band gaps of 3.14 eV and 3.28 eV respectively. The crystal structural analysis confirmed the dominant formation of kesterite for CZTS and CZTSe nanoparticles. On the other hand, the novel LZTS and NZTS nanoparticles exhibited a PMCA crystal phase, which was confirmed by the lattice constant calculations.

The change is crystal phase between the Cu-based nanoparticles and the alkali-metal-based nanoparticles is attributed to the increase in atomic radii from 128 pm for Cu, 152 pm for Li and 186 pm for Na. Further, structural analysis illustrated quasi-spherical (CZTS, LZTS), elongated (CZTSe), mostly spherical (NZTS) and all NPs were poly-dispersed and exhibited agglomerated morphological properties as observed in TEM images. Moreover, the surface analysis through XPS, FT-IR and liquid-state NMR confirmed the successful capping of the nanoparticles with OLA. In addition to the surface chemistry, XPS measurements confirmed the composition and oxidation states of the nanoparticles for each element (i.e. Cu^{+}, Li^{+}, Na^{+}, Zn^{2+}, Sn^{4+}, S^{2-}, Se^{2-}). The variations in Li and Na ratios were observed in both XPS and MAS NMR measurements. Both techniques indicated that the presence and abundance of the Li and Na monovalent cations was prevalent in the Li_2S-LZTS 2:1:0.25:2 and Na_2S-NZTS 2:1:0.5:4 ratios. The combination of structural analysis together with the Raman spectroscopy, further confirmed the formation of Cu_2ZnSnS_4, $Cu_2ZnSnSe_4$, Li_2ZnSnS_4 and Na_2ZnSnS_4 respectively. This study endorses that the use of the colloidal method, is effective in the synthesis of CZTS and CZTSe including the novel synthesis of LZTS and NZTS nanoparticles respectively.

The electrochemical properties were investigated by cyclic voltammetry and electrochemical impedance spectroscopy. The cyclic voltammograms illustrated the reduction of the triiodide ions, observed through the two-pairs of the redox peaks. The CZTS, CZTSe, LZTS and NZTS

counter electrodes, mimicked the same shape as the state-of-the-art platinum electrode, which was indicative of good electrocatalytic activity.

Different contact substrates (ITO, FTO and VC) were explored to investigate the effect of the electrocatalytic performance on the varied counter electrodes for application in DSSCs. The VC was reported for the first time as a contact substrate for the CZTS and CZTSe counter electrodes. Despite the low surface resistance, high conductivity and stability, the opaque nature of the substrate hindered the transmittance of light thus, resulting in the lowest PCE for both counter electrodes. However, the EIS measurements demonstrated that the use of ITO, as the contact substrate, gave the best electrochemical results for all the quaternary nanoparticles in comparison to FTO. The CZTS-ITO, LZTS-ITO and NZTS-ITO counter electrodes were observed to have higher PCE because of the low charge transfer (R_{ct}), low series resistance (R_s), large exchange current density (J_0) and high limiting diffusion current (J_{lim}). The fabricated DSSCs, demonstrated that PCE of LZTS-ITO was 2.26%, followed by CZTS-ITO was 3.62%, subsequently, NZTS-ITO was 3.93%. NZTS-ITO showed improved electrocatalytic activity when compared to CZTS and LZTS specifically and this could be due to the extreme distortion that NZTS can exhibit because of the large cation (i.e. 186 pm). The increased distortion could introduce more defects that improve its electrical performance.

6.2. Recommendations

The full replacement of Cu^+ with Li^+ and Na^+ alkali metals respectively, is rarely reported on apart from the proven doping/alloying effects. However, the doping/alloying effects have reached stagnancy and the successful colloidal synthesis of the alkali metal quaternary semiconducting nanoparticles, introduces a new cohort of nanoparticles that can be explored further. The synthetic results using alkali metals together with the electrocatalytic activity observed in this study show promising results as an alternative to the Pt counter electrode in DSSCs.

Future work:

- Conduct Rietveld refinement calculations for a better understanding of the crystal phases.

- To further explore the use of capping agents (i.e. hexadecylamine, 1,1,1-trichloro-2,2-bis[p-chlorophenyl]ethane, oleic acid and trioctylphosphine) or the combination of these capping agents in size and shape engineering.
- To explore the effects of ligand exchange (for shorter chains). It has been shown that shorter ligands shorten the inter-particle spacing hence creating channels for charge mobility
- Explore more Li (lithium sulfate) and Na (sodium sulfate, sodium selenite) precursors.
- Optimize the fabrication of the DSSC – vary the thin film fabrication.
    - A detailed study on why different substrates behave differently.
    - Explore different electrolytes and photoanode (i.e. dye & electron transport layer) components.
    - Vary the layers of the counter electrode material.

APPENDIX
Supporting Information

Chapter 3

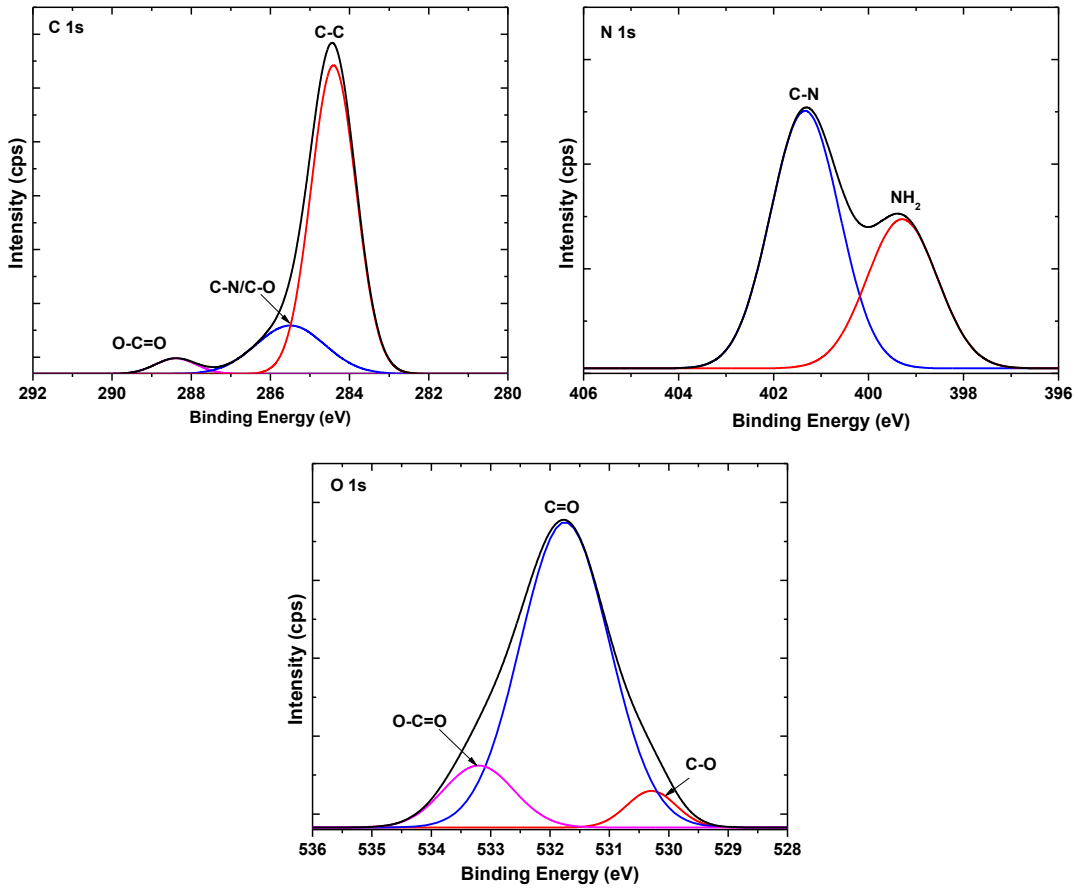

Fig. 3.1S: C 1s, N 1s and O 1s high-resolution spectra for CZTSe nanoparticles.

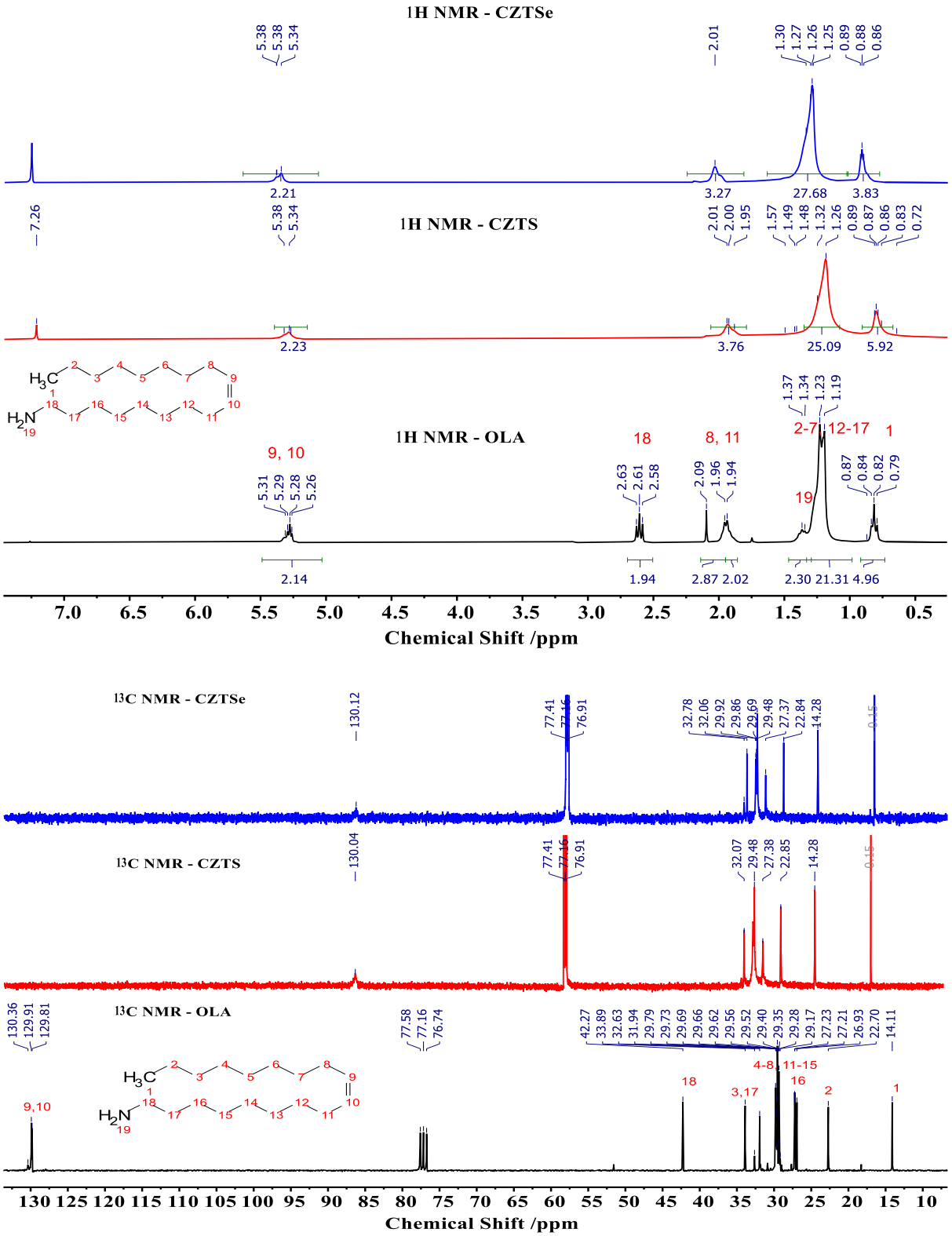

Fig. 3.3S: ^{1}H NMR and ^{13}C NMR spectra of oleylamine, CZTS and CZTSe nanoparticles.

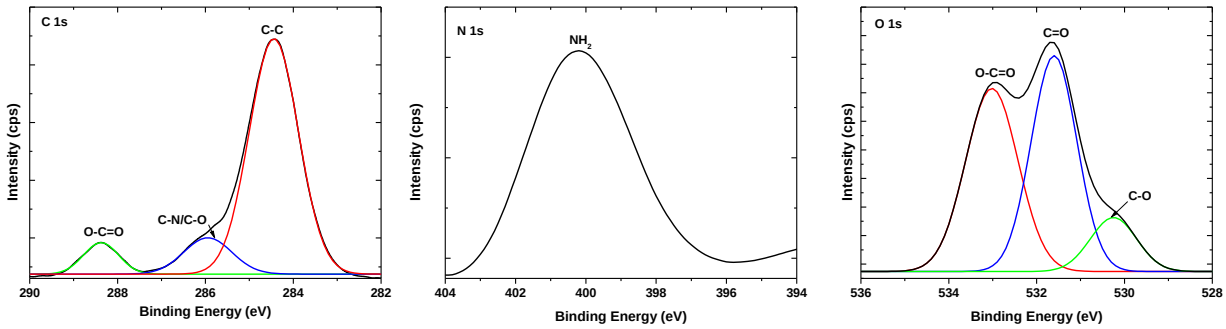

Fig. 4.1S: LiCl_LZTS (1:1:1:1) ratio nanocrystals depicting the high-resolution spectra of the C 1s, N 1s and O 1s.

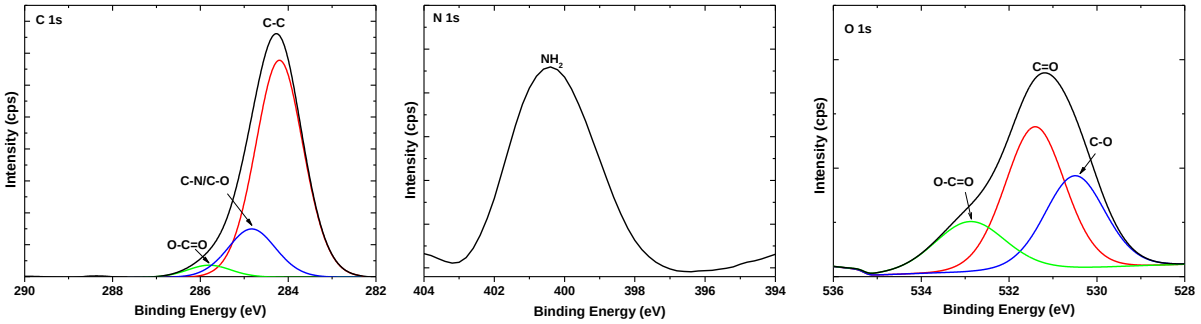

Fig. 4.2S: LiCl_LZTS (2:1:0.25:2) ratio nanocrystals depicting the high-resolution spectra of the C 1s, N 1s and O 1s.

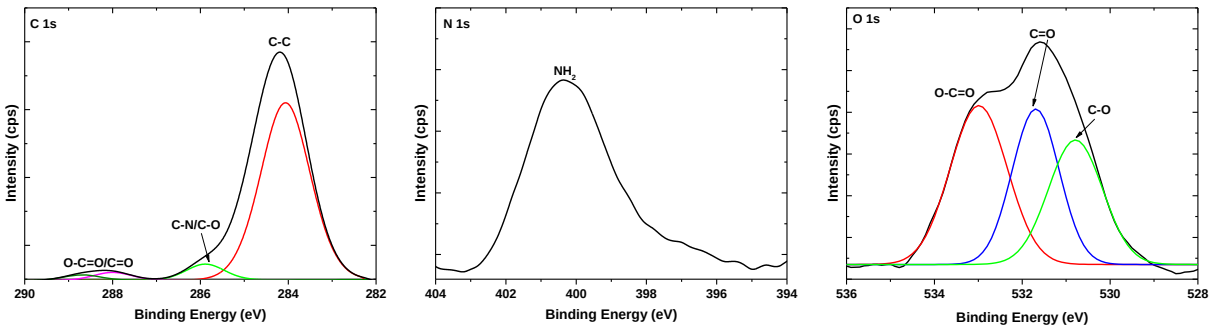

Fig. 4.3S: Li_2S_LZTS (1:1:1:1) ratio nanocrystals depicting the high-resolution spectra of the C 1s, N 1s and O 1s.

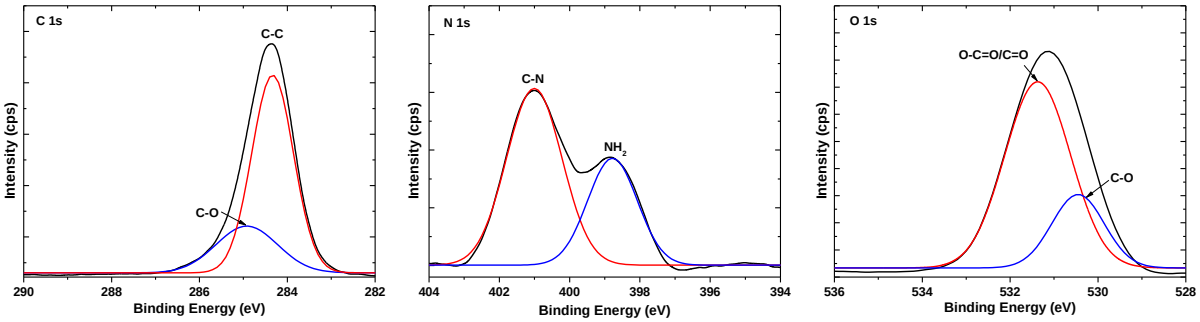

Fig. 4.4S: Li_2S_LZTS (2:1:0.25:2) ratio nanocrystals depicting the high-resolution spectra of the C 1s, N 1s and O 1s.

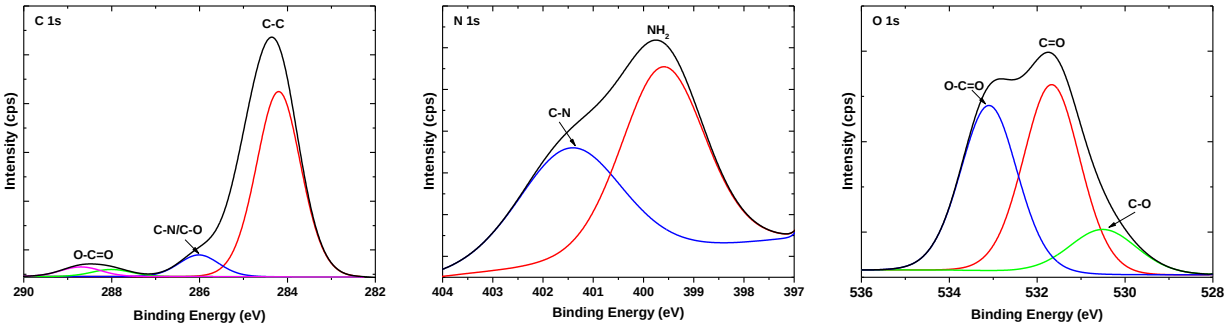

Fig. 4.5S: Li(acac)_LZTS (1:1:1:1) ratio nanocrystals depicting the high-resolution spectra of the C 1s, N 1s and O 1s.

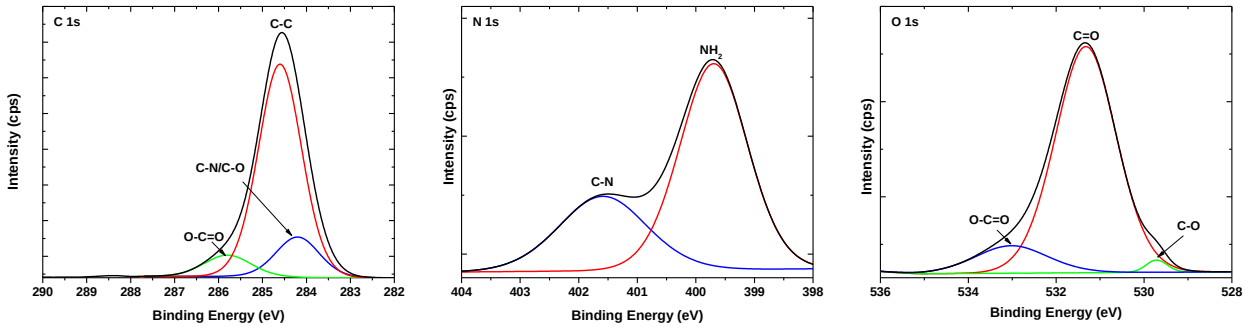

Fig. 4.6S: Li(acac)_LZTS (2:1:0.25:2) ratio nanocrystals depicting the high-resolution spectra of the C 1s, N 1s and O 1s.

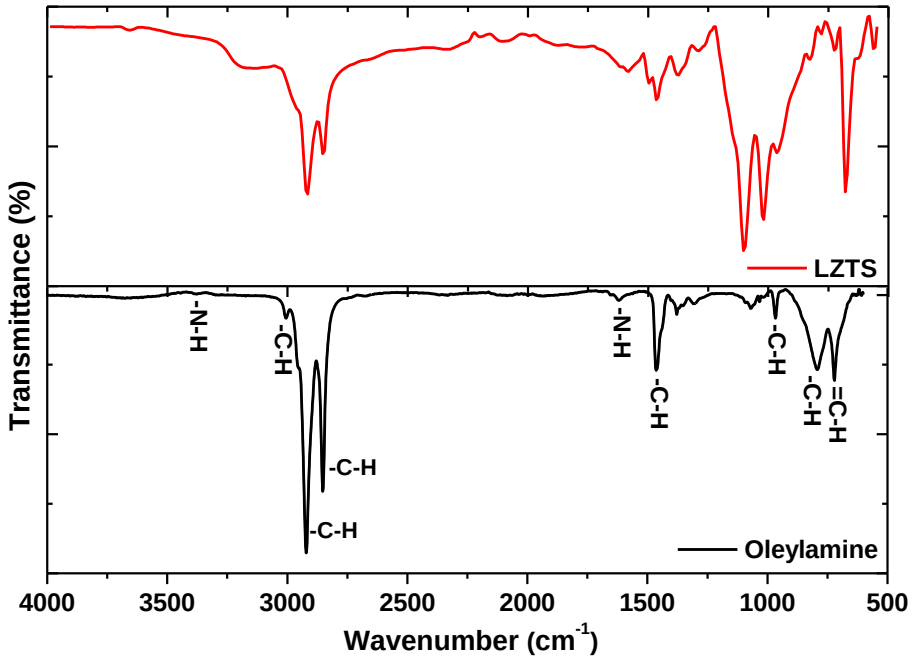

Fig. 4.7S: OLA and LZTS FT-IR spectra

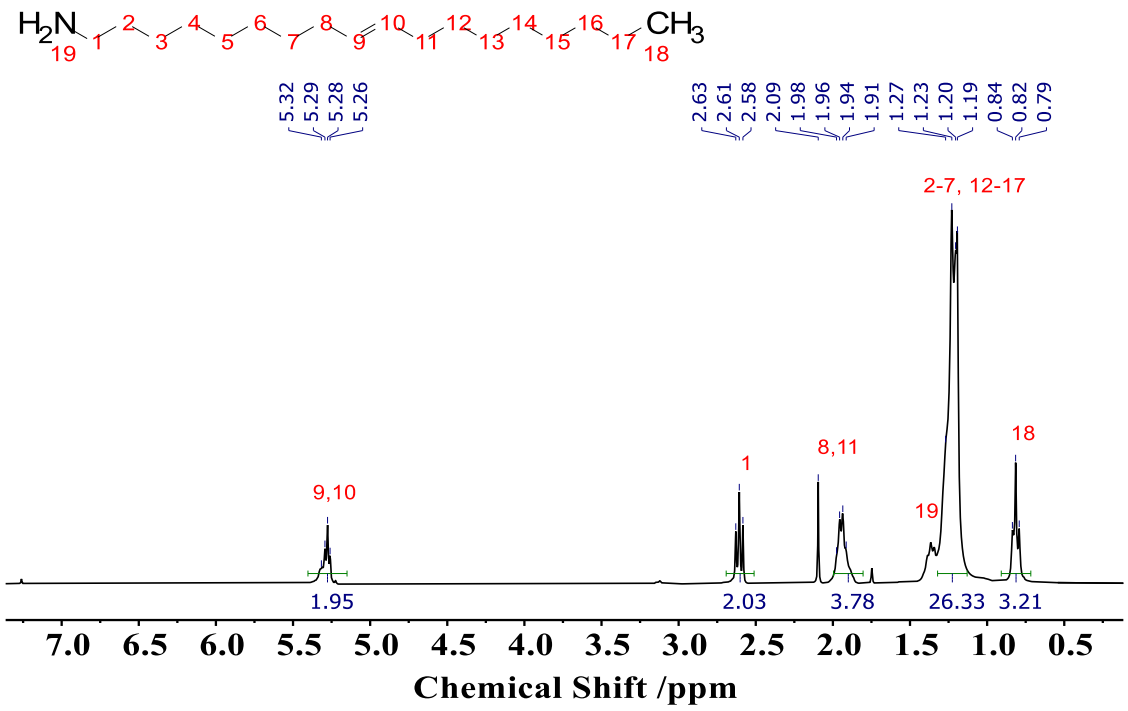

Fig. 4.8S: the ^{1}H NMR spectra of OLA.

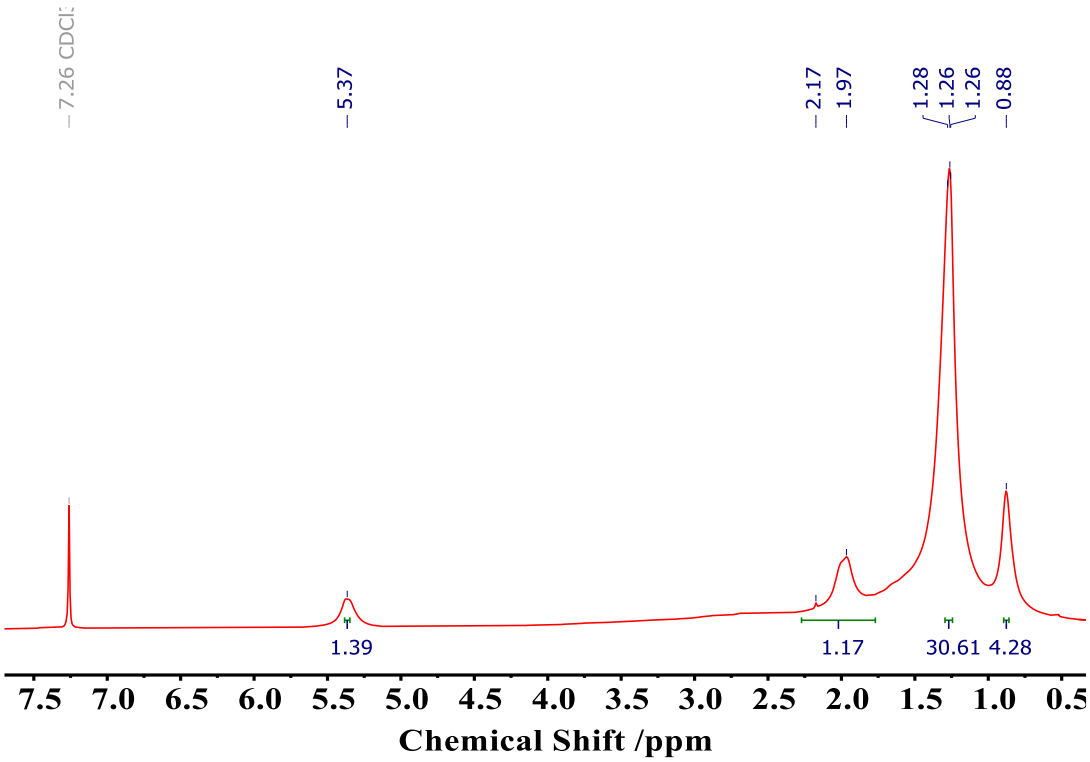

Fig. 4.9S: the ^{1}H NMR spectra of Li_2S_LZTS nanoparticles.

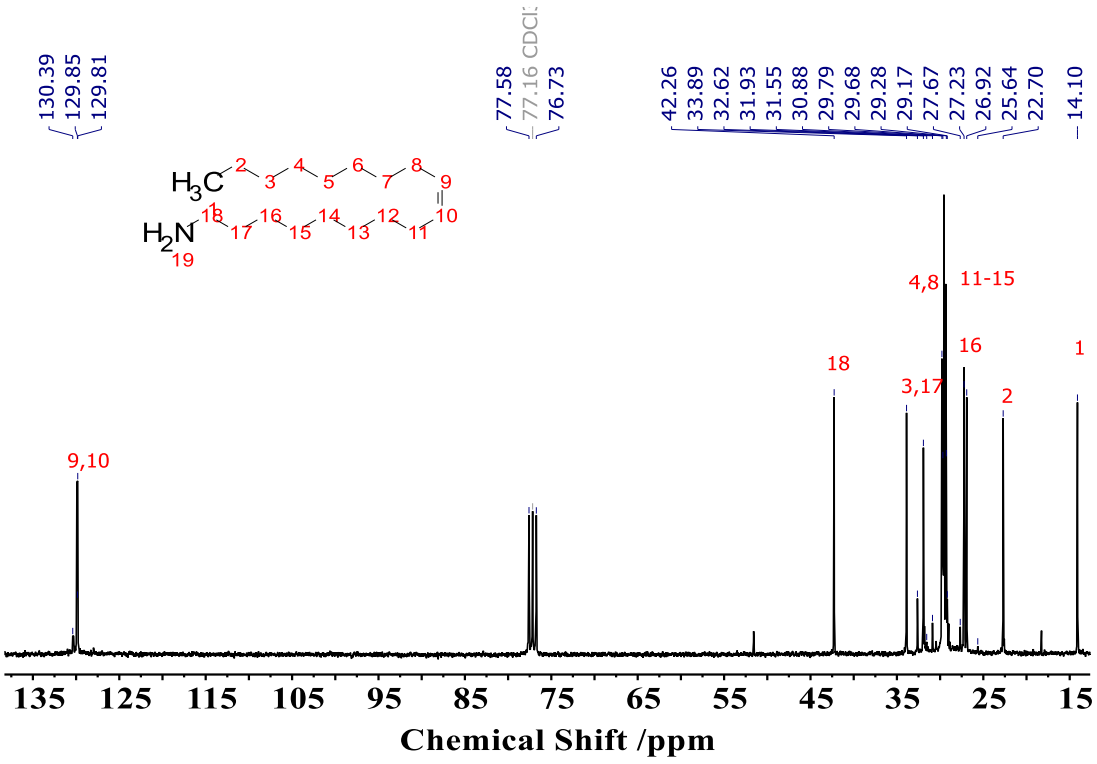

Fig. 4.10S: the ^{13}C NMR spectra of OLA.

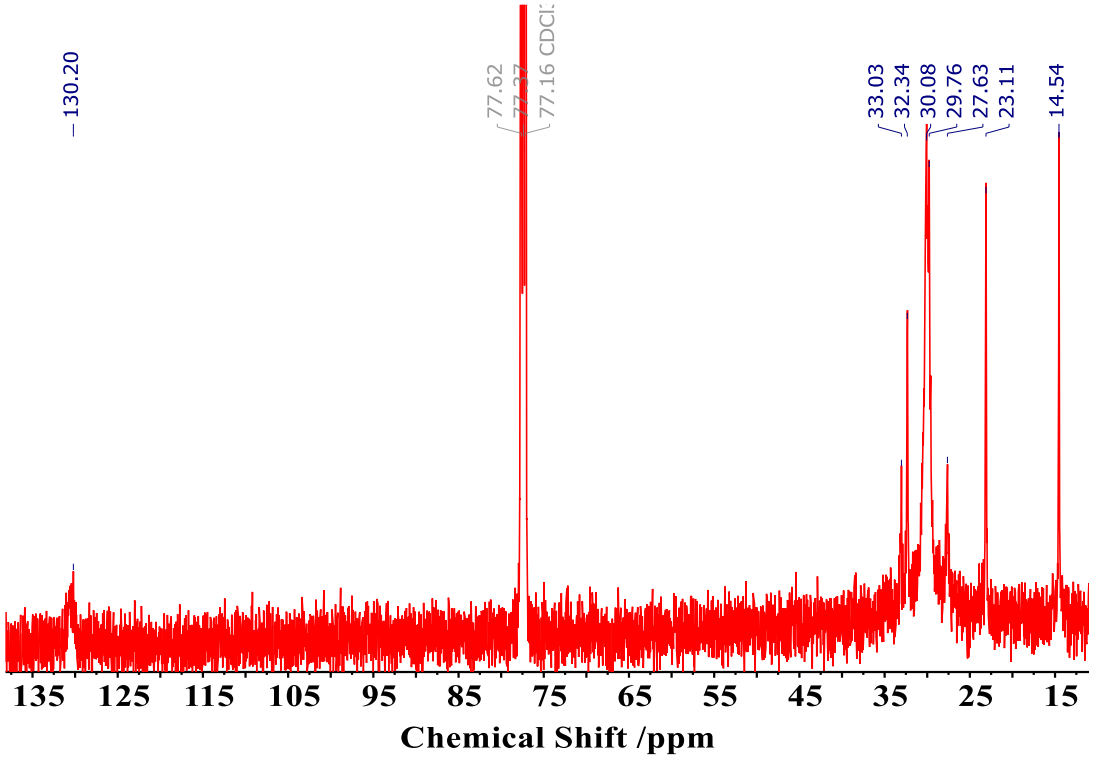

Fig. 4.11S: the ^{13}C NMR spectra of Li_2S_LZTS.

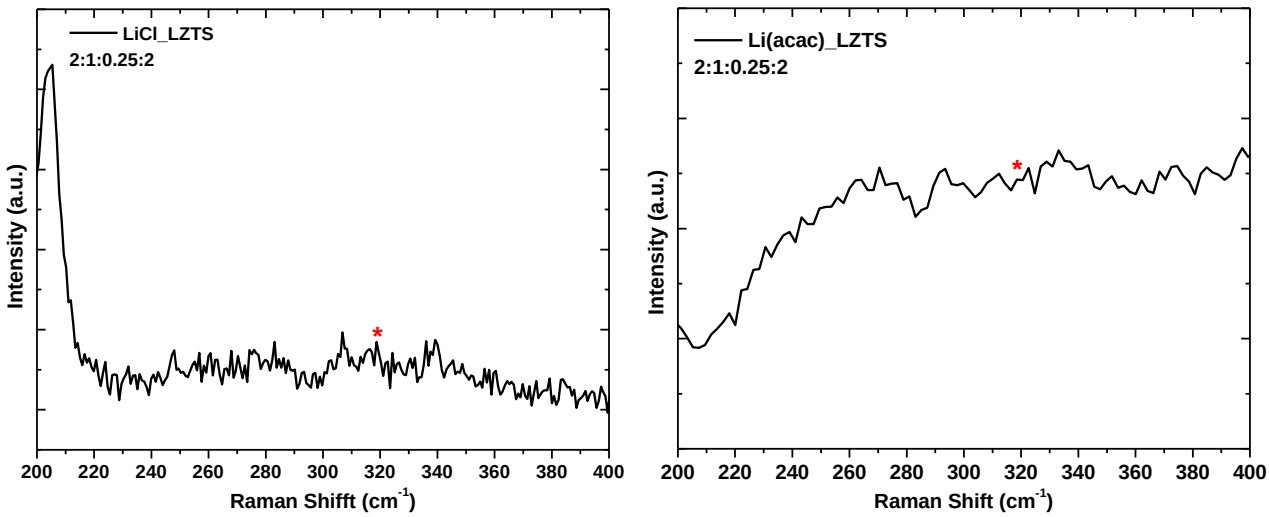

Fig. 4.12S: Raman spectra of LiCl and Li(acac) LZTS material analysed using the 785 nm laser.

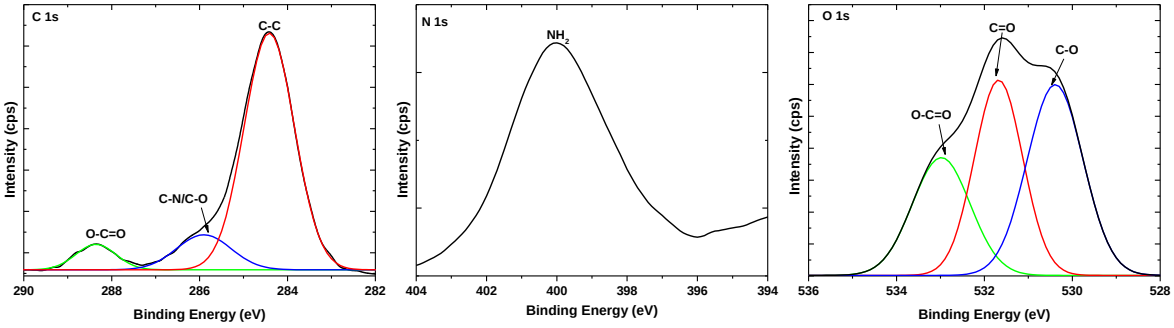

Fig. 5.1S: C 1S, N 1s and O 1s high-resolution spectra for NaCl_NZTS (1:1:1:1) ratio nanoparticles.

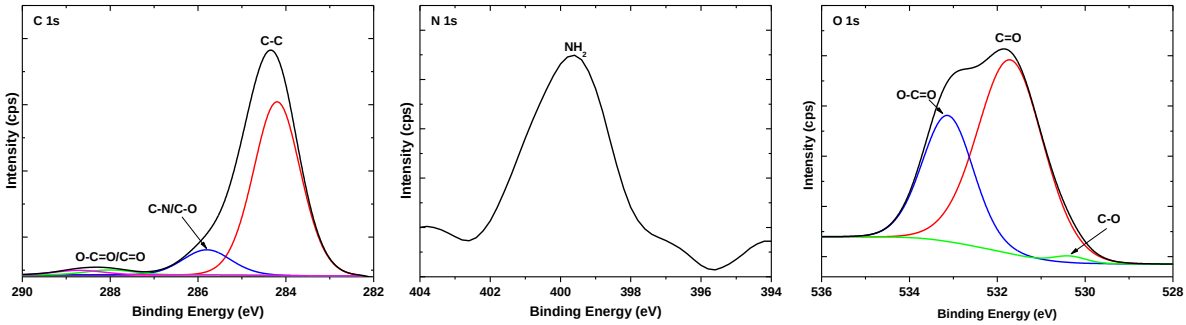

Fig. 5.2S: C 1S, N 1s and O 1s high-resolution spectra for NaCl_NZTS (2:1:0.5:4) ratio nanoparticles.

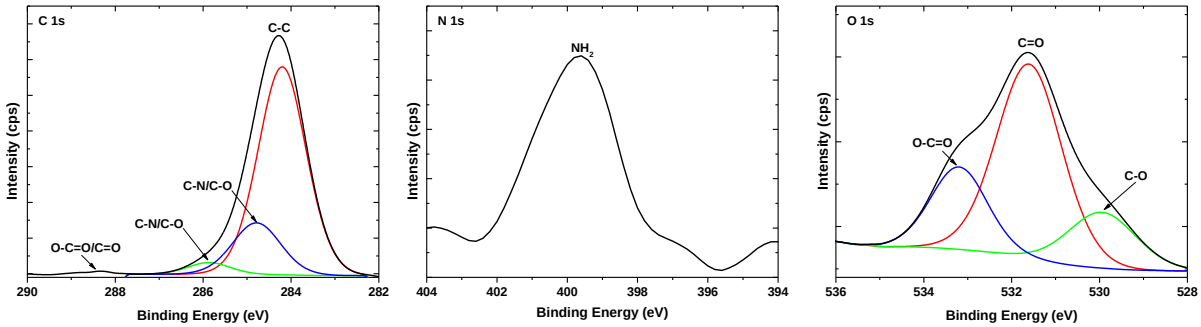

Fig. 5.3S: C 1S, N 1s and O 1s high-resolution spectra for Na_2S_NZTS (1:1:1:1) ratio nanoparticles.

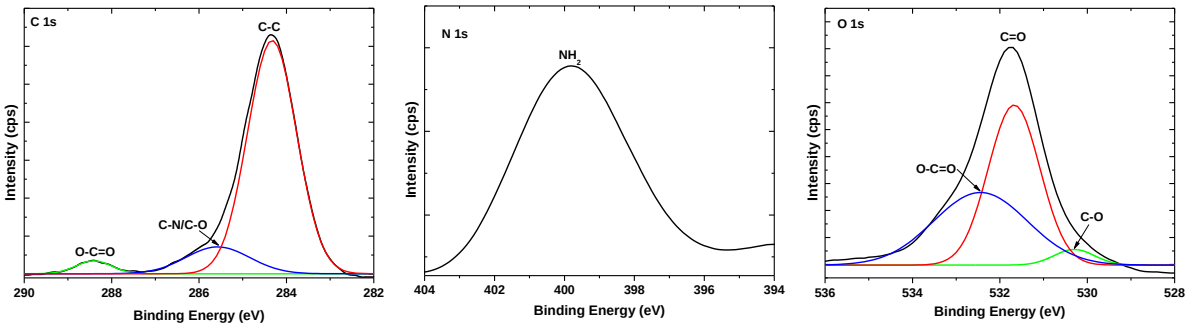

Fig. 5.4S: C 1S, N 1s and O 1s high-resolution spectra for Na_2S_NZTS (2:1:0.5:4) ratio nanoparticles.

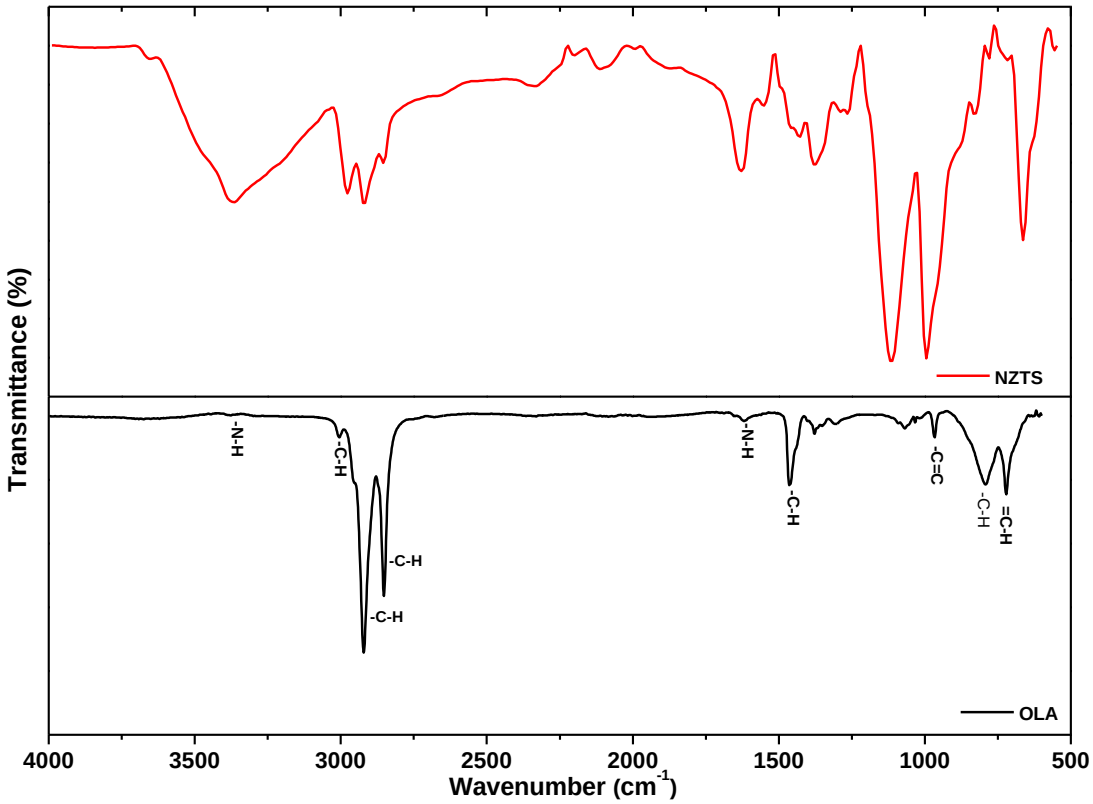

Fig. 5.5S: FT-IR spectra of OLA & NZTS respectively.

Table 5.1S: Summary of the atomic composition stoichiometric assignments obtained from the fitting of the XPS spectra.

	Element	Atomic (%)	Peak binding energy (eV)	Assignments	FWHM (eV)
NaCl_NZTS (1:1:1:1)	C	45.9	284.7	C – C	1.4
		6.0	286.3	C – O	
		4.7	288.6	O – C = O	
	N	0.7	400.6	N	0.3
	O	7.8	530.5	C = O	1.5
		9.0	531.9	C – O	
		4.5	533.3	O – C = O	
	Na	-	1072.2	1s	-
	Zn	0.4	1022.0	Zn 2p3	1.4
	Sn	0.5	484.7	Sn	0.9
		5.2	486.4		1.6
	S	6.5	161.3	2p3	1.2
		6.5	162.4	2p1	

Table 5.2S: Summary of the atomic composition stoichiometric assignments obtained from the fitting of the XPS spectra.

	Element	Atomic (%)	Peak binding energy (eV)	Assignments	FWHM (eV)
NaCl_NZTS (2:1:0.5:4)	C	55.9	284.2	C – C	1.3
		13.9	285.9	C – N / C – O	
		2.7	288.6	C – N / C – O	1.1
	N	2.2	399.4	N	2.2
	O	2.8	529.9	C = O	1.8
		0.8	531.6	C – O	1.5
		1.0	533.2	O – C = O	1.7
	Na	1.4	1073.1	1s	2.4
	Zn	2.1	1021.7	Zn 2p3	1.7
		1.2	1023.5		2.4
	Sn	4.0	486.4	Sn	1.3
	S	12.0	160.9	2p3	1.2

Table 5.3S: Summary of the atomic composition stoichiometric assignments obtained from the fitting of the XPS spectra.

	Element	Atomic (%)	Peak binding energy (eV)	Assignments	FWHM (eV)
Na_2S_NZTS (1:1:1:1)	C	46.2	284.2	C – C	1.2
		20.6	284.8	C – N / C – O	1.2
		6.9	285.8	C – N / C – O	1.3
		1.3	288.0	C = O	1.3
		1.3	288.7	O – C = O	1.3
	N	1.8	399.9	N	2.8
	O	1.8	530.4	C – O	0.8
		3.5	531.7	C = O	1.7
		2.5	533.1	O – C = O	1.3
	Na	0.9	1072.7	1s	2.4
	Zn	1.2	1021.7	Zn 2p3	1.7
		0.8	1023.4		2.4
	Sn	3.1	486.1	Sn	1.4
	S	8.1	161.0	2p3	1.3

Table 5.4S: Summary of the atomic composition stoichiometric assignments obtained from the fitting of the XPS spectra.

	Element	Atomic (%)	Peak binding energy (eV)	Assignments	FWHM (eV)
Na_2S_NZTS (2:1:0.5:4)	C	52.7	284.8	C – C	1.3
		4.8	286.3	C – N / C – O	1.3
		2.8	288.8	O – C = O	1.3
	N	1.7	400.4	N	3.4
	O	10.7	532.9	C = O	1.4
		1.3	530.6	C – O	0.5
		4.3	533.5	O – C = O	2.9
	Na	1.5	1071.7	1s	1.4
	Zn	2.7	1021.8	2p3	1.2
	Sn	2.1	486.4	Sn	1.1
	S	6.6	161.3	2p3	1.2
		6.6	162.4	2p1	1.2
		0.8	162.8	2p3	1.1
		0.7	168.2	2p3	1.2
		0.7	169.4	2p1	1.2

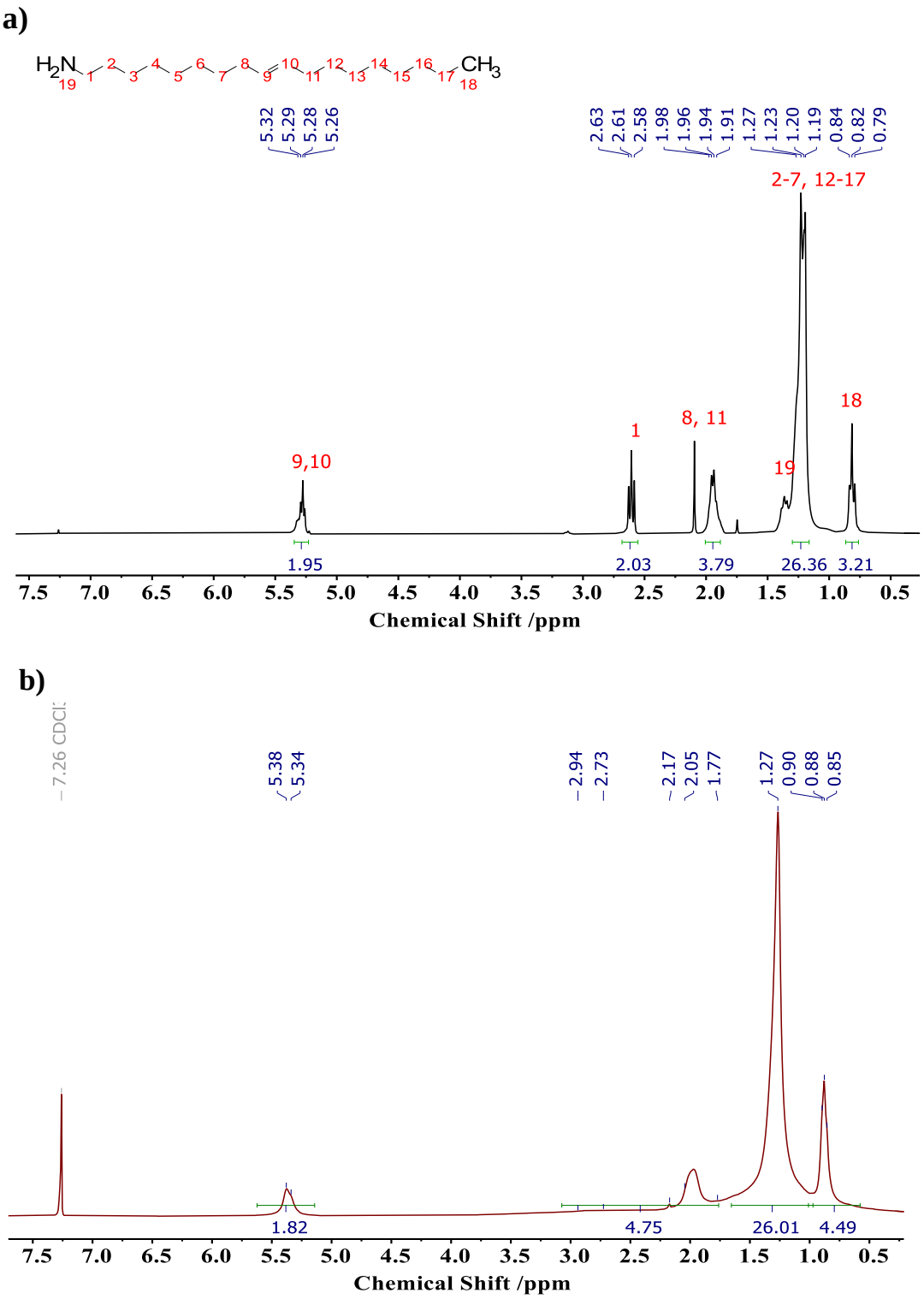

Fig. 5.6S: ^{1}H NMR spectra of (a) OLA and (b) NZTS nanoparticles.

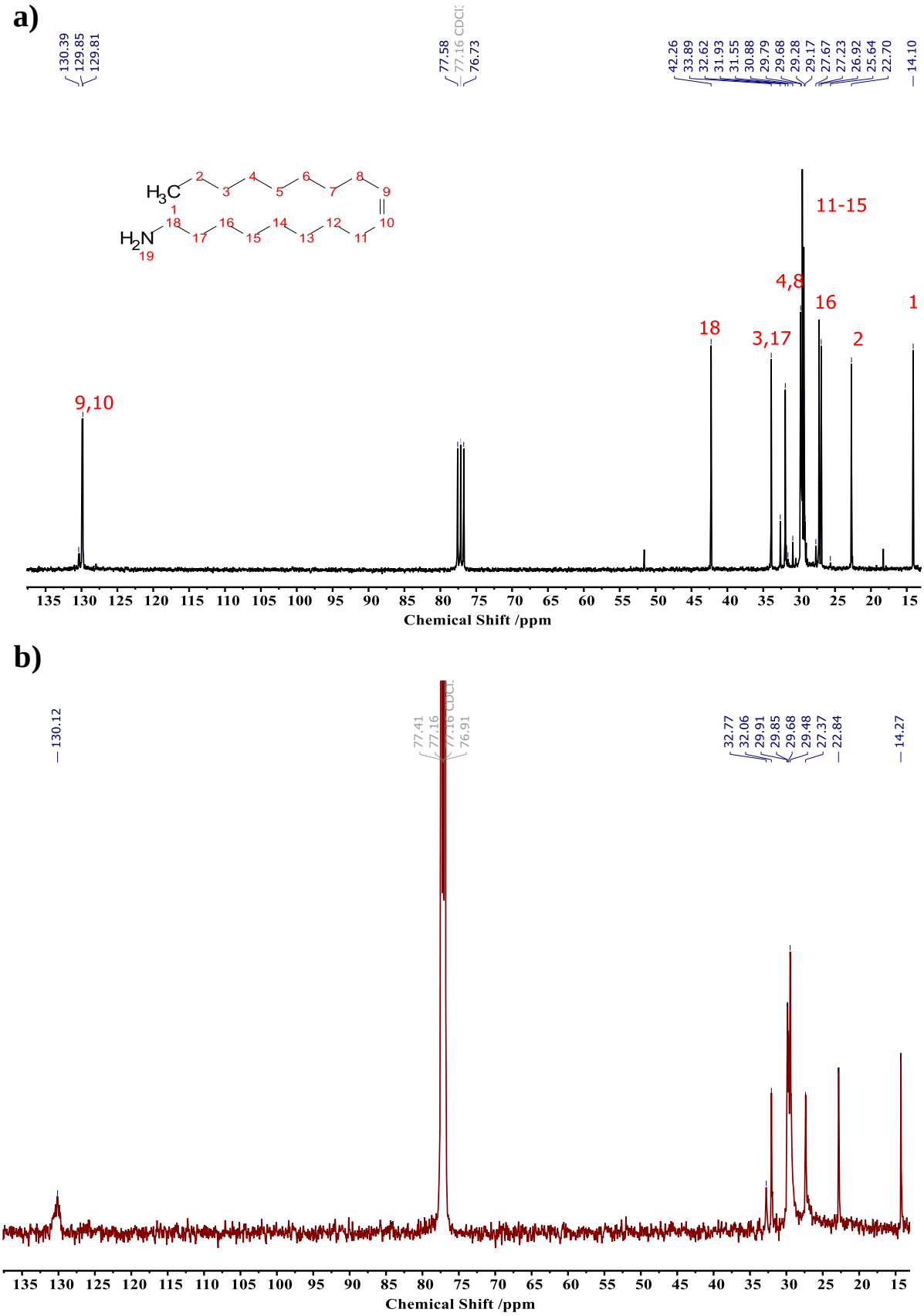

Fig. 5.7S: ^{13}C NMR spectra of (a) OLA and (b) NZTS nanoparticles.

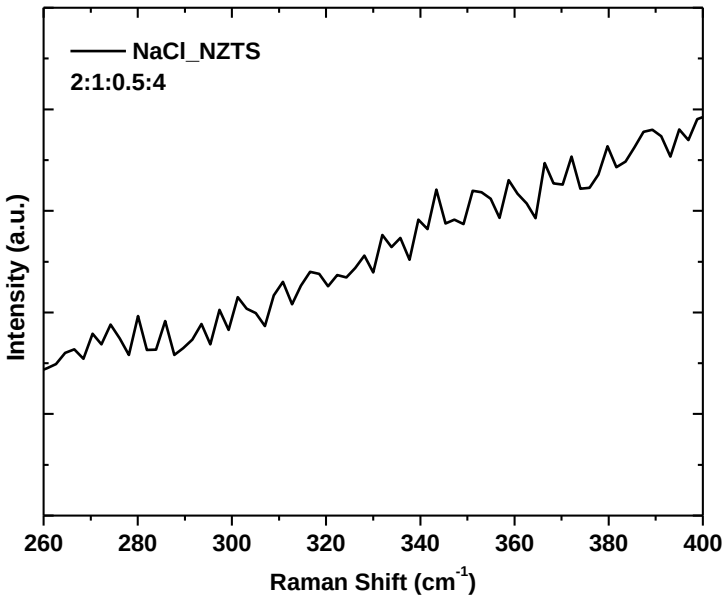

Fig. 5.8S: Raman spectrum of NaCl_NZTS.